NASA/TM—1999-206966

Structures and Acoustics Division 1996 Annual Report

Cynthia S. Acquaviva
Glenn Research Center, Cleveland, Ohio

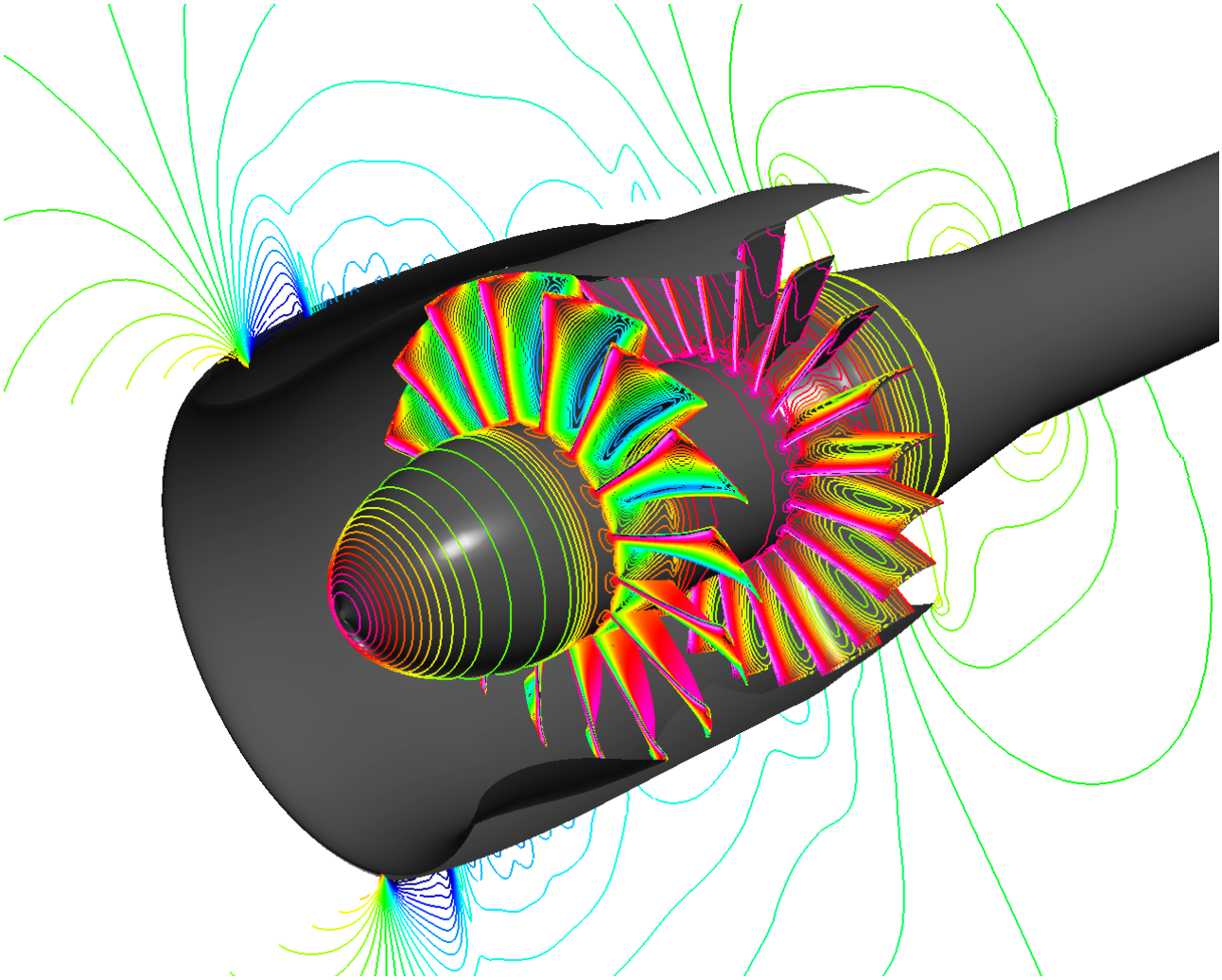

November 1999

The NASA STI Program Office . . . in Profile

Since its founding, NASA has been dedicated to the advancement of aeronautics and space science. The NASA Scientific and Technical Information (STI) Program Office plays a key part in helping NASA maintain this important role.

The NASA STI Program Office is operated by Langley Research Center, the Lead Center for NASA's scientific and technical information. The NASA STI Program Office provides access to the NASA STI Database, the largest collection of aeronautical and space science STI in the world. The Program Office is also NASA's institutional mechanism for disseminating the results of its research and development activities. These results are published by NASA in the NASA STI Report Series, which includes the following report types:

- TECHNICAL PUBLICATION. Reports of completed research or a major significant phase of research that present the results of NASA programs and include extensive data or theoretical analysis. Includes compilations of significant scientific and technical data and information deemed to be of continuing reference value. NASA's counterpart of peer-reviewed formal professional papers but has less stringent limitations on manuscript length and extent of graphic presentations.

- TECHNICAL MEMORANDUM. Scientific and technical findings that are preliminary or of specialized interest, e.g., quick release reports, working papers, and bibliographies that contain minimal annotation. Does not contain extensive analysis.

- CONTRACTOR REPORT. Scientific and technical findings by NASA-sponsored contractors and grantees.

- CONFERENCE PUBLICATION. Collected papers from scientific and technical conferences, symposia, seminars, or other meetings sponsored or cosponsored by NASA.

- SPECIAL PUBLICATION. Scientific, technical, or historical information from NASA programs, projects, and missions, often concerned with subjects having substantial public interest.

- TECHNICAL TRANSLATION. English-language translations of foreign scientific and technical material pertinent to NASA's mission.

Specialized services that complement the STI Program Office's diverse offerings include creating custom thesauri, building customized data bases, organizing and publishing research results . . . even providing videos.

For more information about the NASA STI Program Office, see the following:

- Access the NASA STI Program Home Page at ***http://www.sti.nasa.gov***

- E-mail your question via the Internet to help@sti.nasa.gov

- Fax your question to the NASA Access Help Desk at (301) 621-0134

- Telephone the NASA Access Help Desk at (301) 621-0390

- Write to:
  NASA Access Help Desk
  NASA Center for AeroSpace Information
  7121 Standard Drive
  Hanover, MD 21076

NASA/TM—1999-206966

Structures and Acoustics Division 1996 Annual Report

Cynthia S. Acquaviva
Glenn Research Center, Cleveland, Ohio

National Aeronautics and
Space Administration

Glenn Research Center

November 1999

Available from

NASA Center for Aerospace Information
7121 Standard Drive
Hanover, MD 21076
Price Code: A04

National Technical Information Service
5285 Port Royal Road
Springfield, VA 22100
Price Code: A04

Introduction

The 1996 Annual Report of the Structures Division reflects the work areas performed by the Division staff during the 1996 calendar year. Its purpose is to give a brief, but comprehensive review of the Division's technical accomplishments. As with the reports for the previous years, the report is organized topically. The descriptions of the research reflect work that has been reported in the open literature during the year.

The Structures and Acoustics Division comprises a staff of approximately 82 engineers and scientists plus administrative and support personnel. The work areas comprise composite mechanics, fatigue, fracture, and dynamics with emphasis on life and reliability, as well as mechanical system technologies and aeroacoustics. The Division works cooperatively with both industry and universities to develop the technology necessary for state-of-the-art advancement in aeronautical and space propulsion systems. In the future, propulsion systems will need to be lighter, to operate at higher temperatures and to be more reliable in order to achieve higher performance. Achieving these goals is complex and challenging. If you need additional information, please do not hesitate to contact me or the appropriate Division staff contact provided in this publication.

L. James Kiraly

Chief, Structures and Acoustics Division

Contents

Structural Mechanics

Design Sensitivity Approximations Improve Performance of Optimization Algorithms 1
Performance of Optimization Methods Improved Through Selected Algorithms 1
Finite-Element Formulation for Smart Structures in Thermal Environments 2
Micromechanics for Particle-Reinforced Composites 3
Micromechanics for Two-Dimensional Woven Composites 4

Fatigue and Fracture

Experimental Techniques Verified for Determination of Yield and Flow Surfaces 6
Creep-Fatigue Behavior of Cast IN 939 Superalloy 7
Fatigue Crack Growth of Single-Crystal Superalloys in Hydrogen 8
Reliability Modeling of Brittle, Anisotropic Solids 9
Fatigue Behavior and Life Prediction of a T650-35/PMR-15 (0/90) Weave Under Isothermal Conditions 10
A General Representation Capturing Reversible and Irrevesible Hereditary Behavior of a Titanium Alloy 12
Damage Mechanisms and Mechanical Property Degradation in Titanium Matrix Composites Subjected to TMF Loadings 14

Structural Integrity

CARES/*Life* Ceramics Durability Evaluation Software for Finite-Element Analysis Programs 16
Creep Life Prediction of Ceramic Components Subjected to Transient Tensile and Compressive Stress States 18
Constitutive Theory Developed for Monolithic Ceramic Materials 19
Single Transducer Ultrasonic Imaging Method That Eliminates the Effect of Thickness in Imaging of High-Temperature Structural Materials 20
Noncontact Measurement of Acousto-Ultrasonics for Ceramic Matrix Composites 21

Structural Dynamics

Dynamic Spin Rig Magnetic Suspension 23
High-Temperature Magnetic Bearings for Gas Turbine Engines 25
Neural Network Control of a Magnetically Suspended Rotor System 26
Damping Experiment of Spinning Component Plates With Embedded Viscoelastic Material 28
Improved Dual Clearance Squeeze Film Damper for High Loads 29
User's Guide for MSAP2D, an Euler Flutter and Forced-Response Analysis Code for Multistage Turbomachinery 30
User's Manual for ASTROP2, Version 2.0, a Program for Aeroelastic Stability Analysis of Multiblade Structures 31
Using an Euler Aeroelastic Solver to Analyze Gust and Structural Response of a Two-Dimensional Cascade 31

Flutter Analysis of Ducted Rotors 33
TURBO-AE: An Aeroelastic Code for Propulsion Applications 35
Using an Integrated Fiber-Optic Light Probe to Measure Static Deflections in Rotating Turbomachinery 36
Feasibility of Using Neural Network Models for Accelerated Testing of Mechanical Systems 36

Acoustics

Scale-Model Acoustic Liner and Low-Tip-Speed Turbofan Testing 38
Acoustic Barrier Facilitates Inlet Noise Measurements for Aft-Dominated Fans 39
Jet Noise Prediction for Internal Exhaust Mixer Nozzles 41

Mechanical Components

Gear Crack Propagation Studies 43
Validated Method to Optimize Load Sharing of Split-Torque Transmissions 44
Evaluation of Face Gears for Aerospace Drive System Applications 45
Using Hob Offset to Balance Strength of Spur Gears 46
Brush Seals Tested for Joint Technology Advanced Gas Generator II Engine 48
Diagnostic Parameters Detect Gear-Tooth Fatigue Crack 49
Gas Journal Bearing Stability Versus Amplitude Ratio 51
NASA Selects 1996 Government Invention of the Year 52

Bibliography 54

Structural Mechanics

Design Sensitivity Approximations Improve Performance of Optimization Algorithms

Computational efficiency in design optimization has been enhanced through sensitivity approximations. The sensitivities of behavior constraints have been obtained with a small number of numerical calculations. Four algorithms were used to quantify the performance of the approximations: the sequence of unconstrained minimization technique (SUMT); the method of feasible directions (mFD); the sequence of quadratic programming (SQP); and the sequence of linear programming (SLP). All four optimization algorithms, through approximations, converged to correct optimum solutions. The use of approximations reduced by one-third the CPU time that would otherwise be required to solve the problem with explicit closed-form sensitivities.

The convergence characteristics for a 25-variable, 180-behavior constraints problem determined with explicit and approximate gradients by SUMT and SQP optimizers are shown in figures 1 and 2, respectively. Both algorithms converged to an optimum weight of 308.7 lb. The rates of convergence with and without approximations were in agreement. The problem, however, required somewhat fewer reanalysis cycles when approximate sensitivities were used.

Glenn contacts: Dale Hopkins, (216) 433–3260; and Surya Patnaik, (216) 433–5916

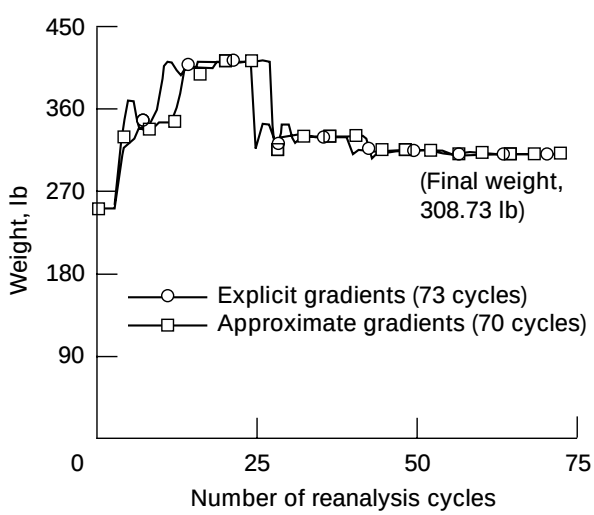

Figure 1.—Convergence of weight for ring as determined by using SUMT.

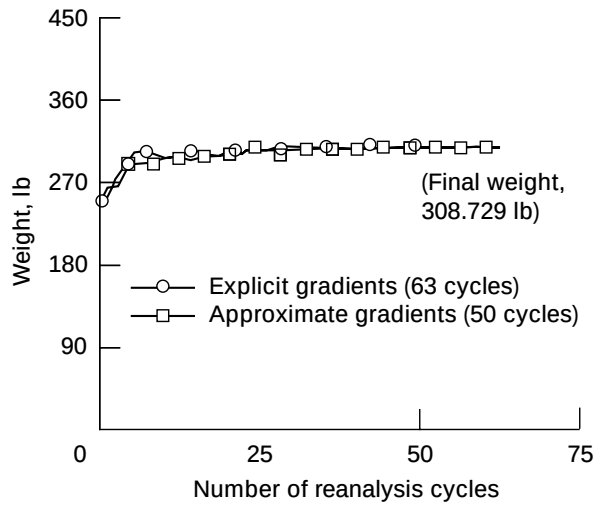

Figure 2.—Convergence of weight for ring as determined by using IMSL-SQP.

Performance of Optimization Methods Improved Through Selected Algorithms

Nonlinear programming algorithms play an important role in structural design optimization. The performance of optimization methods depends on the choice of algorithms. Reliable and efficient algorithms can be found by comparing the performance of different algorithms for the same set of design problems. A comparative study—for a set of about 50 structural design problems solved by using a dozen different algorithms—could not identify a single winner that can be called the most reliable and efficient. Overall, three algorithms scored high marks for large design problems: two sequential programming algorithms (SQP1 and SQP2) and a sequential unconstrained minimization technique (SUMT). The CPU times required to solve large problems were comparable for the three algorithms. Most algorithms, however, could solve at least one-third of the 50 examples.

Figure 1 shows the performance of 6 optimization algorithms in solving a set of 10 large problems. Three algorithms compare well, although with some variation.

Glenn contacts: Dale Hopkins, (216) 433–3260; and Surya Patnaik, (216) 433–5916

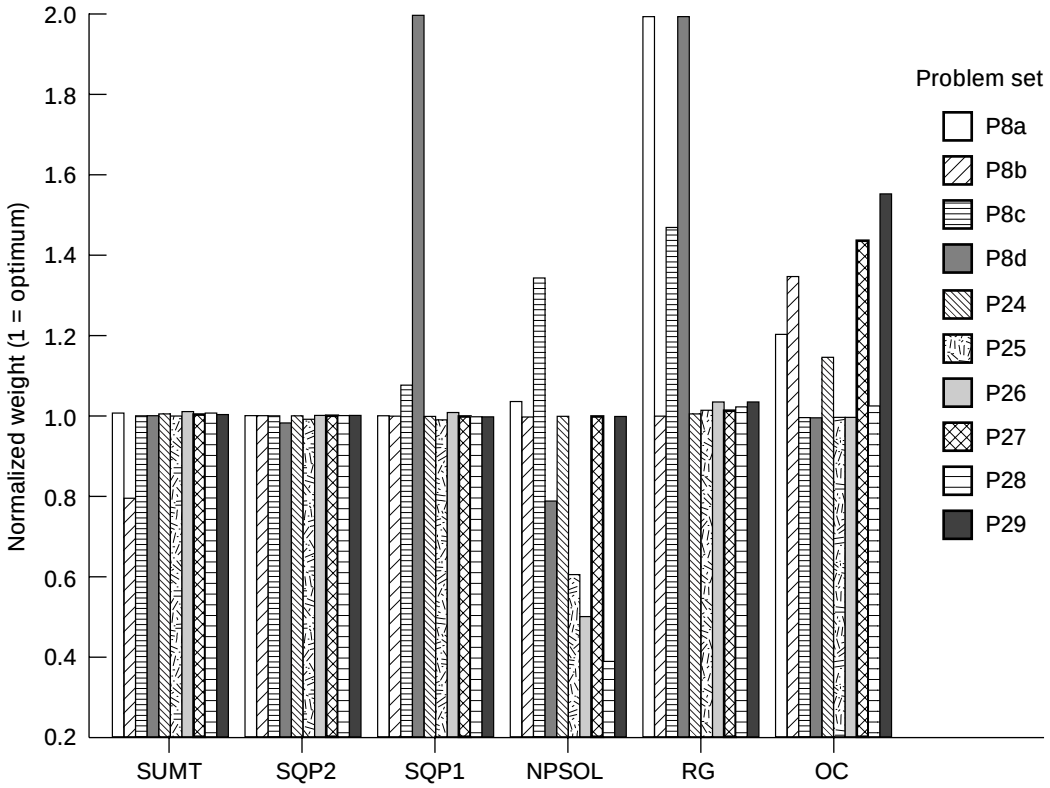

Figure 1.—Performance of different optimizers in solving large problems.

Finite-Element Formulation for Smart Structures in Thermal Environments

Aeropropulsion systems with piezoelectric composite components could offer great potential for improving the performance of aircraft engines through various vibration suppression, noise control, and thermal stability applications. To facilitate the characterization of such smart structures, we have extended finite-element methods to take into account the thermal effects so that the coupled mechanical, electrical, and thermal behavior of these materials can be analyzed.

Thermal effects typically affect the response of smart piezoelectric laminates by three distinct physical mechanisms: (1) thermal strains induced by a coefficient-of-thermal-expansion mismatch between the various composite and piezoelectric layers, (2) pyroelectric effects on the electric displacement of the piezoelectric material, and (3) temperature-dependent changes in both the composite and piezoelectric material properties.

We have incorporated the first two thermal effects mechanisms into a layerwise laminate theory to more accurately model both the active and sensory responses of smart structures. Corresponding finite-element formulations were derived and implemented for both beam and plate elements (Lee and Saravanos, 1996a, b, and c).

The capabilities of the finite-element formulation were demonstrated on a simply supported [0/±45]s graphite/epoxy plate with piezoceramic patches uniformly attached to both the top and bottom surfaces. Figure 1 illustrates the geometry and finite-element mesh of the plate. A linear thermal gradient (50 °C on the top surface and –50 °C on the bottom surface) was applied through the thickness of the plate. With no voltage applied, the bending deflection to both surfaces of the piezoceramic patches was as shown in figure 2(a). By increasing the active voltages applied to the piezoceramic patches, we gradually eliminated the thermally induced deflection of the plate. Figure 2(b) shows the reduction in the deflection achieved by applying an active voltage of 70 V.

Glenn contacts: Ho-Jun Lee, (216) 433–3316; Dimitris Saravanos, (216) 962–3211; and Dale Hopkins, (216) 433–3260

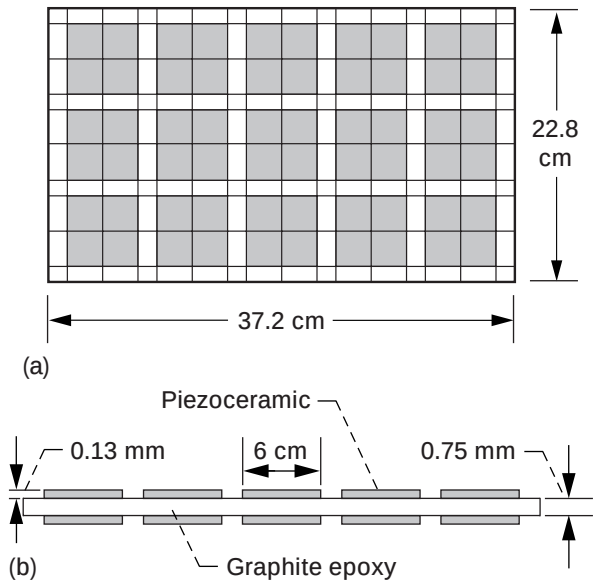

Figure 1.—Model of graphite/epoxy plate with attached piezoceramic patches. (a) Top view. (b) Front view.

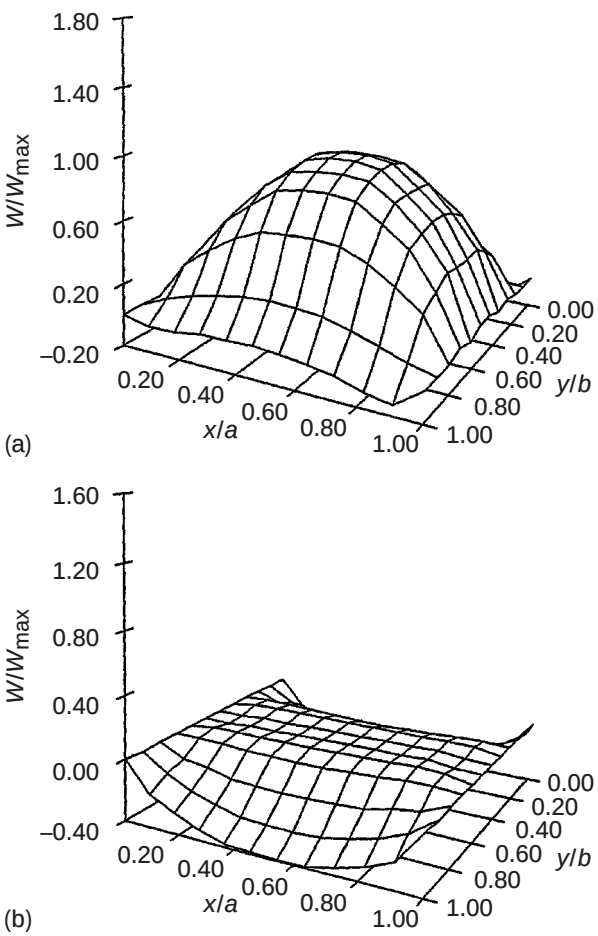

Figure 2.—Thermal shape control of a $[0/\pm45]_s$ plate subjected to a 100 °C gradient. (Deflection of plate, W; current position along the width axis, y; width of plate, b; current position along length axis, x; length of plate, a.) (a) No voltage applied. (b) 70 V applied on upper and lower piezoceramic patches.

Micromechanics for Particle-Reinforced Composites

Recently, there has been a growing interest in the use of particle-reinforced composites in many widely varying applications. Concrete can be thought of as one of the oldest material in this category. Because of the high costs and technical difficulties associated with the fabrication of continuous-fiber-reinforced composites, their use in certain applications is somewhat limited. For aerospace applications, particle-reinforced composites can be thought of as a viable alternative, especially where shock and impact properties are important. In fact, particle-reinforced composites (typically an aluminum matrix reinforced with SiC or TiC particles) have already shown great potential for many automotive applications, such as disk-brake rotors, connecting rods, cylinder liners, and other high-temperature applications. In situ reinforced ceramics, which have higher fracture toughness than monoliths and are easier to process in near-net shapes, can also be modeled as particle-reinforced composites.

For over two decades, NASA Glenn Research Center has been developing computer codes based on simplified micromechanics equations to simulate the behavior of continuous-fiber-reinforced composites, primarily for aerospace use. As a part of this research, several computer codes to simulate the behavior of polymeric, metallic/intermetallic, or ceramic matrix composites have been developed. By following a similar approach, we have developed a set of micromechanics equations for the analysis of particulate-reinforced composites. These equations were programmed as a separate module in an inhouse-developed code. They can predict the overall composite properties (mechanical and thermal) on the basis of volume fraction and the constituent's thermal and mechanical properties. The microstress equations were also developed to decompose the applied stress on the overall composite in terms of the constituent stresses. A limited verification study compared the predicted results with finite- and boundary-element methods and with some bounding techniques found in the literature for the analysis of particle-reinforced composites. The agreement was excellent, and the overall results demonstrate that the micromechanics equations for particle-reinforced composites can indeed model their behavior. Figure 1 compares the experimentally measured normal modulus for a particle-reinforced metal

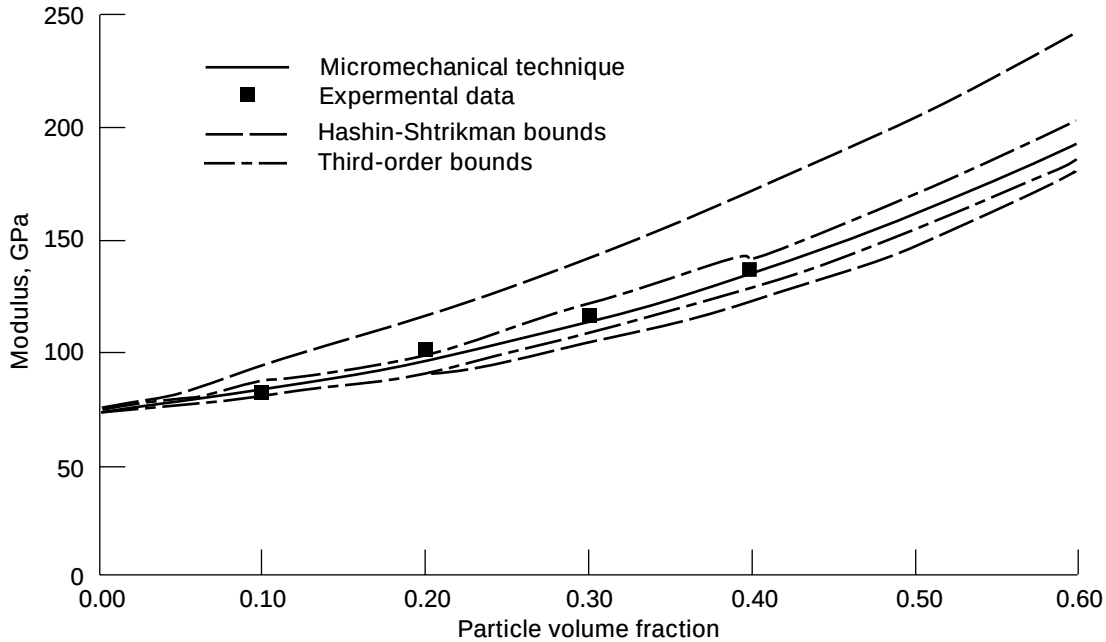

Figure 1.—Modulus of Al/SiC$_p$ composite. (The subscript p refers to the reinforcing particle.)

matrix composite with predictions made by various methods.

Glenn contacts: Subodh Mital, (216) 433–3261; Robert Goldberg, (216) 433–3330; and Pappu Murthy, (216) 433–3332

Micromechanics for Two-Dimensional Woven Composites

Woven fabric composites are constructed by weaving two or more fiber tows into each other to form a layer. These layers are then impregnated with a coating and some kind of resin or matrix material, stacked in a desired orientation, and cured to obtain a composite laminate of specified thickness. The interlacing of fiber bundles has several advantages, such as increasing the intralaminar and interlaminar strength, thereby providing greater damage tolerance and making possible the production of near-net-shape structural components. However, these advantages come at the expense of some loss in the inplane stiffness and strength, which depend on the weave architecture. There is certainly a need for sound engineering data as well as verified and efficient analytical and design methodologies to evaluate different design parameters. To accurately model such composites, one must use design methodologies that account for processing parameters and microstructural and geometrical features

We have developed a micromechanics-based technique that can be used to analyze any kind of two-dimensional weave architecture. It works in conjunction with the inhouse-developed codes ICAN (Integrated Composite Analyzer) and CEMCAN (Ceramic Matrix Composites Analyzer). The intent of this work was to develop a technique that can use the capabilities of already existing codes for laminated composite behavior, yet account for fiber waviness, fiber end distributions through the thickness, and constituent morphology that accurately represents the micromechanical behavior of woven composites. Micromechanics techniques have certain inherent advantages in terms of computational efficiency over other techniques that rely on numerical analyses.

Two material systems, a generic graphite/epoxy plain-weave composite and a SiC/SiC plain-weave ceramic matrix composite were analyzed with this technique. Results were compared with some available experimental data from three-dimensional finite-element analyses. There was a fair agreement between the two. This same technique is currently being used to develop a computer code for the

analysis of plain-weave composites. Figures 1 and 2 show the structure of a plain-weave fabric and inplane modulus of a SiC/SiC composite as a function of porosity.

Glenn contacts: Subodh Mital, (216) 433–3261; and Pappu Murthy, (216) 433–3332

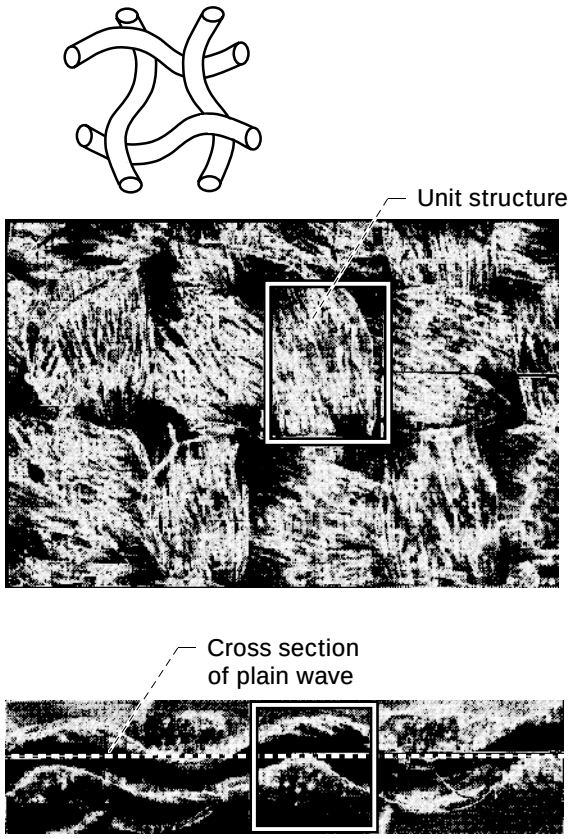

Figure 1.— Structure of a plain-weave fabric.

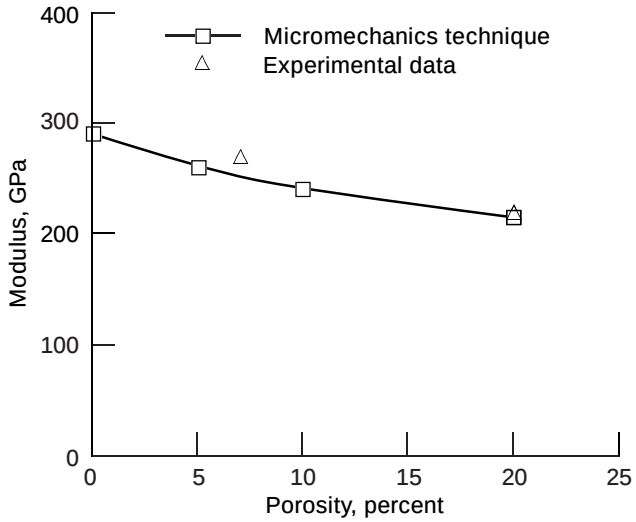

Figure 2.—In-plane modulus as a function of porosity for SiC/SiC composite with 0.4 fiber volume ratio.

Fatigue and Fracture

Experimental Techniques Verified for Determination of Yield and Flow Surfaces

Many structural components are subjected to multiaxial loads when in service. For such components, a threshold surface is customarily used to distinguish irreversible response from reversible response. For elastoplastic materials, a yield surface can be used to delimit the elastic region in a given stress space. The concept of a yield surface is central to the mathematical formulation of a classical plasticity theory. However, at elevated temperatures, material response can be highly time dependent; thus, viscoplastic theories have been developed to account for the time dependency. Since many of these theories require experimental validation, our objective (Lissenden et al., 1996 and 1997) was to verify that current laboratory techniques and equipment are sufficient to determine flow surfaces at elevated temperatures.

By conducting multiple probes in axial-torsional stress space (fig. 1), we were able to define the yield and flow surfaces. A small offset definition of yield (10 $\mu\varepsilon$) was used to delineate the boundary between reversible and irreversible behavior so that the material state remained essentially unchanged and multiple probes could be made on the same specimen. The strain was measured with an off-the-shelf multiaxial extensometer that can measure the axial and torsional strains over a wide range of temperatures. The accuracy and resolution of the extensometer were verified by comparing the extensometer data with strain gauge data at room temperature. This showed the extensometer had sufficient resolution for these experiments. In addition, the amount of crosstalk (i.e., the accumulation of apparent strain in one direction when strain in the other direction is applied) was found to be negligible.

To determine flow surfaces at elevated temperatures, the tubular specimens were heated by induction heating, but the heating system induced a significant amount of noise in the data. However, by reducing thermal fluctuations and using appropriate data-averaging schemes, the noise was rendered inconsequential. Thus, accurate and reproducible flow surfaces (fig. 2) were obtained.

It is now possible to validate multiaxial, viscoplastic theories. Future work will be aimed at examining multiaxial effects in composites.

Glenn contacts: Brad Lerch, (216) 433–5522; and Rod Ellis, (216) 433–3340

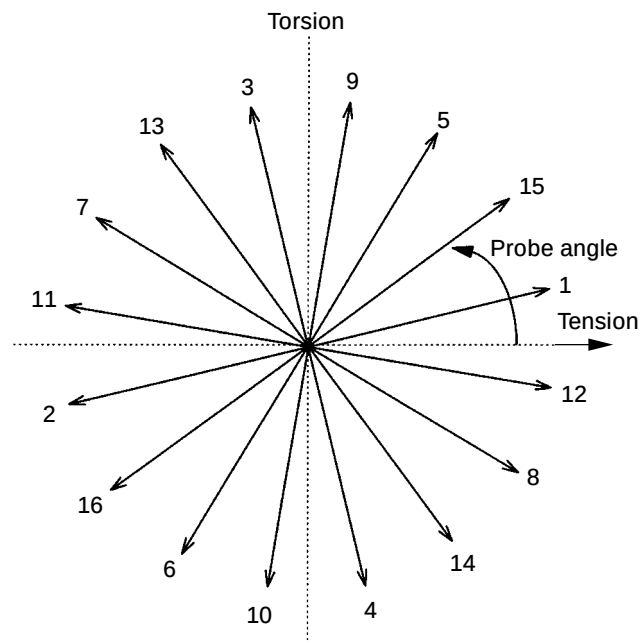

Probe number	Probe angle, deg	Probe number	Probe angle, deg
1	12	2	192
3	102	4	282
5	57	6	237
7	147	8	327
9	79	10	260
11	170	12	350
13	125	14	305
15	35	16	215

Figure 1.—Probes for determination of yield and flow surfaces.

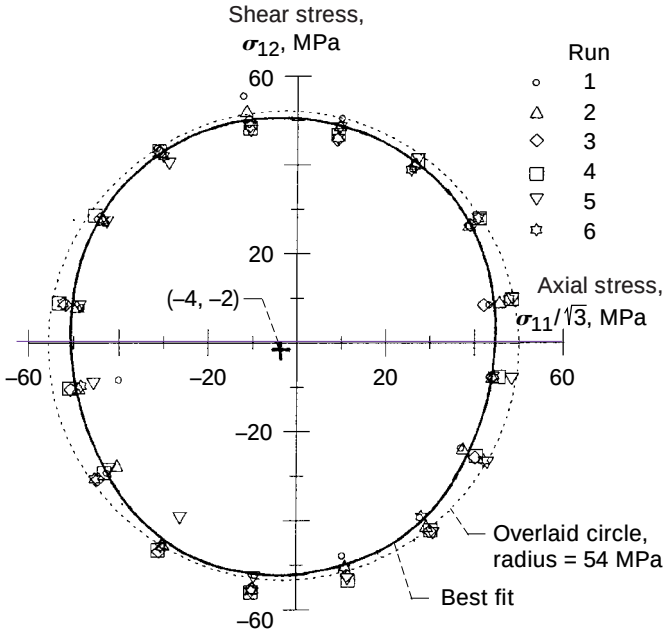

Figure 2.—Flow surfaces for 316 stainless steel at 650 °C. (Radius of flow surface, r; stress, σ_{ij}.)

Creep-Fatigue Behavior of Cast IN 939 Superalloy

Cast superalloys are being considered as high-temperature structural components for the exhaust system of the High Speed Civil Transport. These components are projected to experience service cycles that include hold periods under tensile stresses. Low cycle fatigue tests were used to assess the influence of dwell period on life.

Cast IN 939 (Inconel) specimens were subjected to load-controlled, elevated-temperature, tension-tension fatigue tests for hold times of 0, 1, 10, and 120 min at maximum load. A triangular waveform was employed. A computer-controlled, servo-hydraulic test machine was used for all the tests. The specimens were heated with a susceptor, which, in turn, was heated by an induction coil. All the tests were conducted at a homologous temperature of 0.7 (70 percent of the melting temperature).

The fatigue life progressively decreased with an increase in hold time. The average fatigue life at a hold time of 120 min was a factor of 300 shorter than the average life with no hold time. Specimens were examined after failure, to characterize the damage mechanisms. Figure 1 is a polished metallographic section of a specimen tested under continuous cycling conditions, and figure 2 shows a specimen tested by using a 120-min dwell. The loading direction was vertical. Under continuous cycling conditions, a flat, transgranular fracture path was observed, whereas the 120-min-hold-time test produced a tortuous, intergranular fracture surface. Hold times of 1 and 10 min resulted in both transgranular and intergranular regions on fracture surfaces. Thus, the change in the mode of fracture was the cause of the substantial reduction in the fatigue life as tensile hold time increased.

Glenn contacts: Michael Verrilli, (216) 433–3337; and Sreeramesh Kalluri, (216) 433–6727

(a)
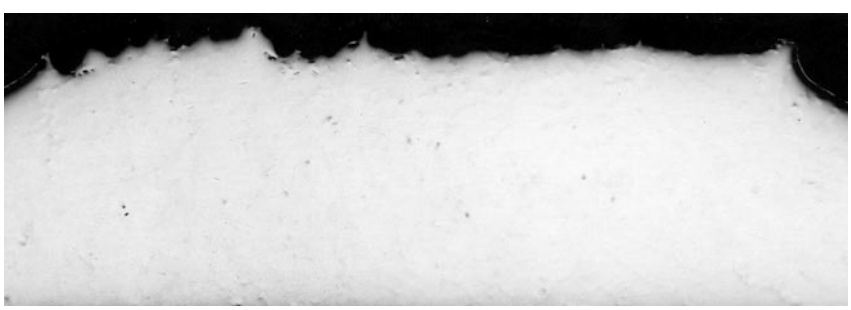

Figure 1.—Metallographic section of an IN 939 specimen tested under continuous fatigue cycling conditions.

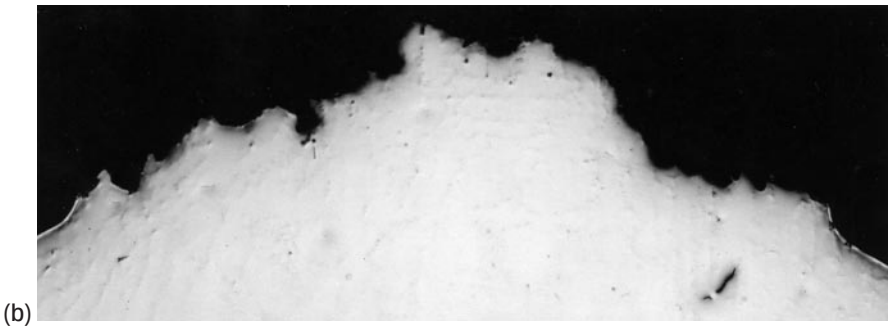

(b)

Figure 2.—Metallographic section of an IN 939 specimen tested using a 120-min dwell at maximum cyclic load.

Fatigue Crack Growth of Single-Crystal Superalloys in Hydrogen

A study was conducted to examine the effect of hydrogen on the fatigue-crack-growth behavior of a PWA 1480 (Pratt & Whitney Aircraft) single-crystal superalloy. The results showed a complex interrelationship between the fatigue-crack-growth behavior, hydrogen content, and the active failure modes. In the low stress intensity range (ΔK) regime, the same fatigue failure mode led to similar fatigue-crack-growth rates, regardless of hydrogen content. Although hydrogen did not significantly influence the fatigue-crack-growth behavior in the near threshold regime, as the ΔK increased it had a major influence in that it hindered a transition from a more damaging failure mode to a less damaging one. From this, we postulated that there is a distinct fatigue-crack-growth curve for each failure mode observed. Moreover, we suspect that the plateau regions (fig. 1) for which crack growth rates appear to be independent of ΔK are the result of transition from one fatigue-crack-growth curve to another because of the gradual change in failure modes. For more information, see Telesman et al. (1996).

Glenn contact: Jack Telesman, (216) 433–3310

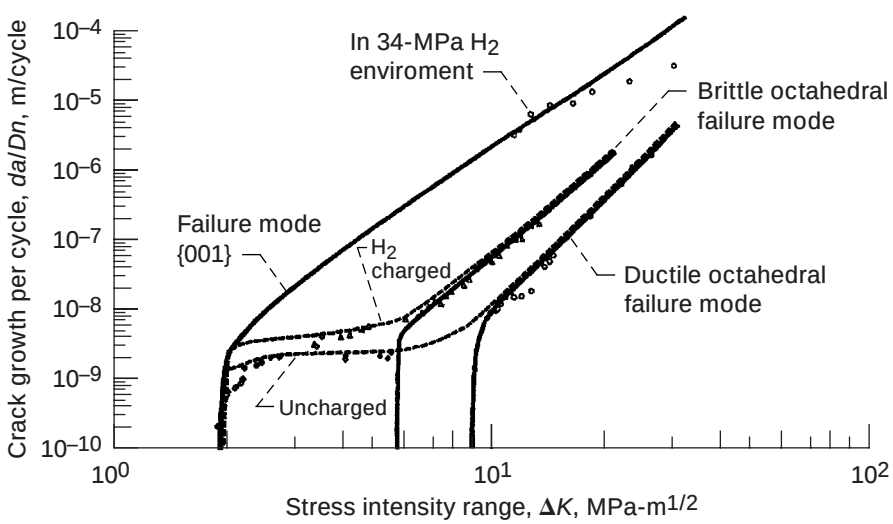

Figure 1.—Fatigue-crack-growth curves for different failure modes showing the onset of plateaus due to failure mode transition.

Reliability Modeling of Brittle, Anisotropic Solids

A general reliability model was developed for use in the design of structural components made from brittle, homogeneous anisotropic materials such as single crystals or materials with an anisotropic flaw distribution. This model incorporates a variable strength distribution and any equivalent stress criterion such as the coplanar energy release rate or the minimum strain energy density.

By considering the probability associated with a flaw existing in a component and the probabilities that the flaw has a specific orientation and a critical size, we derived the following reliability function for anisotropic materials:

$$P_F = 1 - EXP\left(-\frac{1}{A_o} \int_A \frac{1}{\pi} \int_0^{\pi} \left(\frac{\sigma_{Ieq}(\theta, \bar{x})}{\sigma_0(\theta)} \right)^m d\theta dA \right)$$

where $\sigma_{Ieq}(\theta, \bar{x})$ is the mode-I equivalent stress and $\sigma_0(\theta)$ is a function describing strength as a function of orientation. Strength as a function of orientation is shown in figure 1 for single crystal NiAl. This model is similar to the model frequently used for isotropic, polycrystalline ceramics, with two exceptions: (1) the strength in this case is a function of planar angle, and (2) an equivalent stress formulation defining coplanar extension for an anisotropic body is used.

The model is applicable to materials that exhibit anisotropy in both strength distribution and elasticity or just strength distribution. The strength anisotropy may result from either the distribution of flaws or the variation in fracture toughness with orientation.

In order to verify the model, uniaxial and biaxial strength data were generated from a single-crystal NiAl alloy developed by General Electric Aircraft Engine Co. The effect of test specimen volume is shown in figure 2. In the case of uniaxial loading, the model can predict the effects of test specimen volume on measured strength as a function of crystal orientation. Coding of the model for verification of the multiaxial predictive capability, via the biaxial test data, is ongoing. For more information, see Darolia et al. (1996) and Salem et al. (1998).

Glenn contacts: Jonathan Salem, (216) 433–3313; and Ronald Noebe, (216) 433–2093

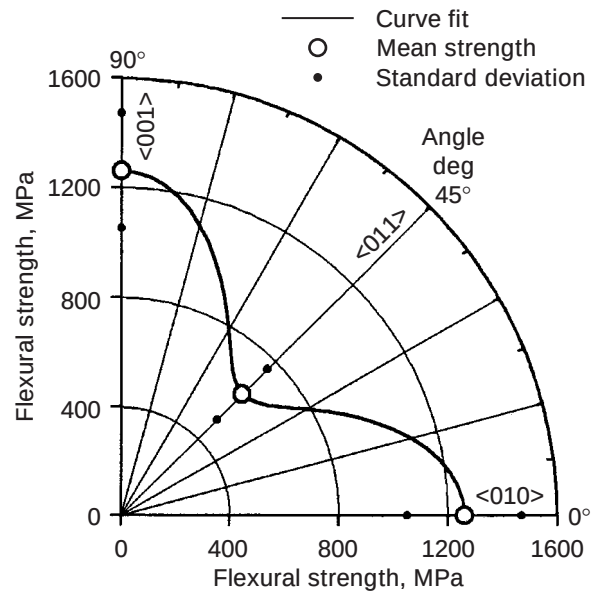

Figure 1.—Polar plot of flexural strength as a function of crystal orientation for single crystal NiAl

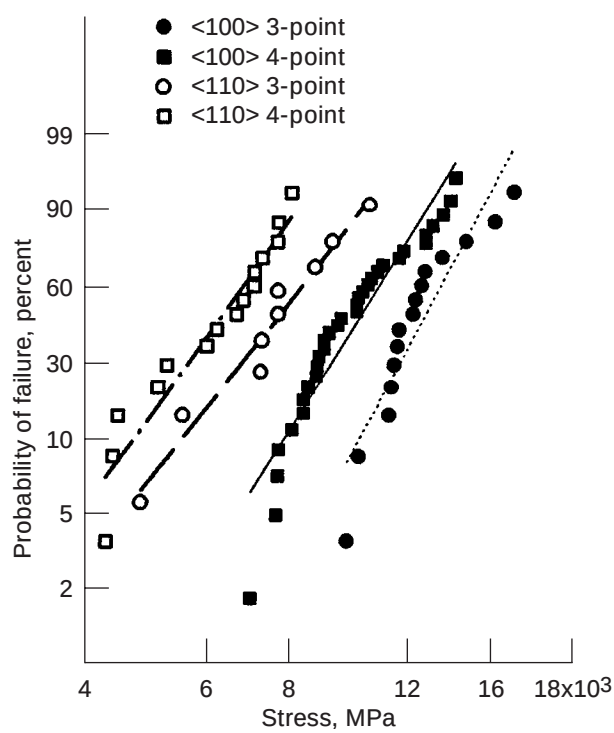

Figure 2.—Measured strength distribution for a single crystal NiAl alloy

Fatigue Behavior and Life Prediction of a T650-35/PMR-15 (0/90) Weave Under Isothermal Conditions

Currently, the gas turbine community is working toward advanced aircraft that will provide greater payload deliveries with corresponding increases in fuel efficiency. Of vital importance in the development of propulsion systems for these aircraft is the utilization of cost-effective materials. Among such materials are lightweight, high-temperature polymer matrix composites (PMC's). The load-bearing PMC structures are expected to perform at temperatures of 300 °C or higher, but few reports are available regarding the mechanical behavior and life prediction of woven layups at elevated temperatures (ET). Because of the new expectations, there is a need for data about the tensile, compressive, and fatigue characteristics of woven PMC's subjected to ET. The current investigation focused on the characterization of the monotonic tensile, compressive, and fully reversed fatigue ($R_\sigma = -1$) behavior exhibited by a T650–35/PMR–15, 8-satin harness (0/90) weave at room temperature (RT) and ET. The study documented the microscopic cracking events and their influence on macroscopic properties such as stiffness and residual compressive strength. The isothermal static and fatigue experiments were conducted at 22 °C and 316 °C. An analytical model, based on modulus degradation as a measurable damage variable, was implemented for damage and life prediction (Ye, 1989). The damage variable was defined as $D = 1 - E/E_o$ where E and E_o represent the residual and initial compressive moduli of the specimen, respectively. A power law relationship was utilized to describe the accumulation of damage:

$$\frac{dD}{dN} = A\,\frac{\sigma_{\max}^{C}}{BD^{B-1}} \tag{1}$$

where A, B, and C are material constants. Damage evolution and life prediction were determined by integrating equation (1). For life prediction, a definition of critical damage ($D_{critical}$) was required; it was assumed to be a function of load and temperature.

The temperature effects on the moduli and static tensile strength were minimal. At RT the averages for the longitudinal moduli were $E_{tensile}$ = 75 GPa and E_{comp} = 71 GPa; at ET they were reduced by only 2 percent. Similarly, the 22 °C static tensile strength and strain were 855 MPa and 1.15 percent, respectively, whereas at ET, tensile strength was reduced by 3 percent and compressive strength by 7 percent. The results for the ultimate compressive stress and strain at RT were –675 MPa and –1.12-percent strain. Fatigue lives, on the other hand, were negatively influenced by ET, as can be seen in figure 1. At both temperatures, failure occurred during compression because of the residual compressive strength's sensitivity to the environment and damage. Figure 2 displays the typical three-stage compressive modulus degradation behavior and its repeatability as evidenced by the three RT specimens. For modeling purposes, failure was defined as the final modulus value $D_{critical}$ before stage III behavior was initiated (see fig. 2). At this point each specimen had exhausted 98 percent of its life. For a given stress, both the RT and ET specimens followed the same degradation path, although the ET specimens failed before suffering much damage (i.e., modulus degradation). At RT, $D_{critical}$ values of the specimens typically exhibited a 16- to 22-percent modulus reduction, whereas for ET specimens the reductions in modulus before failure ranged from 5 to 9 percent. The characterization of equation (1) was achieved by using only the RT modulus data; this equation was observed to be dependent only on the applied stress. Recall that the modulus degradation rates were equivalent at the two temperatures; thus temperature dependence was introduced in the $D_{critical}$ function. We observed that $D_{critical}$ was a function of temperature and maximum applied stress. Figure 1 compares the model with the experimental data. The results indicate good agreement between the theory and the data at the temperatures used to characterize the model and at an intermediate temperature. The plateau of the curves is the point where no damage growth (i.e., modulus reduction) is detected before failure; these results also agree with the experimental observations. In summary, the temperature caused a degradation in properties that was dependent on the resin (e.g., monotonic compression and $R_\sigma = -1$ fatigue). Also, the residual modulus was shown to be a good indicator of damage and was successfully employed as a tool for life prediction.

Glenn contact: Andrew L. Gyekenyesi, (216) 433–8155

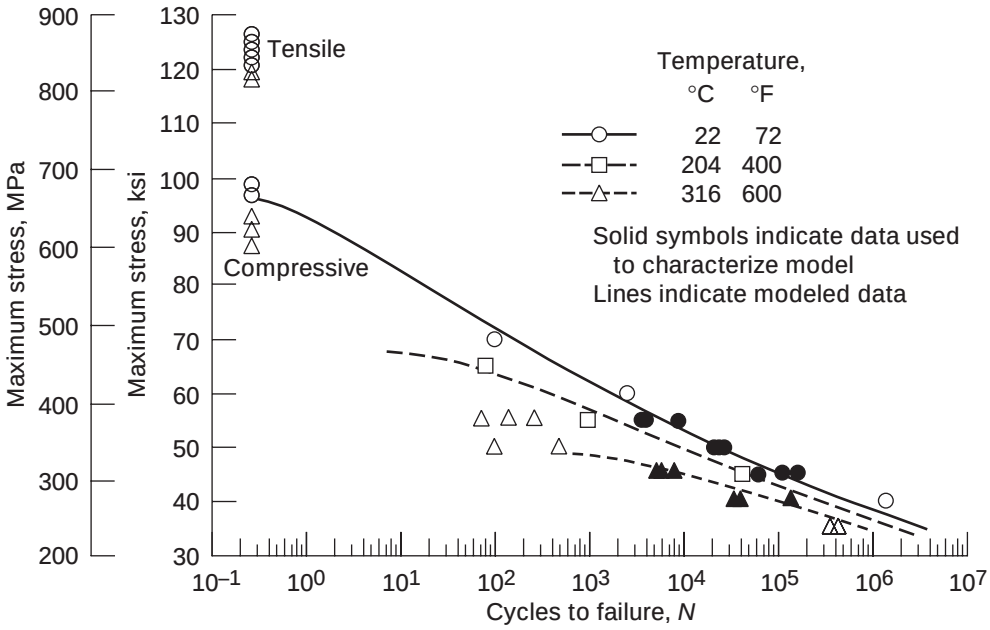

Figure 1.—Stress-based isothermal fatigue life comparison for T650-35/PMR-15 (0/90) weaves.

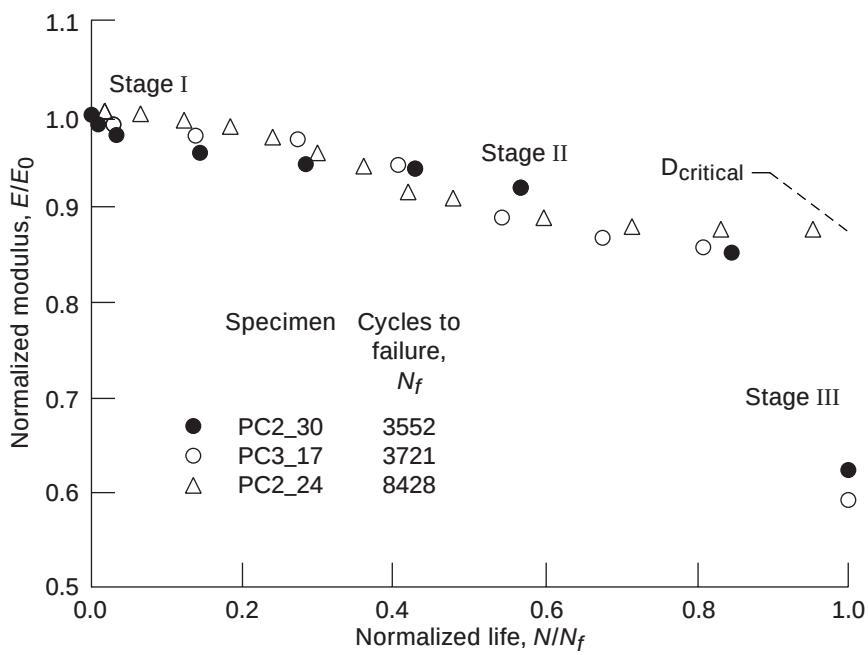

Figure 2.—Normalized compressive modulus degradation behavior for multiple specimens (σ_{max} = 379 MPa and temperature = 22 °C).

A General Representation Capturing Reversible and Irreversible Hereditary Behavior of a Titanium Alloy

A number of titanium matrix composite (TMC) systems are currently being researched and evaluated for high-temperature airframe and propulsion system applications. As a result, numerous computational methodologies to predict both deformation and life for this class of materials are under development. Integral to these methodologies is an accurate and computationally efficient constitutive model for the metal matrix constituent. In addition, because of the elevated temperatures at which these systems are designed to operate, such a model must account for both time-dependent and time-independent deformations.

To accomplish this, we employed a recently developed, complete potential-based framework (Arnold and Saleeb, 1992) that uses internal state variables and that was put forth for the derivation of reversible and irreversible constitutive equations. These reversible and irreversible domains are posited to be delineated by a temperature-dependent threshold surface, as illustrated in figure 1 for low-, mid- and high-temperature regimes. An example titanium alloy that has experimentally exhibited both a time- and temperature-dependent reversible (linear viscoelastic) and irreversible (viscoplastic) domain) (Arnold et al., Castelli, 1997) is TIMETAL 21S. Our previous work (Arnold et al., 1994 and 1995(b)) focused on the specification and characterization of the irreversible domain for this material. The

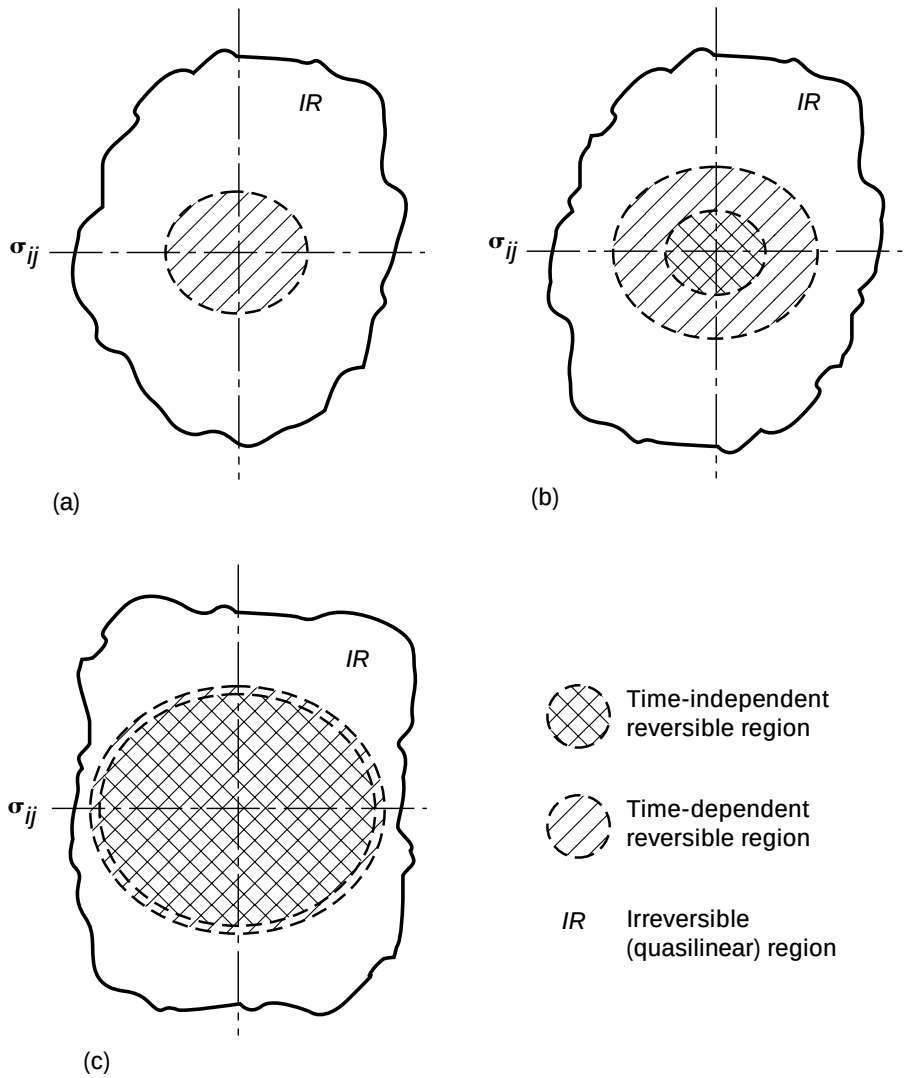

Figure 1.—Reversible and irreversible threshold surfaces (a) High temperature. (b) Mid temperature, (c) Low temperature.

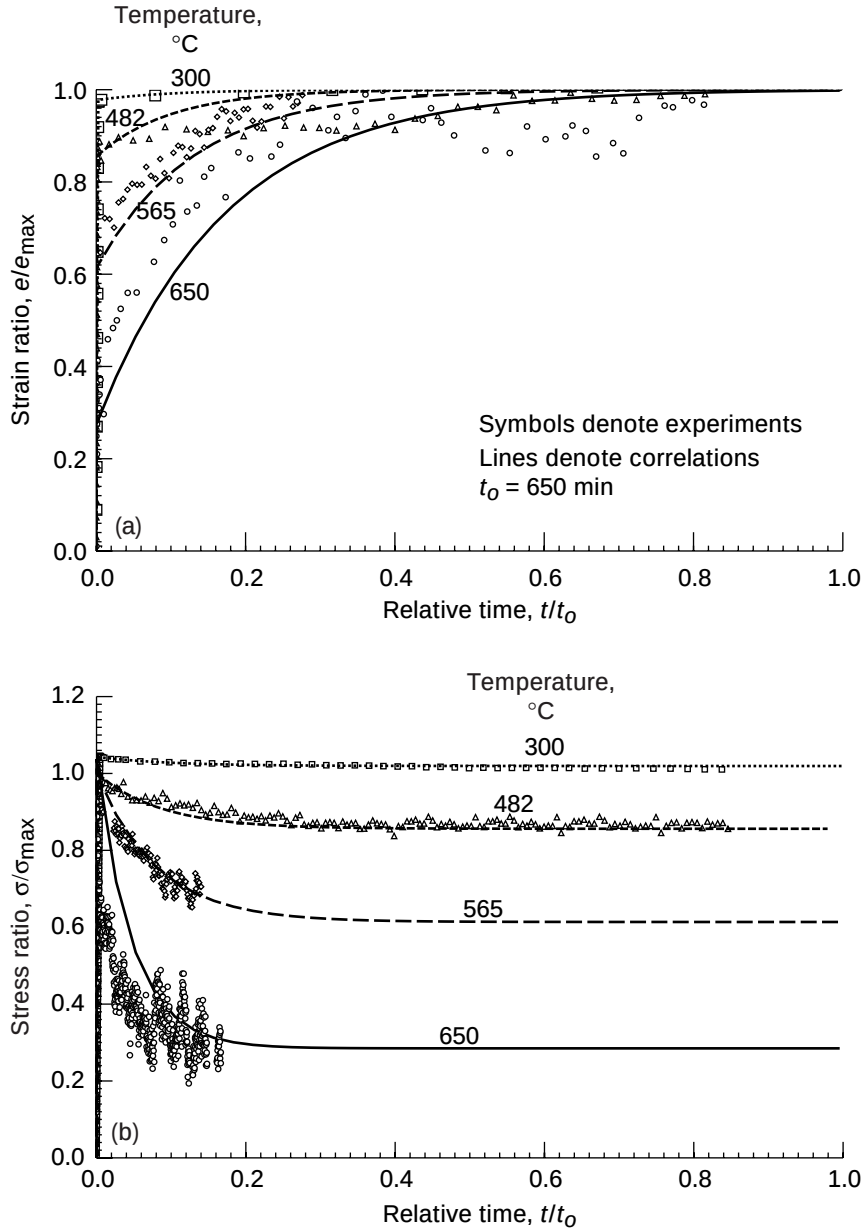

Figure 2.—Nonisothermal viscoelastic correlations with experiments. (a) Creep. (b) Relaxation.

primary objective of our present work is to construct, within the context of a complete potential structure, a multiaxial, nonisothermal viscoelastic model to describe the reversible strain component of the total strain decomposition. To construct a potential-based viscoelastoplastic mathematical framework, we had to specifically partition both the strain (reversible and irreversible) and stress (equilibrium and nonequilibrium) variables. By making the reversible portion of the model specific and assuming all mechanical elements (i.e., springs and dashpots) have the same Poisson ratio effect, we significantly reduced the required number of material parameters and characterization effort for the model. Thus, a successful nonisothermal characterization of this reversible viscoelastic model has been completed for TIMETAL 21S. The resulting normalized creep and relaxation response histories are shown, respectively, in parts (a) and (b) of figure 2, for four temperatures (300, 482, 565, and 650 °C).

Glenn contact: Steven M. Arnold, (216) 433–3334

Damage Mechanisms and Mechanical Property Degradation in Titanium Matrix Composites Subjected to TMF Loadings

Over the past decade, continuously reinforced titanium matrix composites have been the focus of many research programs aimed at evaluating these materials for high-temperature aeronautics and aerospace applications. Specifically, the use of theses materials in future supersonic and hypersonic flight vehicles and advanced propulsion systems is viewed as a critical enabling technology. Since the vast majority of such applications involve combined cyclic stress and temperature conditions, it is essential to characterize and evaluate material behavior under thermomechanical fatigue (TMF) loadings if the ultimate goal is to develop robust deformation and damage/life models applicable to in-service conditions.

Detailed examinations of TMF deformation, damage progression, and life behaviors have been completed and summarized for multiple laminates of continuous SiC-fiber-reinforced titanium matrix composites (Castelli, 1996). Fundamental behaviors resulting from in-phase (IP) and out-of-phase (OP) TMF loadings were addressed with particular emphasis on the micromechanical damage mechanisms leading to macroscopic failure. This was accomplished by using both fractography and metallography to examine microstructural details. In addition, macroscopic damage progression was determined on the basis of mechanical property degradation from data collected with an advanced TMF test technique (Castelli, 1994) that allowed explicit measurements of the macroscopic isothermal static moduli and the coefficient of thermal expansion (CTE) as functions of the TMF cycles.

Zero-tension TMF life results indicate analogous trends for both [0] and [0/90] titanium matrix composite laminates (see fig. 1). High stress IP TMF and mid- to low-stress OP TMF loadings are more life-limiting than maximum temperature isothermal conditions. The dominant damage mechanisms changed with cycle type. Damage resulting from IP

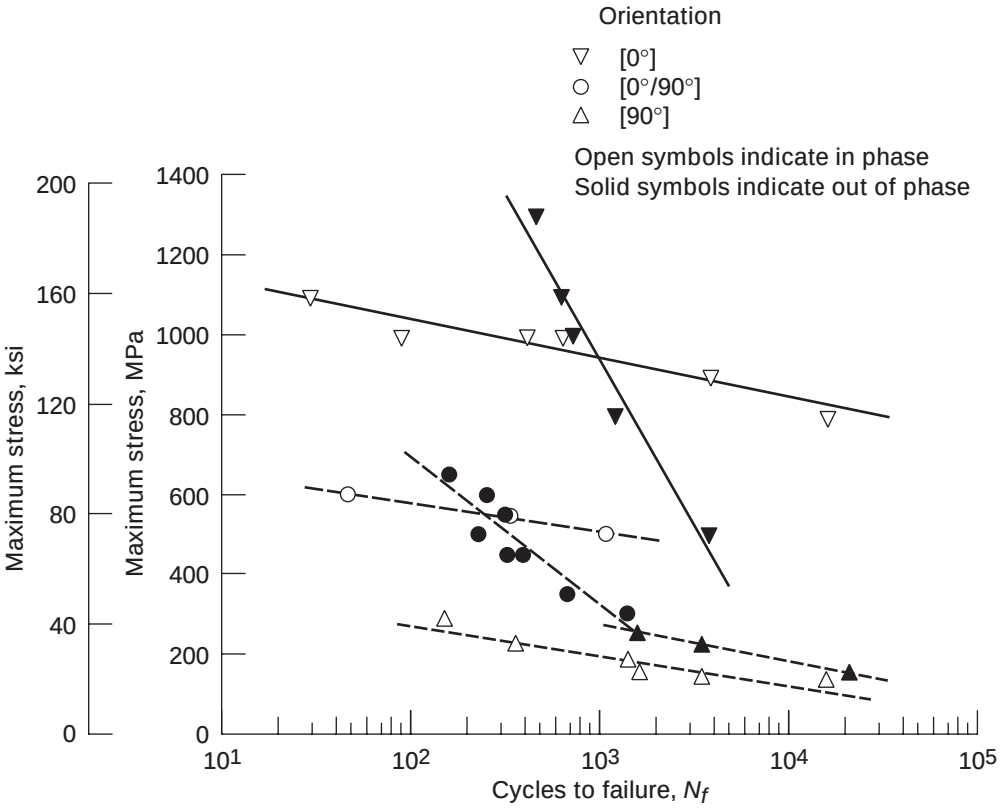

Figure 1.—Thermomechanical fatigue life behaviors of SiC-reinforced titanium matrix composite laminates.

TMF conditions produced measurable decreases in static moduli, but only minimal changes in CTE occurred. Microstructural damage is generally associated with [0] fiber cracking, sparse matrix damage, and no surface-initiated cracking. Under OP TMF conditions, notable static moduli and CTE degradations were experienced. Here, conditions promoted environment-enhanced surface-initiated cracking. The [0/90] titanium matrix composites also exhibited matrix cracking initiated at debonded [90] fiber/matrix interfaces. Both laminates showed little to no [0] fiber cracking under OP TMF. Zero-tension TMF of a [90] titanium matrix composite revealed significant changes in both the static moduli and CTE under IP and OP conditions. Mechanical property degradation patterns were very similar to those exhibited under isothermal loadings. Further, damage mechanisms promoted by isothermal, IP TMF, and OP TMF loadings were essentially identical, consisting of debonding at the fiber/matrix interface followed by matrix cracking that initiated at the debond and propagated transverse to the applied load. For more information, see Castelli (1996b), Castelli and Rao (1996), Verrilli and Castelli (1996a and b), Lei et al. (1996), and Arnold et al. (1994 and 1995a).

Glenn contact: Michael G. Castelli, (216) 433–8464

Structural Integrity

CARES/*Life* Ceramics Durability Evaluation Software for Finite-Element Analysis Programs

The CARES/*Life* program is a state-of-the-art software design tool that predicts the time-dependent reliability of monolithic ceramic components. The program has many features and options for materials evaluation and component design. Its capability, flexibility, and uniqueness has attracted many users representing a broad range of interests and has resulted in numerous awards for technological achievements and technology transfer.

CARES/*Life* is an integrated package that predicts the probability of a monolithic ceramic component's failure as a function of time in service. It couples commercial finite-element programs—which resolve

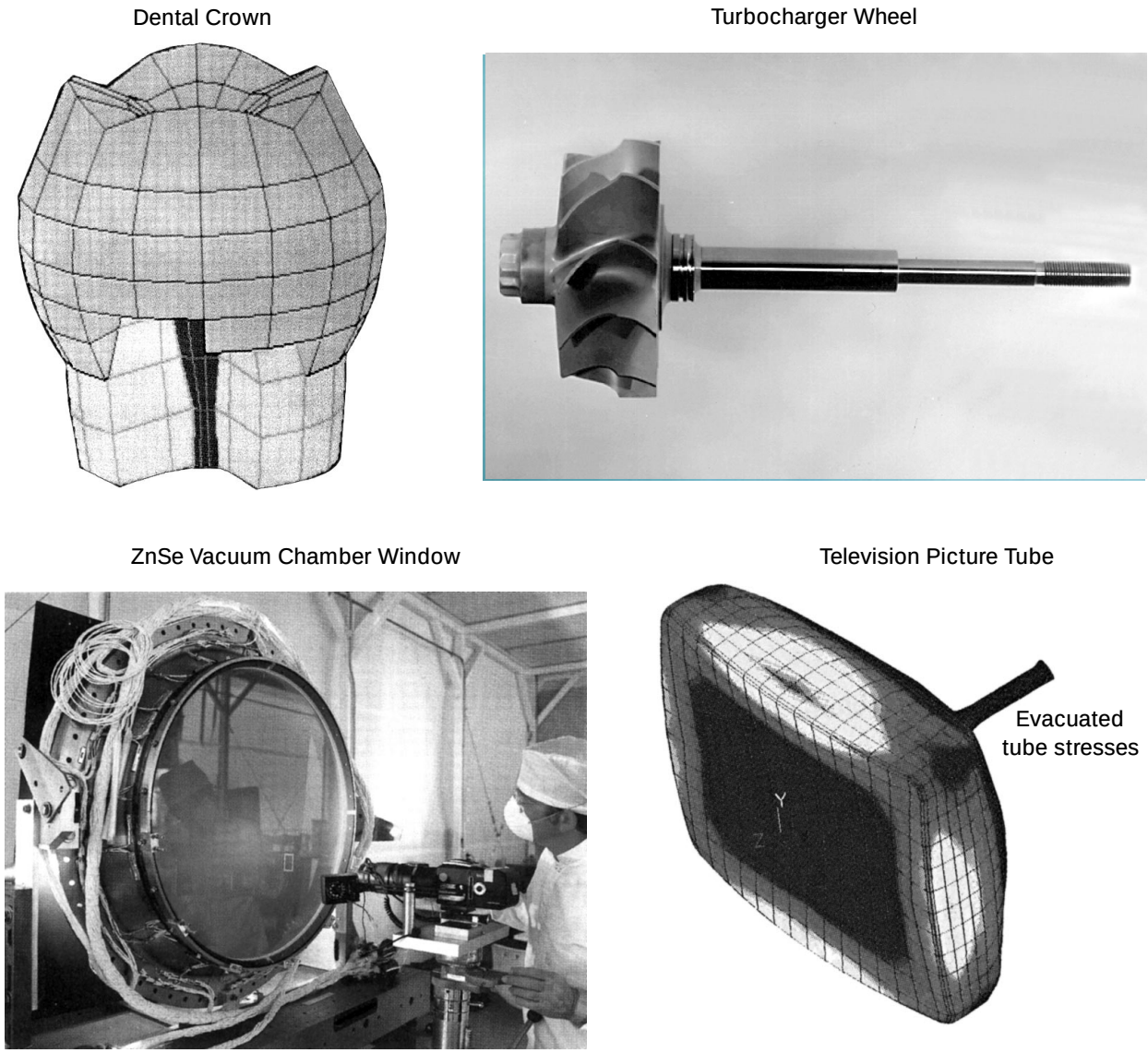

Figure 1.—Examples of components designed with CARES/Life.

a component's temperature and stress distribution—to reliability evaluation and fracture mechanics routines for modeling strength-limiting defects. These routines are based on calculations of the brittle material's probabilistic strength.

The key to maintaining interest in CARES/*Life* has been active maintenance and promotion of the program as well as enhancement of the program's ease of use. Towards this end the CARES/*Graphics*, and CARES/*Input* modules were created. CARES/*Graphics* enables the plotting of specimen rupture data and the corresponding regression lines that characterize the data. CARES/*Input* is an interactive input preparation program to CARES/*Life*. It helps to eliminate the bewildering array of input files and keywords confronting the user, performs error checking, and includes online explanations as appropriate. Incorporating the many suggestions from users and reviewers has significantly improved the CARES/*Input* program in 1996.

CARES/*Life* has continued to be in high demand worldwide, although present technology-transfer efforts are primarily focused on U.S.-based organizations. Success stories can be cited in numerous industrial sectors such as aerospace, automotive, biomedical, electronic, glass, and nuclear- and conventional-power generation industries. For more information, see Nemeth et al. (1996a and b), Salem et al. (1996), and Sokolowski et al. (1996).

Glenn contacts: Noel N. Nemeth, (216) 433–3215; Lynn M. Powers, (216) 433–8374; and Lesley A. Janosik, (216) 433–5160

Creep Life Prediction of Ceramic Components Subjected to Transient Tensile and Compressive Stress States

Since ceramics have desirable properties at high temperatures, there is interest in using them in structural applications such as advanced turbine systems. However, the design lives for such systems can exceed 10 000 hr. With such long life requirements, the stresses on the components must be kept relatively low. The combination of high temperatures and low stresses typically places failure mode for monolithic ceramics in the creep regime.

A design methodology for predicting the lifetimes of structural components subjected to multiaxial creep loading has been developed. This methodology utilizes commercially available finite-element packages and takes into account the time-varying creep stress distributions (stress relaxation). In this methodology, the creep life of a component is divided into short time steps, during which the stress and strain distributions are assumed constant. The damage D is then calculated for each time step on the basis of a modified Monkman-Grant creep-rupture criterion. For components subjected to predominantly tensile loading, failure is assumed to occur when the normalized accumulated damage at any point in the component is greater than or equal to unity.

Some ceramic components, such as vanes and rotors, are subjected to concurrent tensile and compressive stress fields. For such components, failure generally starts at or near the most highly stressed point and subsequently propagates across the section. The creep-rupture life for members subjected to concurrent tensile and compressive loading is divided into two stages. The first is called the stage of latent failure (damage initiation). During this stage, damage accumulates until it reaches unity at some point within the component and failure begins. (Hence, this portion of life represents the entire predicted life for predominantly tensile components.) Damage due to compressive stresses is assumed to be negligible, although in this methodology, it can be accounted for very easily if it is determined to be of any significance. Subsequently, the second stage, named the damage propagation stage, takes place. During this stage a damage front defined by the condition $D = 1$ will travel through the body or surface of the component. Component failure occurs at the end of this stage when its total load-carrying capacity is expended. In CARES/*Creep* (Ceramics Analysis and Reliability Evaluation of Structures/*Creep*), this means that failure is assumed to occur when $D = 1$ at the periphery of the expanded critical damage zone. The corresponding time will be the creep-rupture life for that component. This size of the critical damage zone corresponding to creep-rupture failure varies depending on the load conditions and component configuration. One way to estimate the duration of the propagation stage is to assume it is equal to the time required for the damage zone to penetrate the initial tensile stressed portion of the structure. An example of this technique applied to a flexure specimen, is shown in table I.

This creep-rupture life methodology has several advantages. First, it yields a cumulative damage map for the component, showing the critical locations where failure would originate; this can be very helpful in the redesign of such components. In creep-type loading applications, it is not a trivial task to predict the location of failure since the multiaxial stress components are redistributed as time elapses. Thus, failure does not necessarily occur at the location where stresses are highest at the beginning of loading or at the time of failure; it can take place elsewhere. A second advantage is that this design methodology could incorporate the primary creep strain effect into the analysis (thereby influencing the stress state), which could then predict shorter lives (conservative predictions) than can be predicted when only the secondary creep stain effect is used. The third advantage is that any equivalent stress criterion can be used to predict the component's life. Thus, as multiaxial creep data emerge in the future and we understand better how ceramics fail under such applications, the CARES/*Creep* code can be modified accordingly. Fourth, any creep-rupture criterion (continuum damage mechanics, Larson-Miller, minimum commitment method, etc.) can be utilized to compute damage and predict life. For more information, see Jadaan et al. (1996).

Glenn contacts: Lynn M. Powers, (216) 433–8374; and Lesley A. Janosik, (216) 433–5160

Table I.—FLEXURE SPECIMEN RESULTS

Initial maximum stress, MPa	Experimental failure time, hr	Damage initiation, hr	Predicted lifetime, hr
200	830	200	830
250	55	14.5	80
300	45	1.2	8.6
350	1.3	.12	1.3

Constitutive Theory Developed for Monolithic Ceramic Materials

With increasing use of advanced ceramic materials in high-temperature structural applications such as advanced heat engine components, the need arises to accurately predict thermomechanical behavior that is inherently time-dependent and hereditary—in the sense that current behavior depends not only on current conditions but also on thermomechanical history. Most current analytical life prediction methods for both subcritical crack growth and creep models utilize elastic stress fields to predict the time-dependent reliability response of components subjected to elevated service temperatures. The inelastic response of these material systems at high temperature has been well documented in the materials science literature, but this issue has been ignored by the engineering design community. However, from a design engineer's perspective, it is imperative to emphasize that accurate predictions of time-dependent reliability demand accurate stress field information.

Ceramic materials exhibit different time-dependent behavior in tension and in compression. Thus, inelastic deformation models for ceramics must be constructed in a fashion that admits both sensitivity to hydrostatic stress and differing behavior in tension and in compression. A number of constitutive theories for materials that exhibit sensitivity to the hydrostatic component of stress have been proposed; they characterize deformation by using time-independent classical plasticity as a foundation. However, none of these theories allow a different behavior in tension and in compression. Furthermore, these theories are somewhat lacking in that they are unable to capture the creep, relaxation, and rate-sensitive phenomena exhibited by ceramic materials at high temperature.

The objective of our effort has been to formulate a macroscopic continuum theory that captures these time-dependent phenomena. Specifically, we have focused on the inelastic deformation behavior associated with these service conditions by developing a multiaxial viscoplastic constitutive model that accounts for time-dependent hereditary material deformation (e.g., creep, stress relaxation, etc.) in monolithic structural ceramics. Using continuum principles of engineering mechanics, we have derived the complete viscoplastic theory from a scalar dissipative potential function. Constitutive equations for the flow law (strain rate) and evolutionary law have been formulated on the basis of a threshold function, identified here as F (see fig. 1), that is sensitive to hydrostatic stress and allows different behavior in tension and compression. For illustration, a set of threshold flow stress values has been adopted that roughly corresponds to values anticipated for isotropic monolithic ceramics. Specifically, the compressive uniaxial threshold stress value is σ_c = 2.00 MPa, and the tensile uniaxial threshold stress value is σ_t = 0.20 MPa. In addition, inelastic deformation is treated as inherently time-dependent, and a rate of inelastic strain is associated with every state of stress. Thus, creep, stress relaxation, and rate sensitivity are phenomena resulting from applied boundary conditions and are not treated separately in an ad hoc fashion.

Complete details of the model and its attending geometrical implications are presented in Janosik and Duffy (1998). A quantitative assessment has yet to be conducted since the material constants have not been suitably characterized for a specific material. Incorporating this model into a nonlinear finite-element code would provide industry a means to numerically simulate the inherently time-dependent and hereditary phenomena exhibited by these materials in service. This approach could make life prediction more accurate for structural ceramics used in high-temperature applications.

Glenn contacts: Lesley A. Janosik, (216) 433–5160; and Stephen F. Duffy, (216) 433–5626

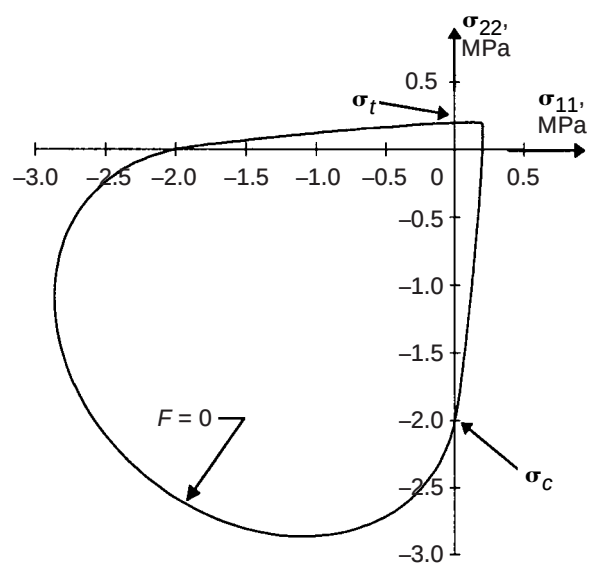

Figure 1.— Threshold function F, projected onto the $\sigma_{11} - \sigma_{22}$ stress plane.

Single Transducer Ultrasonic Imaging Method That Eliminates the Effect of Thickness in Imaging of High-Temperature Structural Materials

NASA Glenn Research Center Life Prediction Branch, in partnership with Sonix, Inc., and Cleveland State University, recently advanced the development, refinement, and commercialization of an advanced nondestructive evaluation inspection method entitled the Single Transducer Thickness-Independent Ultrasonic Imaging Method (Roth 1996; and Roth et al. 1996a and b). Selected by *R&D Magazine* as one of the 100 most technologically significant new products of 1996, the method uses a single transducer to eliminate in ultrasonic images of materials the effects of superimposing thickness variation (fig. 1). As a result, any variation seen in the ultrasonic image is solely due to microstructural variation. This method precisely and accurately characterizes material gradients (pore fraction, density, chemical) that affect the uniformity of physical performance (mechanical, thermal, electrical) for the material. Among the advantages of this method over conventional ultrasonic imaging are (1) elimination of machining costs (for precision thickness control) during quality control stages of material processing and development and (2) elimination of labor costs and the subjectivity inherent to further image processing and image interpretation.

At NASA, this method has primarily been used for accurate inspection of high-temperature structural materials such as monolithic ceramics, metal matrix composites, and polymer matrix composites. This year, data were published for plate-like samples, and the current research is focused on applying the method to tubular components.

Initial publicity about the development of this method has generated 150 requests for further information. These requests came from a wide variety of institutions and individuals, including the Federal Bureau of Investigation, Lockheed Martin Co., Rockwell International, Hewlett Packard Co., and Procter & Gamble. In addition, NASA has been solicited by the 3M Co. and Allison Abrasives to investigate the use of this method on composite materials manufactured by these companies.

Glenn contact: Don J. Roth, (216) 433–6017

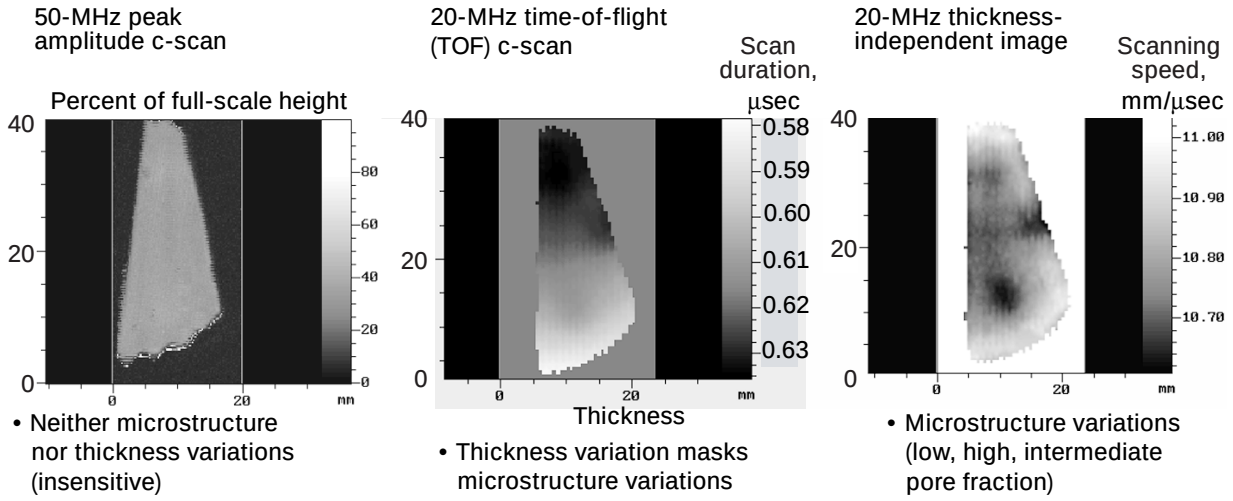

Figure 1.—Conventional ultrasonic imaging versus thickness-independent ultrasonic imaging of silicon nitride monolithic ceramic with pore fraction variations and 10-percent thickness variation.

Noncontact Measurement of Acousto-Ultrasonics for Ceramic Matrix Composites

Advancements in the processing and fabrication of ceramic matrix composites (CMC's) for use in engine components require appropriate mechanical and nondestructive testing methods. These methods are needed to characterize the properties, assess the integrity, and predict the life of engine components. Acousto-ultrasonics (AU) has demonstrated the capability to detect fatigue degradation of CMC's in experiments that caused matrix cracks to be formed and propagated in a manner typical of that caused by the mechanical stresses experienced during service (Periera et al., 1994; and Brewer et al., 1995).

The AU measurements performed for the cited work required contact coupling of the ultrasonic transducers to the surface of the specimens used. However, being able to do AU measurements without contacting the specimens would be more desirable. This would allow AU experiments to be done at high temperatures without the limitations imposed by the ultrasonic equipment. Beyond this, it would allow AU to be done on structures while they are in service. In this latter application, probes could be designed to monitor the health of aircraft engine parts.

For a number of years (Huber and Green, 1990) lasers have been under investigation as remote ultrasonic input sources and ultrasonic detectors. The use of ultrasonic transducers, coupled through an air gap, has also been studied for some time (Safaeinili, et al., 1995). At NASA Glenn we have been more successful in using the laser as an ultrasonic input medium than as an output device. On the other hand, we have been more successful using an air-coupled transducer as an output device than as an input device. For this reason, we have studied the combination of laser input with air-coupled transducer output.

With this laser-in/air-out noncontact combination, the first antisymmetric plate wave velocity in SiC/SiC specimens was successfully measured (Kautz, 1996). Figure 1 shows the noncontact measurement system. Tests of 18 specimens of 3 architectures measured by both this noncontact and a contact-coupling method gave the same results (see fig. 2).

Now the noncontact technique need to be extended to other AU measurements, such as ultrasonic decay, and to other material systems of interest in aeronautics, such as metal- and polymer-matrix composites. This future work will utilize higher intensity laser beams and more sensitive air-coupled transducers for better imaging of the ultrasonic signals that must be analyzed.

This AU technique, once calibrated to a composite system and component geometry, may be useful in predicting the life of aerospace components.

Glenn contact: Harold E. Kautz, (216) 433–6015

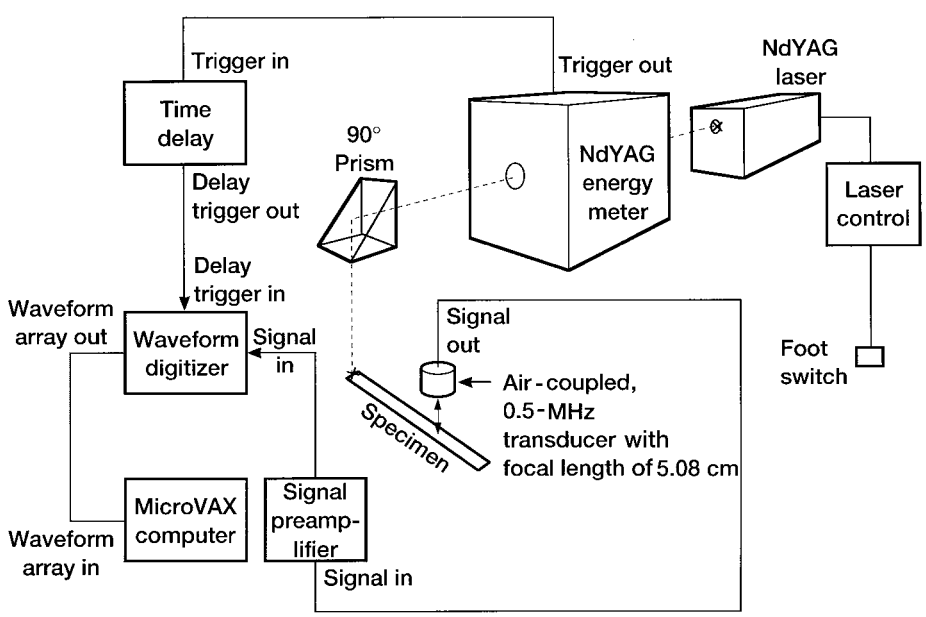

Figure 1.—Experimental arrangement for collecting laser-in, air-out acousto-ultrasonic waveforms.

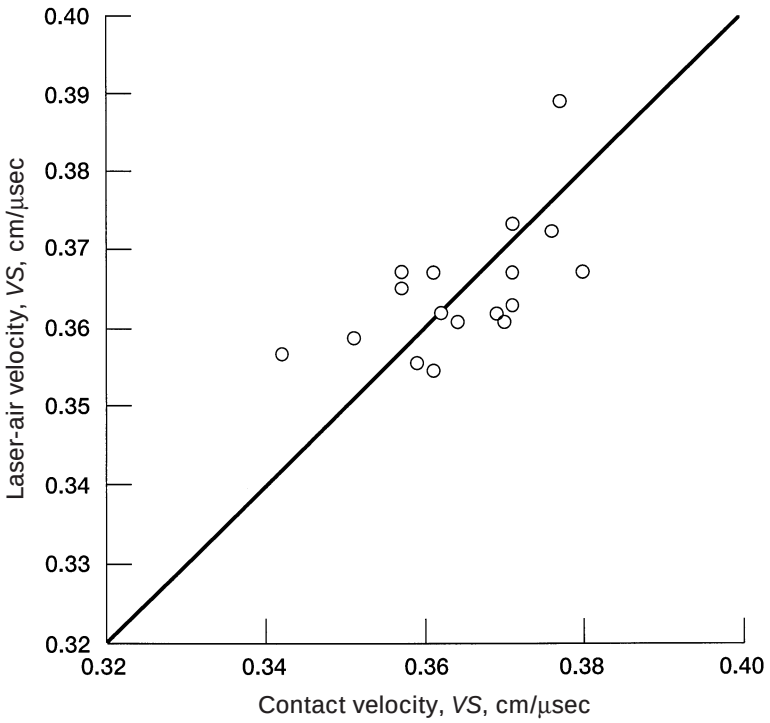

Figure 2.—Laser-air versus contact plate velocity,VS.

Structural Dynamics

Dynamic Spin Rig Magnetic Suspension

The Glenn Research Center's Dynamic Spin Rig, located in Building 5, test cell CW-18 (see fig. 1), is used to test turbomachinery blades and components by rotating them in a vacuum chamber. A team from the Machine Dynamics Branch successfully integrated a magnetic bearing and control system into the Dynamic Spin Rig (see fig. 2). This magnetic bearing worked very well to both support and shake the shaft. We demonstrated that the magnetic bearing can transmit more vibrational energy into the shaft and excite some blade modes to larger amplitudes than can the existing electromagnetic shakers. In cooperation with the University of California at San Diego, experiments conducted on damping of composite plates successfully demonstrated the system's robustness for long-term

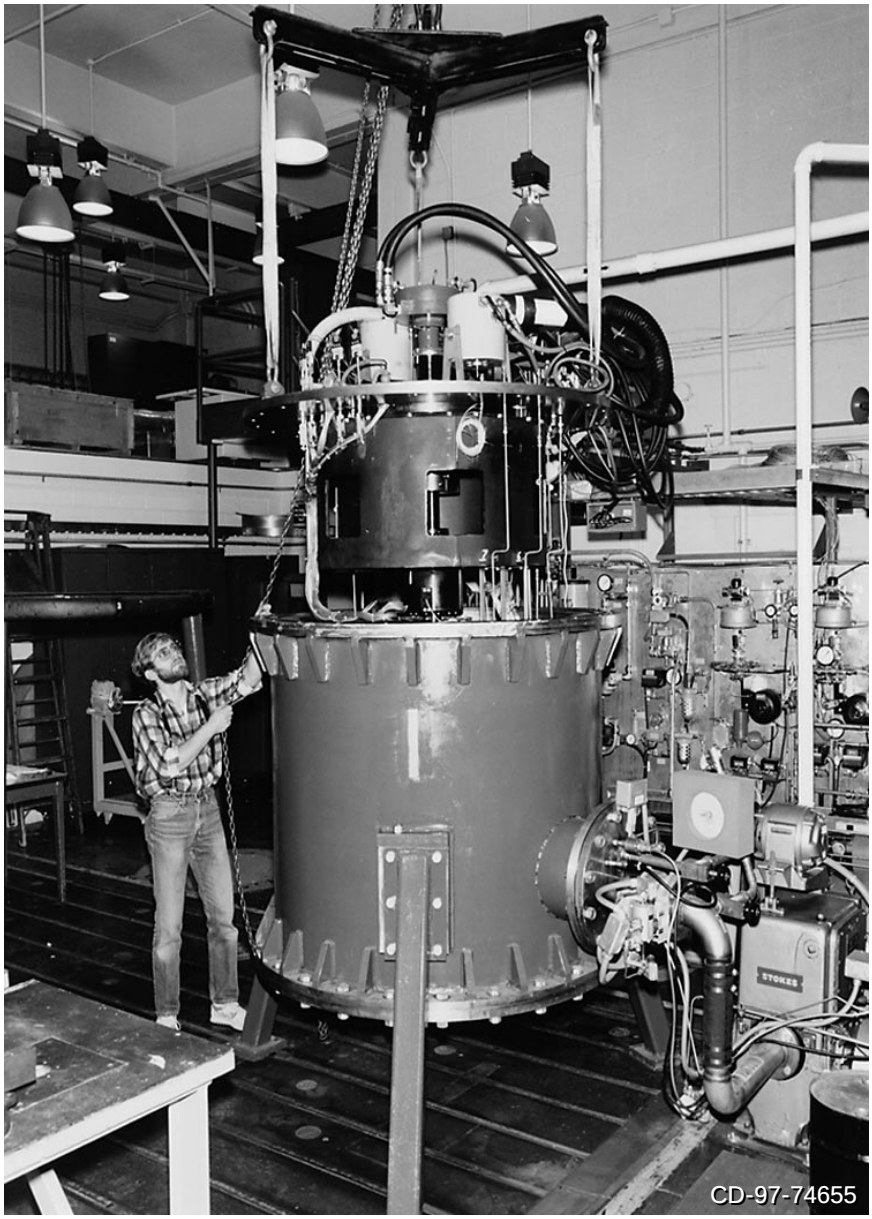

Figure 1.—NASA Lewis Dynamic Spin Rig Facility.

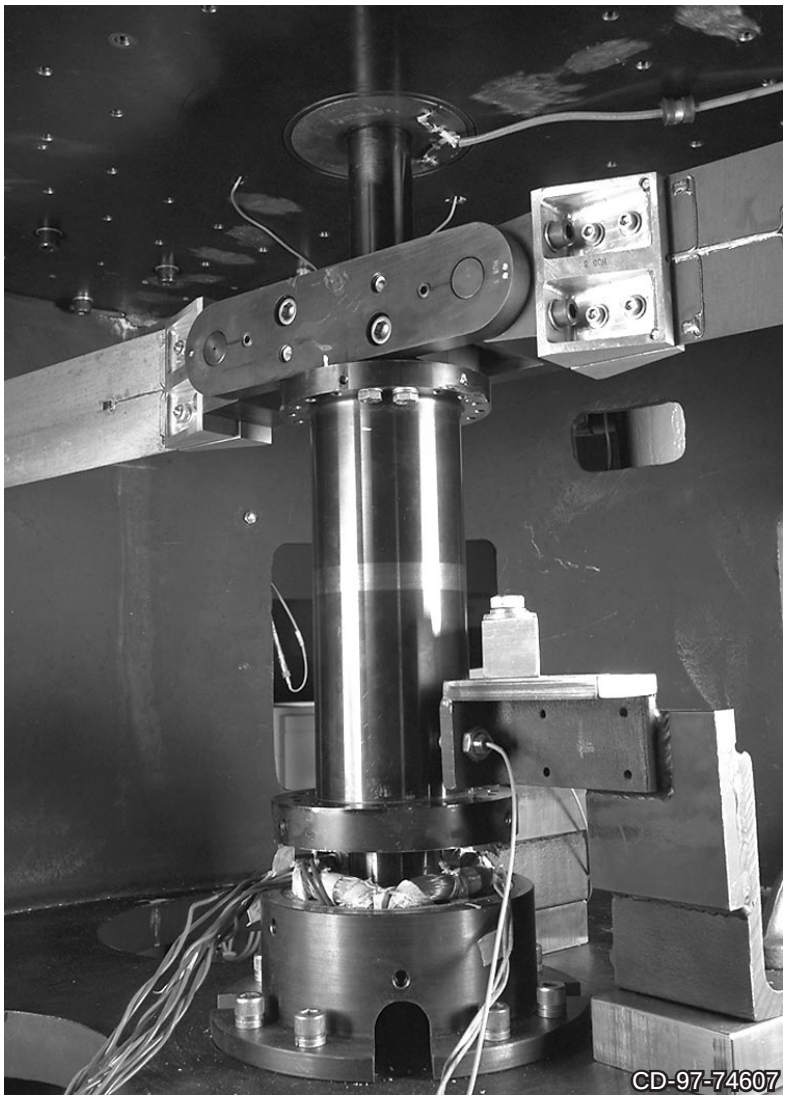

Figure 2.—Radial magnetic bearing in NASA Lewis Dynamic Spin Rig Facility along with viscoelastic damped composite plates attached to rotor.

testing. Existing magnetic bearing system hardware and software were modified to give enhanced capabilities. New features were added, for example, a user-friendly interface, and flexibility in orientation and phasing while applying the excitation force. We discovered that the bearing can also provide blade damping by using feedback from the blade strain gauges. This is an additional benefit since insufficient blade damping is a critical problem in advanced turbomachinery blades. The success of this initial work will lead to the design and implementation of a full magnetic suspension system for the Dynamic Spin Rig by September 1997. The facility can now provide either a mechanical or magnetic support system for rotors. The magnetic support will enable longer run times at higher speeds and larger vibration amplitudes for rotating blades.

Glenn contacts: Dexter Johnson, (216) 433–6046; Oral Mehmed, (216) 433–6036; and Gerald V. Brown, (216) 433–6047

High-Temperature Magnetic Bearings for Gas Turbine Engines

Magnetic bearings are the subject of a new NASA Glenn Research Center and U.S. Army thrust, with significant industry participation and cooperation with other Government agencies. The NASA-Army emphasis is on high-temperature applications for future gas turbine engines, so magnetic bearings could increase the reliability and reduce the weight of such engines by eliminating the lubrication system. They could also increase the DN limit (i.e., the diameter of the bearing times the revolutions per minute) on engine speed and allow active vibration cancellation systems to be used, thereby yielding a more efficient, "more electric" engine. In addition, the Integrated High Performance Turbine Engine Technology (IHPTET) Program, a joint Department of Defense-industry program, identified a need for a high-temperature (1200 °F) magnetic bearing that could be demonstrated in a phase-III engine.

The magnetic bearing being developed is similar to an electric motor. It has a laminated rotor and stator made of cobalt steel. Wound around the stator are a series of electrical wire coils that form a series of electric magnets around the circumference. The magnets exert a force on the rotor. A probe senses

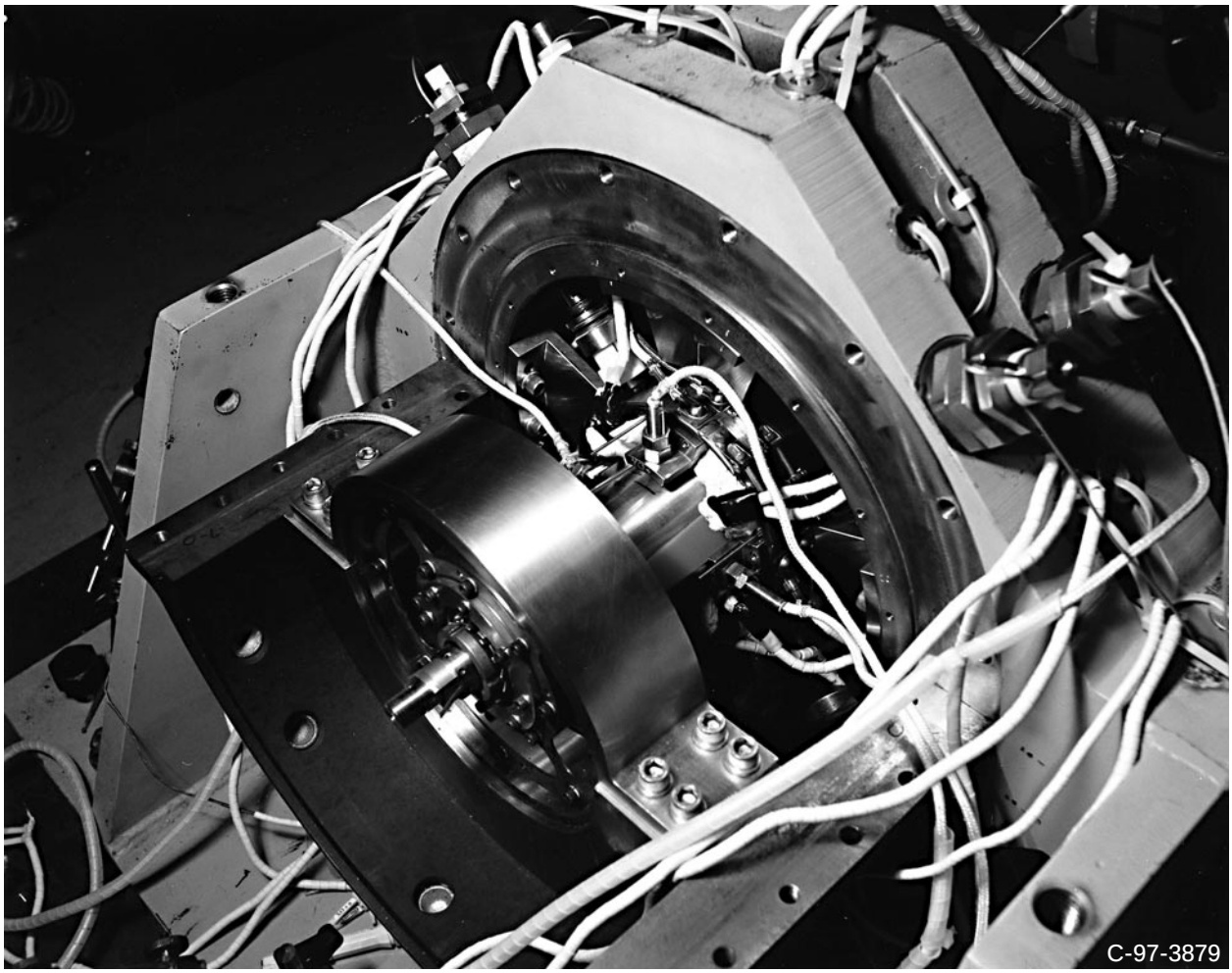

Figure 1.—NASA 1000 °F Magnetic Bearing Test Rig.

the position of the rotor, and a feedback controller keeps it centered in the cavity. The engine rotor, bearings, and casing form a flexible structure that accommodates a large number of modes. The bearing feedback controller, which could cause some of these modes to become unstable, can be adapted to varying flight conditions to minimize the seal clearances and monitor the health of the system.

Cobalt steel has a curie point greater than 1700 °F, and copper wire has a melting point beyond that. Therefore, practical limitations associated with the maximum magnetic field strength in cobalt steel and the stress in the rotating components limit the temperature to about 1200 °F. The objective of this investigation was to determine the speed and temperature limits of the magnetic bearing operating in an engine. Our approach was to make use of the Glenn expertise in magnets, mechanical components, high-temperature materials, and surface lubrication to build and test a magnetic bearing in both a rig and an engine. Testing would be done at Glenn or through cooperative programs in industrial facilities.

In 1995, we made significant progress. We initiated with Allison Engine a cooperative program to work on a high-temperature magnetic thrust bearing. During this work, we uncovered a problem with the conventional design of the magnetic thrust bearing: Because the thrust bearing was not laminated, it caused eddy currents that severely reduced the bandwidth. We also worked at Allison to bring their high-temperature magnetic bearing rig to full speed. In addition, we predicted the stability limits for both the inhouse and Allison magnetic bearings and tested a high-temperature displacement probe

Currently, our flexible casing rig is being converted to a high-temperature magnetic bearing rig (see fig. 1). Testing should start in the third quarter of 1997. Our plan is to develop a high-temperature, compact wire insulation and to fiber-reinforce the core lamination to operate at higher temperatures and DN values. We plan to modify our stability analysis and controller theory by including a nonlinear magnetic bearing model. We are developing an expert system that adapts to changing flight conditions and that diagnoses the health of the system. Then, we will demonstrate the bearing in our rotor dynamics rig and, finally, in an engine.

Glenn contacts: Albert Kascak, (216) 433–6024; and Gerald Brown, (216) 433–6047

Neural Network Control of a Magnetically Suspended Rotor System

Magnetic bearings offer significant advantages over conventional bearings because they do not contact other parts during operation, which can reduce maintenance. Furthermore, they are far superior because they offer higher speeds, no friction, no lubrication, weight reduction, precise position control, and active damping. However, there are technical barriers that limit the application of magnetic bearings in industry. One of them is the need for a nonlinear controller that can overcome the system nonlinearity and uncertainty inherent in magnetic bearings. For our work, a neural network was selected as a nonlinear controller because it generates a neural model without any detailed information regarding the internal working of the magnetic bearing system; it can even be used for systems that are thought to be too complex or where an accurate system model cannot be derived. A feed-forward architecture with a back-propagation learning algorithm was selected because of its proven performance, accuracy, and relatively easy implementation.

The neural network plant emulator was first trained to emulate a theoretical model of the nonlinear plant. A discrete theoretical model of the plant dynamics in state-space notation was used to choose both the present states of the plant (rotor displacement and velocity) and the plant input (control current) as input to the emulator. The next states, the rotor displacement and velocity after one sample time, were chosen as output from the plant emulator. During the learning procedure, the errors between the actual network output and the desired values were minimized by upgrading the weights. After training, the neural emulator perfectly predicted the next states (delayed by one sample time) of the magnetic bearing system for the current states and control force, which were not in the training sample data.

In the second step, the trained neural emulator was used to train a neural net controller to make the whole system meet conventional performance specifications such as bandwidth, settling time, overshoot, and such. We wanted the controller to take the current magnetic bearing states $x(t)$ and demand r as input parameters, and to deliver a control force $u(t)$ as output to the magnetic bearing

system. These current state values should make the magnetic bearing's next state vector $x(t + 1)$ be identical to that defined by the desired linear reference system, which satisfies the performance specifications in either the frequency or the time domain.

Figure 1(a) shows the Bode plot of a simple second-order linear reference model derived from frequency domain specifications; figure 1(b) shows the closed-loop magnetic bearing system after training. They are almost identical, even after 200 training epochs. Another neural controller based on time domain specifications was trained and tested by simulating its response for the initial condition and by comparing the results to the actual magnetic bearing response (see fig. 2). The neural network controller was so accurate that it perfectly overlapped the magnetic bearing response (+ symbols).

In summary, a neural network controller that circumvents the magnetic bearing's nonlinearity was developed and successfully demonstrated on a small Bentley-Nevada magnetic bearing rig. The neural plant emulator and neural controller were so accurate that the neural network controller did a nearly perfect job of making the nonlinear magnetic bearing system act like the linear reference model. This novel approach demonstrated the feasibility of using it for advanced turbomachinery systems with large-scale magnetic bearings of unknown dynamics.

Glenn contacts: Benjamin Choi, (216) 433–6040; Gerald Brown, (216) 433–6047; and Dexter Johnson, (216) 433–6046

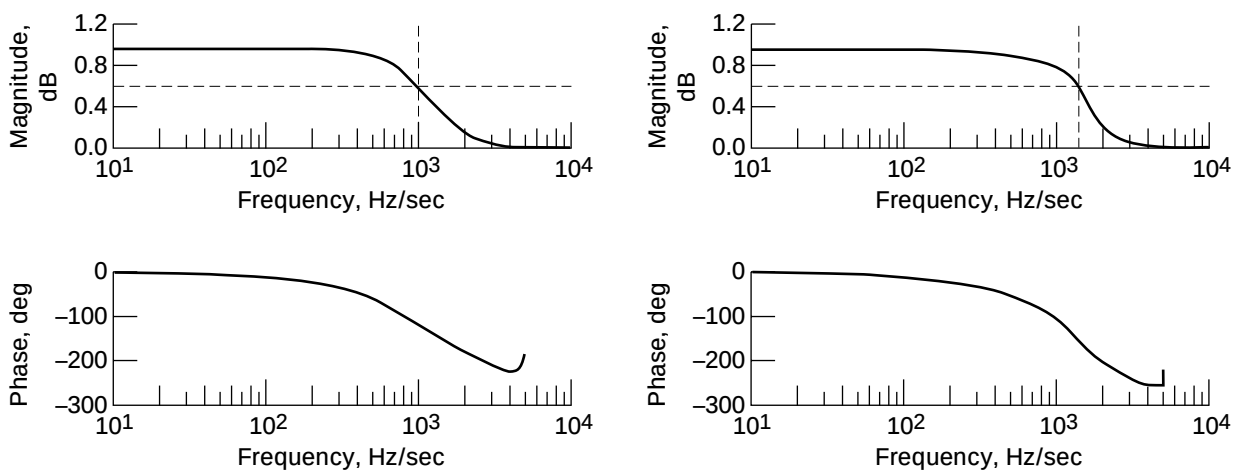

Figure 1.—Bode plots of desired and neural network models in frequency domain showing averaged transfer function. (a) Simple, second-order linear reference model (m_p = 1.1 and w_c = 1000 Hz). (b) Trained closed-loop system.

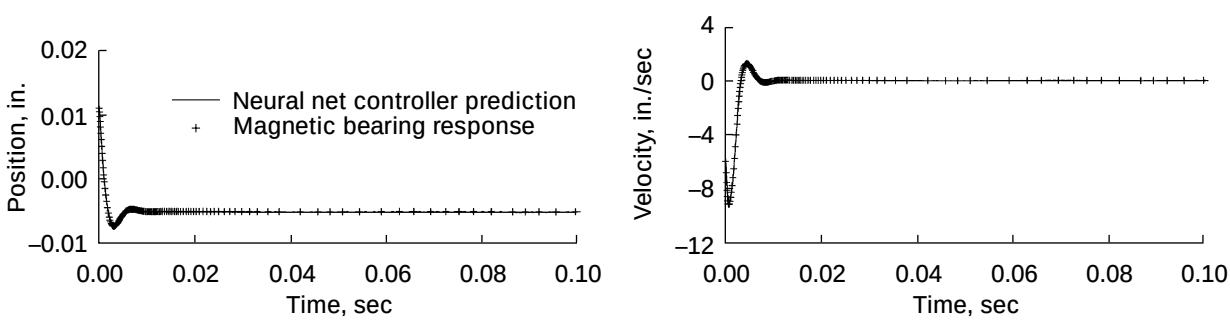

Figure 2.—Desired and actual trained, closed-loop system response for simple, second-order linear reference model in time domain. Overshoot, P_o, 4.3 percent; settling time, T_s, 0.0001 sec; initial rotor position, x_o, 0.011 in.; initial rotor velocity, x_o, 6 in./sec; and reference position of rotor, r_f, –0.005 in.

Damping Experiment of Spinning Component Plates With Embedded Viscoelastic Material

One way to increase reliability and durability of gas turbine engine blades is to reduce blade vibration. It is well known that vibration can be reduced by adding damping to metal and composite blade-disk systems. Toward this end, NASA Glenn and the University of California at San Diego jointly investigated the use of integral viscoelastic damping to reduce the vibration of rotating composite fan blades. The objectives of the experiment were to verify the structural integrity of composite plates with viscoelastic material patches embedded between composite layers while the plates were under large steady forces from spinning and to measure the damping and natural frequency variation with rotational speed.

Experimental data were obtained from in-vacuum vibration spin experiments of flat and twisted graphite composite plates damped by embedding 3M ISD 113 viscoelastic material patches between the composite layers. Figure 1 shows the rotor installation in the spin facility. The rotor has a tip diameter of 792 mm; the plates have an aspect ratio of 3 and a chord of 76 mm. Damping was calculated from measured transfer functions of blade base acceleration to blade strain. Damping was repeatable, and there were no failures or delaminations of the plates. This is significant since 3M ISD 113 has a low creep modulus at room temperature and the plates had centrifugal loads of up to 28 000 g at the tip. There was a great deal of centrifugal stiffening of the plates, which caused a significant drop in the damping ratios; however, the viscoelastic material damping remained nearly constant. Even though the damping ratios decreased, they were always greater than 2 times the damping ratios of undamped control plates. Real fan blades,

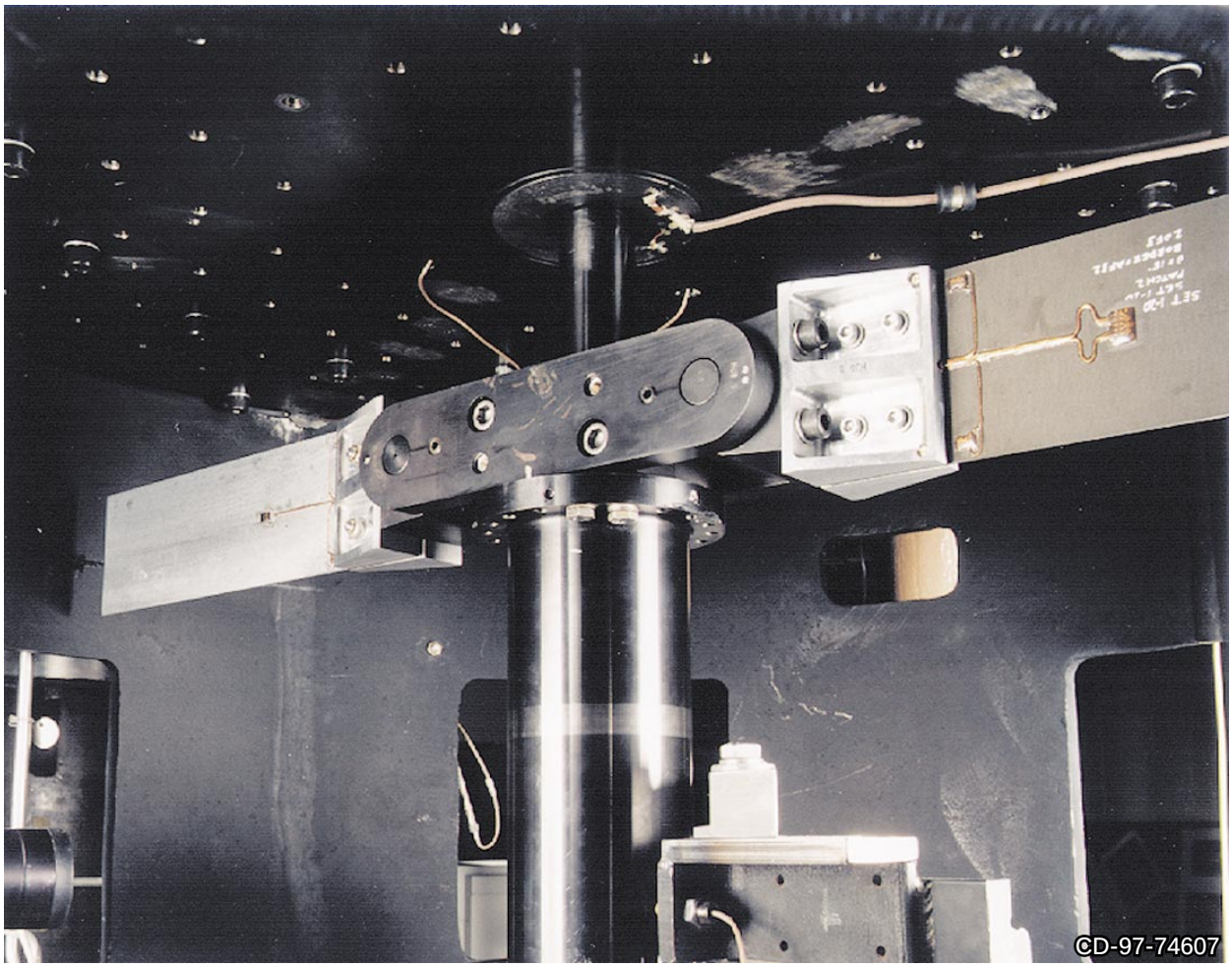

Figure 1.—Viscoelastic damped composite plates in the NASA Dynamic Spin Facility.

though, have smaller increases in natural frequencies with rotational speed, and therefore, the decrease in fan blade damping ratio should be smaller than that measured in this experiment.

From the results, we concluded that the presence of centrifugal forces, which are well known to increase blade bending stiffness and corresponding natural frequencies, will decrease the damping ratios. This occurs because as the blade stiffens the corresponding modal strain levels and strain energy in the damping material decrease, thus decreasing the modal damping ratios. To further improve damping, new designs should consider ways to increase the strain energy level in the viscoelastic material; for example, use a stiffer viscoelastic damping material than was used here. This study not only reveals the potential of integral viscoelastic material damping in composite fan blades, but it also illustrates that there are technical challenges that still must be overcome before such damping can be effectively used as a design option.

Glenn contact: Oral Mehmed, (216) 433–6036

Improved Dual Clearance Squeeze Film Damper for High Loads

Squeeze film dampers are widely used to control vibration in high-speed rotating machinery. However, when imbalance occurs at values appreciably above the design value (e.g., due to turbine blade loss), a conventional squeeze film will be overloaded and, thus, no longer effective in controlling vibration amplitudes and bearing forces. The dual clearance damper (fig. 1), characterized by two oil films separated by a sleeve, overcomes this problem. The sleeve is fixed in place for normal operation, and the thin inner damper film (typically about 0.1 mm) provides all of the damping. In the event of rotor blade loss or some other occurrence that increases the imbalance significantly, the sleeve is released by shearing of the pins holding it (see fig. 1) and the outer damper film becomes active. The two films then operate in series; that is, the bearing load is transmitted first through the inner film and then through the sleeve and outer film to the machine structure. The outer film has a larger clearance than the inner film to accommodate the larger vibration amplitude necessarily accompanying the higher imbalance. Sleeve mass, which was not accounted for in previous analyses, was found to be detrimental to damper performance. Inclusion of a spring support for the sleeve mitigated the effect of sleeve mass and markedly improved performance of the dual clearance damper.

A dual clearance damper was designed for a five-mass flexible rotor system. The rotor, 62 cm long with a mass of 5.7 kg, was assumed to have an imbalance of 290 g-cm distributed over the rotor length. For all cases in which sleeve mass was accounted for, the mass was taken as 360 g—about what it would be for aluminum.

For this rotor system, vibration amplitude is largest at midspan. In figure 2, midspan amplitude is plotted over a range of speeds for several conditions. The solid line represents the previously analyzed case, neglecting sleeve mass; its vibration is very close to that obtained with an ideal damper whose stiffness and damping are independent of amplitude and speed. When the sleeve mass was included, but not the spring support, vibration was somewhat lower at low speeds, but rose considerably higher at the rigid-support critical speed of 8280 rpm. Next, three spring stiffnesses were investigated. A stiffness of 0.18 MN/m (the dot-dash line) produced the lowest amplitudes overall; the peak vibration was not much higher than for the massless sleeve case. Higher spring stiffnesses resulted in progressively higher peak amplitudes.

The dual clearance damper, with proper spring support of the sleeve, holds the promise of providing good rotordynamic control of flexible shaft systems at both normal and extraordinarily large imbalances.

Glenn contact: David Fleming, (216) 433–6013

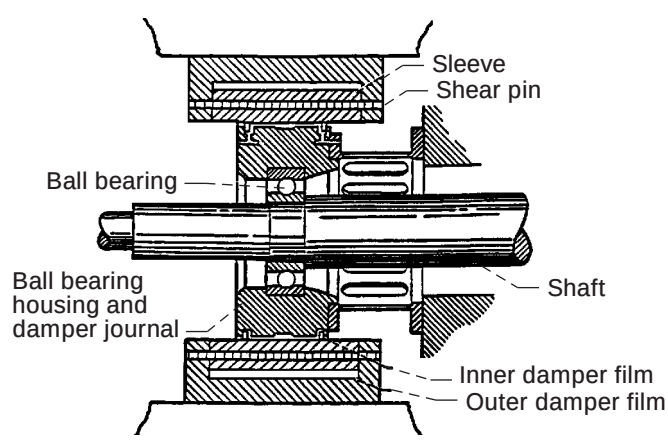

Figure 1.—Dual clearance squeeze film damper.

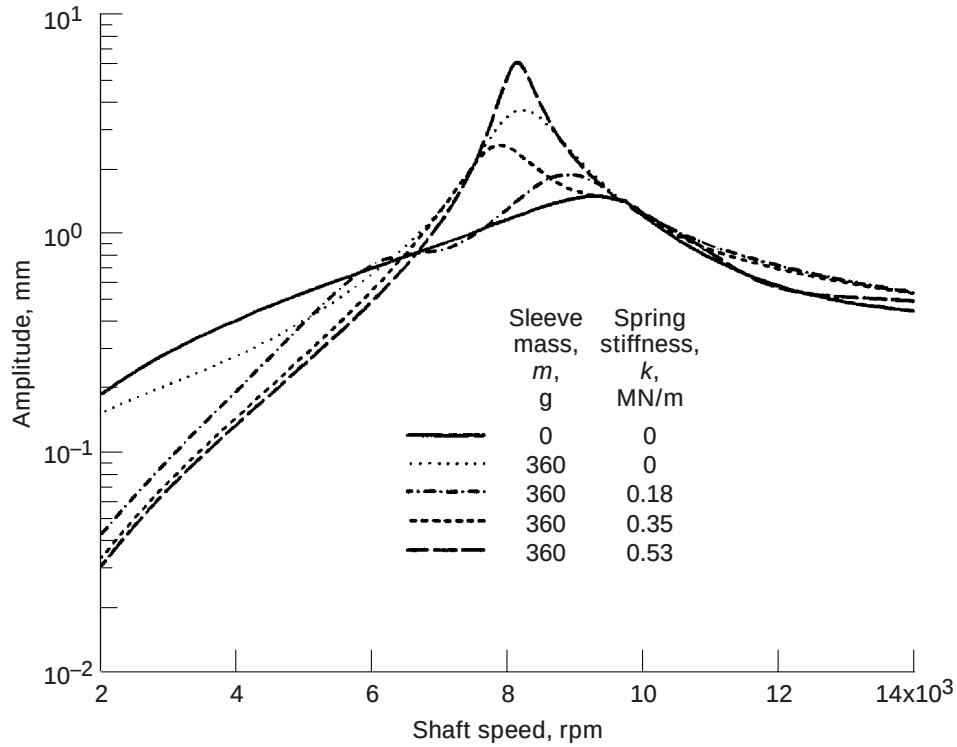

Figure 2.—Rotor midspan amplitude.

User's Guide for MSAP2D, an Euler Flutter and Forced-Response Analysis Code for Multistage Turbomachinery

Most of the current aeroelastic analyses for turbomachines analyze only one blade row (i.e., an isolated blade row). The multistage effects, those due to the presence of other blade rows, have been neglected or included in an approximate manner. Prediction of flutter and forced-response characteristics of turbomachinery blades requires that the multibladed-row turbomachine be accurately analyzed as a single unit. Towards this goal, an aeroelastic program, MSAP2D, was developed. The program can be used to analyze unsteady aerodynamic and aeroelastic characteristics of multiblade rows, such as compressor or turbine stages. In addition, it can be used for an isolated blade row as well.

In this program, the unsteady aerodynamic forces are obtained by using a finite volume method with a combination of flux vector splitting and flux difference splitting to solve two-dimensional Euler equations. The Euler solution scheme is third-order accurate in space and second-order accurate in time. The flow equations are solved on one or more passage-centered H-grids. The interface boundary between the blade rows is handled as an additional fluid boundary; it is updated explicitly after the interior of the computational domain is updated. The structural model is a typical section with bending and torsional degrees of freedom for each blade in the blade row and for all blade rows. The aeroelastic equations are solved in the time domain by using Newmark's method. This program has been calibrated for several examples.

We have written a user's guide to help the user prepare the input data file required by the MSAP2D code. The user's guide completely describes the input data, and gives the input and output information for three examples from published papers. References directing the user to detailed explanations of the aerodynamic analysis, the numerical algorithms, and the aeroelastic analysis are provided in the manual. A job control file for executing the program on the Cray-YMP computers is also included.

Glenn contacts: Tondapu S.R. Reddy, (216) 433–6083; Rakesh Srivastava, (216) 433–6045; and Oral Mehmed, (216) 433–6036

User's Manual for ASTROP2, Version 2.0, a Program for Aeroelastic Stability Analysis of Multiblade Structures

Flutter is an aeroelastic instability that must be considered in designing a safe aircraft engine. Flutter in fan, compressor, or turbine blading can cause delays in the development of new engines, and a consequent increase in developmental costs. ASTROP2 (aeroelastic stability and response of propulsion systems—two-dimensional analysis) is an aeroelastic code that can perform flutter analysis of rotating propfan, compressor, and turbine blades. It was developed as part of a project aimed at developing advanced propellers for aircraft capable of cruising at 0.8 the speed of sound.

To formulate the aeroelastic eigenvalue equations, the code uses strip theory to combine the unsteady aerodynamic forces due to vibrating blades with the blade structural characteristics. The stability information (flutter frequency and damping) is inferred from the eigenvalues obtained from these equations. In ASTROP2, the unsteady aerodynamic forces are obtained from two-dimensional cascade theories, and the structural characteristics are obtained from a three-dimensional structural model. An interface with NASTRAN is included in the program; however, the interface can be modified to suit any structural program. The program requires minimal computational resources, and it can be used in a desktop workstation setting.

In version 2.0, flutter analysis is performed by two separate programs: (1) 2DSTRIP, a program that calculates the structural dynamic information at selected stations, called strips; and (2) 2DASTROP, a program that calculates unsteady aerodynamic force coefficients and the aeroelastic stability. This allows users to check their structural model and aerodynamic model separately. In Version 1.0 of ASTROP2, these two steps were performed in a single program. Other improvements to version 2.0 include an option to account for counterrotation, improved numerical integration, accommodation for nonuniform inflow distribution, and an interative flutter calculation for frequency convergence. The ASTROP2 program is written in FORTRAN 77; the current version (2.0) has been run on a Cray computer and a Silicon Graphics Indigo2 workstation. It is now available through COSMIC.

The user's manual for version 2 of ASTROP2 completely describes the input data required and gives the input and output for a propfan that fluttered during wind tunnel testing. References directing the user to detailed explanations of the aerodynamic analysis, the numerical algorithms, and the aeroelastic analysis are provided in the manual. A job control file for executing the program on the Cray–YMP is also given.

Glenn contacts: Tondapu S.R. Reddy, (216) 433–6083; and John M. Lucero, (216) 433–2684

Using an Euler Aeroelastic Solver to Analyze Gust and Structural Response of a Two-Dimensional Cascade

The forced response from a nonuniform, unsteady gust caused by upstream blade rows, and aeroelastic instability are two areas that must be considered in the safe design of turbomachines. To our knowledge, there is no code in the open literature that includes gust response calculation, rotor-stator interaction, and structural (aeroelastic) response calculation in a single program. To fill this void, the multistage aeroelastic analysis program MSAP2D was modified to include gust response analysis. This was done by prescribing the unsteady inflow conditions at the inlet and using one-dimensional nonreflecting boundary conditions. Then these modifications were validated by comparing the predicted unsteady pressure and phase angles with measured data.

The unsteady aerodynamic forces are obtained by using a finite volume method with a combination of flux vector splitting and flux difference splitting to solve two-dimensional Euler equations. The Euler solution scheme is third-order accurate in space and second-order accurate in time. The flow equations are solved on one or more passage-centered H-grids. The structural model is a typical section with bending and torsional degrees of freedom for each blade in the cascade. The aeroelastic equations are solved in the time domain by using Newmark's method.

Figure 1 plots the amplitude and phase of the unsteady pressure coefficient on the lower surface of the turbine airfoil as a function of the chord fraction. The Mach number is 0.27, and the flow enters axially and turns about 40°. The steady inflow angle is 2.98°, and the reduced frequency of oscillation based on the chord is 10.0. The

amplitudes of the unsteady pressures compare reasonably well with measured data. The phase comparisons are fair in the regions where amplitudes are higher, but are poor in the area of lower amplitudes. However, predictions for the upper surface and for a Mach number of 0.2 showed poor to fair correlation; thus, this needs further investigation.

Glenn contacts: Tondapu S.R. Reddy, (216) 433–6083; Rakesh Srivastava, (216) 433–6045; and Oral Mehmed, (216) 433–6036

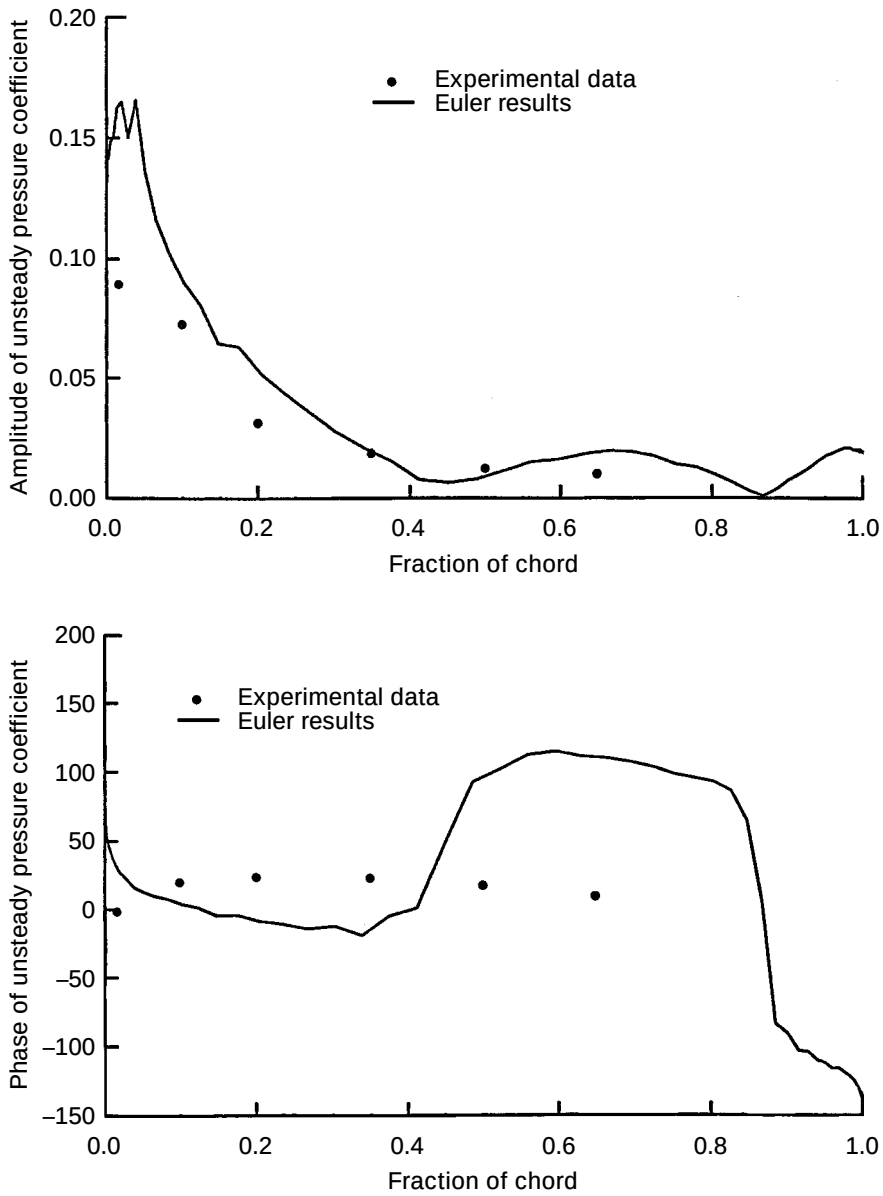

Figure 1.—Characteristics of unsteady pressure coefficient on lower surface as a function of chord fraction. (a) Amplitude. (b) Phase angle. (Mach number = 0.27, reduced frequency based on chord = 10.0; angle of attack = 2.98°; gap-to-chord ratio = 0.9744, phase angle = 0.0°.)

Flutter Analysis of Ducted Rotors

An aeroelastic analysis procedure (DuctE3D) has been developed to investigate the flutter in turbomachines. DuctE3D determines the unsteady airloads on vibrating blades by solving three-dimensional unsteady Euler equations and obtains the blade structural properties from a three-dimensional finite-element model. The duct is assumed to be infinitely long and structurally rigid. Any number of structural modes of vibration of the blades can be included in the analysis. The aeroelastic equations are formulated in normal mode and are then solved for flutter by using a frequency domain analysis technique for all possible interblade phase angles. For verification purpose, the analysis was applied to a ducted fan configuration of a propfan enclosed within an infinitely long and structurally rigid duct.

The three-dimensional Euler equations are solved with an implicit-explicit hybrid scheme. Since only two matrix inversions are required, as opposed to three for fully implicit schemes, this scheme saves large amounts of CPU time and requires much less memory. The structural analysis is carried out by using the normal mode approach and assuming the hub and duct to be rigid. The flutter analysis is carried out by moving one of the blades from steady state in a prescribed pulse motion and obtaining the unsteady aerodynamic forces on all the blades. These forces are then superposed, and the roots of the aeroelastic equation are obtained by solving an eigenvalue problem. The roots provide a measure of aerodynamic damping at the combined aeroelastic frequency. Negative aerodynamic damping would imply that the blade will extract energy from the surrounding air and, thus, indicates instability. Any number of normal modes can be included in the analysis. A single run is sufficient to provide information about the blade aeroelastic characteristics for the particular flight condition for each mode of interest.

The analysis was applied to an eight-bladed, ducted fan, the SR3C-X2 propfan enclosed in a rigid cylindrical duct. This propfan, in the unducted configuration, showed flutter in the wind tunnel tests at NASA Glenn at a freestream Mach number $M_\infty = 0.6$ for the eight-bladed configuration operating at an advance ratio $J = 3.55$ and setting angle $\beta = 61.2°$. The analysis was carried out at $M_\infty = 0.5$ by using the first three normal modes for a tip gap of 0.4 percent of rotor radius. First, the analysis was used to obtain the unsteady generalized forces on all the blades, and then a post-processing program was used to solve the eigenvalue problem that provided the aeroelastic characteristics. Figures 1 and 2 show the variation of generalized forces F_{11} with time. Observing the generalized forces, we found that their amplitudes fall off rapidly with increasing distance from the reference blade (the blade being moved). Thus, the argument was

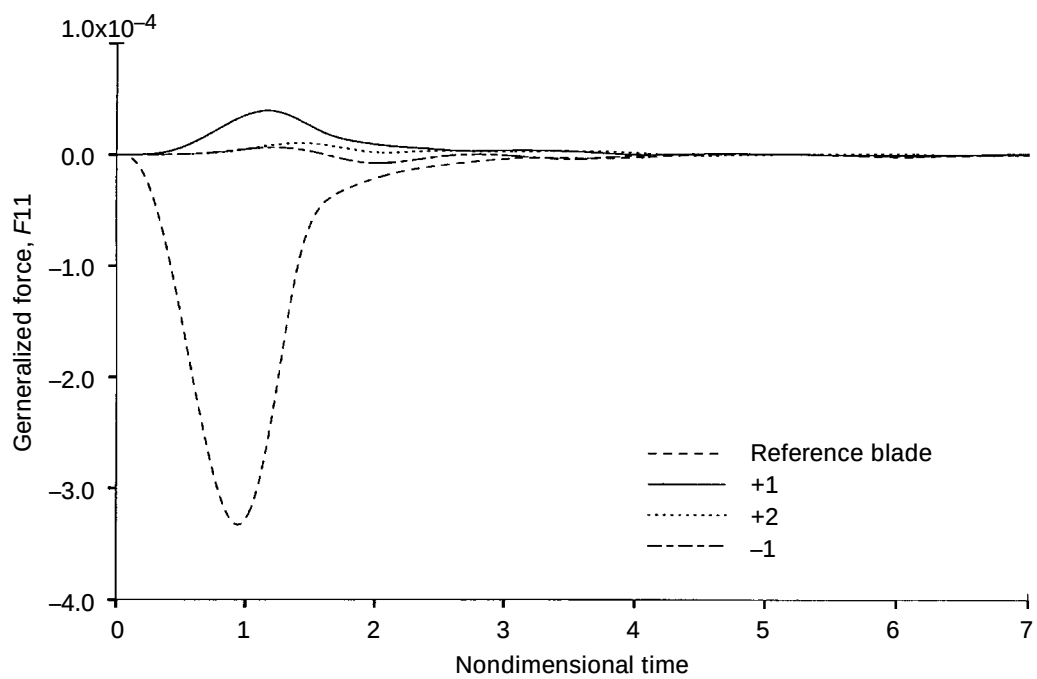

Figure 1.—Time history of generalized forces for the eight-bladed fan operating at $M_\infty = 0.5$, $J = 3.55$, and $\beta = 61.2°$.

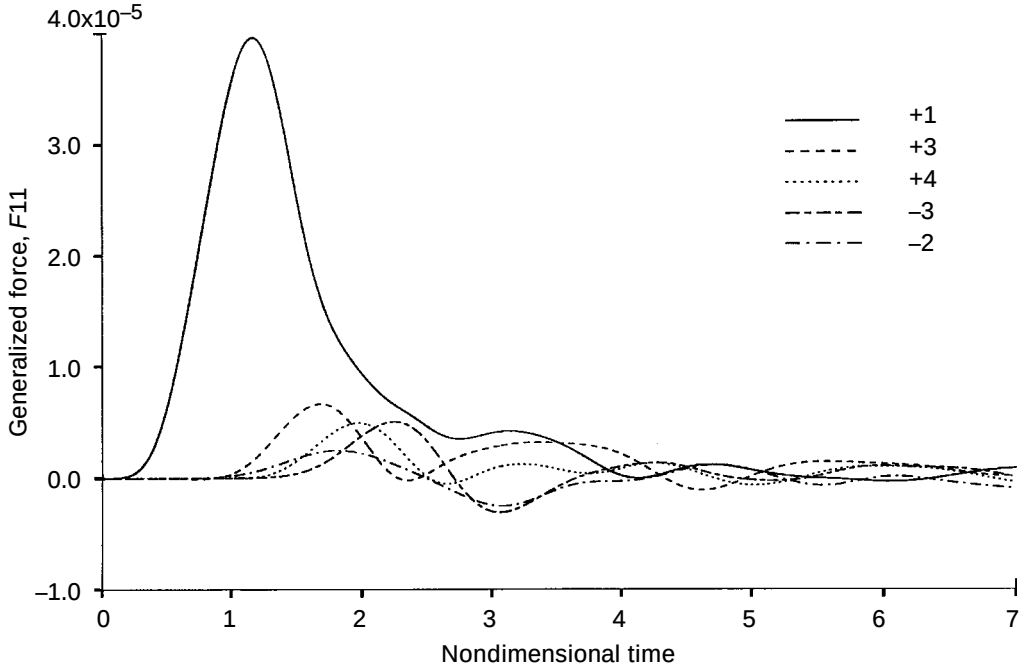

Figure 2.—Plus signs refer to blade location clockwise from reference blade. Minus signs refer to blade location counterclockwise from reference blade, (while standing in front of rotor and looking downstream). (a) Blades closest to reference blade. (b) Blades furthest from reference blade.

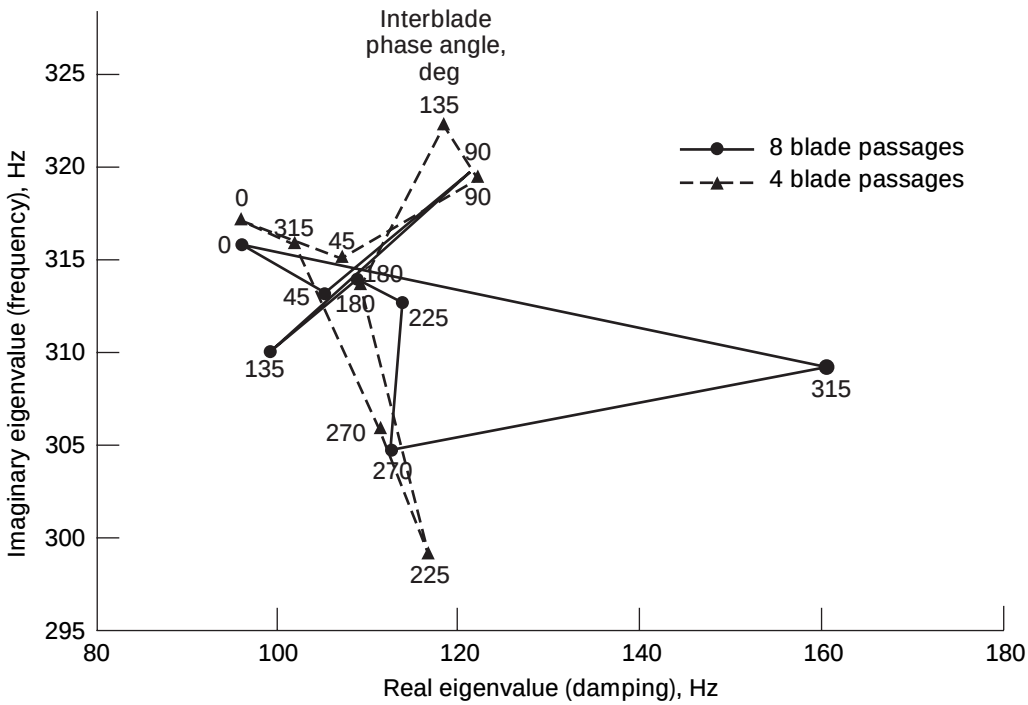

Figure 3.—Eigenvalue plots for analysis of eight- and four-bladed rotors in the eight-bladed fan operating at $M_\infty = 0.5$, $J = 3.55$, and $\beta = 61.2°$.

made that if only the blades in close proximity to the reference blades are included in the analysis, say four blades, the characteristics of an eight-bladed rotor should be able to be calculated within reasonable accuracy. This could potentially reduce the computational costs by at least 50 percent. In order to test this, the generalized forces were calculated for the eight-bladed rotor by using only four blade passages and applying the periodicity across the four blade passages. The resultant eigenvalue plots for both the eight-bladed and four-bladed rotor analyses are shown in figure 3. At this stage the results are not very encouraging. Even though the analysis of the four-bladed rotor accurately predicts the interblade phase angles for which it is valid, the other interblade phase angles are poorly predicted. We feel that this method requires more investigation.

Glenn contacts: Rakesh Srivastava, (216) 433–6045; and Tondapu S.R. Reddy, (216) 433–6083

TURBO-AE: An Aeroelastic Code for Propulsion Applications

NASA's Advanced Subsonic Technology (AST) Program seeks to develop new technologies to increase the fuel efficiency of commercial aircraft engines, improve the safety of engine operation, and reduce emissions and engine noise. With the development of new designs of ducted fans, compressors, and turbines to achieve these goals, a basic aeroelastic requirement is that there should be no flutter or high resonant blade stresses in the operating regime. This, in turn, makes necessary an accurate prediction/analysis code to verify the aeroelastic soundness of the design. Such a three-dimensional viscous propulsion aeroelastic code, named TURBO-AE, is being developed at the NASA Glenn Research Center.

TURBO-AE is based on a three-dimensional unsteady aerodynamic Euler/Navier-Stokes turbomachinery code TURBO, which was developed under a grant from NASA Glenn. TURBO can model viscous flow effects that play an important role in certain aeroelastic problems, such as flutter with flow separation, or stall flutter, and flutter in the presence of shock and boundary-layer interaction. In-vacuum free-vibration modes are used to model the structural dynamics of the blade. Then, a finite-element analysis code, such as NASTRAN, is used to calculate the mode shapes and frequencies.

To determine aeroelastic instability (flutter), a work-per-cycle approach is used. That is, the motion of the blade is prescribed to be a harmonic vibration in a specified in-vacuum normal mode. The aerodynamic forces acting on the vibrating blade and the work done by these forces on the vibrating blade during a cycle of vibration are calculated. If positive work is being done on the blade by the aerodynamic forces, the blade is dynamically unstable, since energy will be extracted from the flow, and an increase in the amplitude of oscillation of the blade will result.

Initial calculations have been done for a configuration representative of the Energy Efficient Engine fan rotor. Figure 1 shows the work-per-cycle after each cycle of vibration, which can be seen to vary only slightly after the fourth cycle of blade vibration. The negative sign of the converged work-per-cycle shows that the fan blade is dynamically stable and will not flutter.

The TURBO-AE code will provide a useful aeroelastic prediction/analysis capability for engine manufacturers. It will reduce design cycle times by allowing new blade designs to be verified for aeroelastic soundness before the blades are built and tested. This prediction capability will make it possible to build thinner, lighter, and faster rotating blades without encountering aeroelastic problems like stall flutter and high-cycle fatigue due to forced vibrations.

Glenn contacts: Milind A. Bakhle, (216) 433–6037; and George Stefko, (216) 433–3920

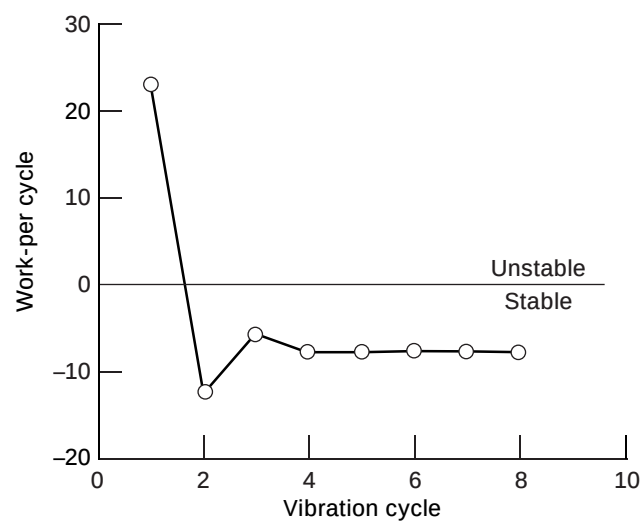

Figure 1.—Aeroelastic work-per-cycle for blade vibrating in first mode.

Using an Integrated Fiber-Optic Light Probe to Measure Static Deflections in Rotating Turbomachinery

An integrated fiber-optic light probe system for monitoring blade-tip deflections, vibrations, and to some extent, changes in blade-tip clearances in a turbomachinery fan or a compressor rotor has been designed, fabricated, and tested. The system is composed of a set of integrated fiber-optic light probes that are positioned to detect the passing blade tip at the leading and the trailing edges. Each probe consists of an integrated fiber-optic transmitting channel and numerical aperture receiving fibers, all mounted in the same cylindrical housing. This configuration permits both nonsynchronous blade vibrations and steady-state blade deflections to be measured by using the timing information provided by each light probe. With integrated fiber-optic technology, a spatial resolution of 50 μm is possible while keeping the outer diameter below 2.5 mm. In addition, one fiber sensor can monitor changes in blade-tip clearance on the order of 10 μm. These probes were evaluated by making measurements in a single-stage compressor facility and an advanced fan rig in the NASA Glenn 9- by 15-Foot Low Speed Wind Tunnel.

Glenn contact: Anatole Kurkov, (216) 433–5695

Feasibility of Using Neural Network Models for Accelerated Testing of Mechanical Systems

Verification testing is an important aspect of the design process for mechanical systems. Full-scale, full-length life testing is typically used to qualify any new component for use in space. However, as the required life specification is increased, full-length life tests become more costly and also lengthen development time. In fact, this type of testing becomes prohibitive if the mission life exceeds 5 years, primarily because of the high cost of and slow turnaround time for new technology. As a result, accelerated testing techniques are needed to reduce the time required for testing mechanical components.

In current accelerated testing methods, typically the speeds, loads, or temperatures are increased in order to simulate a high cycle life in a short period of time. However, two significant drawbacks exist with this technique. The first is that it is often not clear what the accelerated factor is when the operating conditions are modified. Second, if the conditions are significantly changed (on the scale of an order of magnitude or more), the component is forced to operate out of its design regime. When the system is operated under such conditions, the material and mechanical systems' parameters are often exceeded, and the test is rendered meaningless.

We believe that neural network systems may be able to model the operation of a mechanical component. If so, these neural network models could simulate long-term mechanical testing by using data from a short-term test. This combination of computer modeling and short-term mechanical testing could then be used to verify the reliability of mechanical systems, thereby eliminating the costs associated with long-term testing. Neural network models could also enable designers to predict the performance of mechanical systems at the conceptual design stage by entering the critical parameters as input when running the model.

The purpose of this study was to assess the potential of using neural networks for predicting the performance and life of mechanical systems. To do this, we generated a neural network system to model the wear as obtained from three accelerated testing devices: (1) a pin-on-disk tribometer, (2) a line-contact rub-shoe tribometer, and (3) a four-ball tribometer. Critical parameters such as load, speed, oil viscosity, temperature, sliding distance, friction coefficient, wear, and material properties were used to produce models for each tribometer.

The study showed that neural networks were able to model these simple tribological systems, thereby illustrating the feasibility of using neural networks to perform accelerated life testing on more complicated mechanical systems (e. g., bearings, etc.). Figure 1 compares actual wear data generated on a rub-shoe tribometer to data that were generated from a neural network. As the figure illustrates, the correlation is very good.

Neural networks can also be used to predict input variables for conditions that have not been run experimentally. Figure 2 is a neural-network-generated three-dimensional plot of wear rate (pin-on-disk tribometer) as a function of sliding distance and sliding speed. The figure depicts wear rate

values that would occur at different distance and speed values.

Glenn contact: Robert L. Fusaro, (216) 433–6080

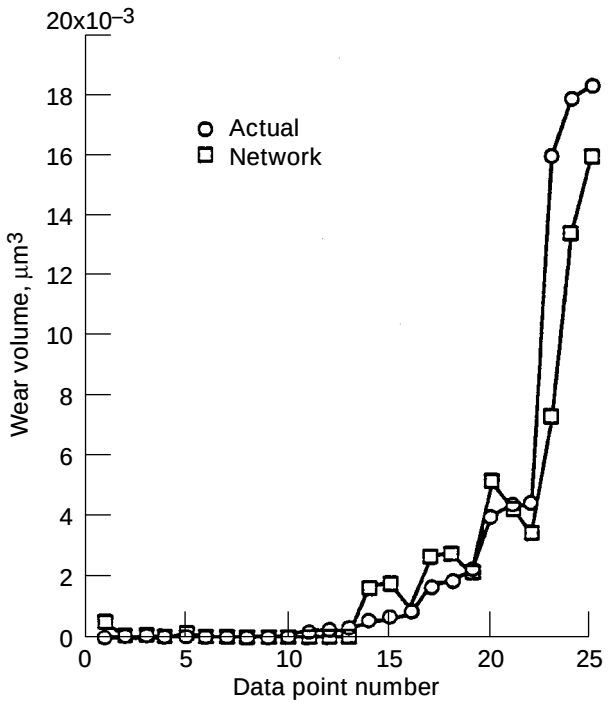

Figure 1.—Comparison of previously unknown rub-shoe wear volumes (actual data) to that of neural network model approximation.

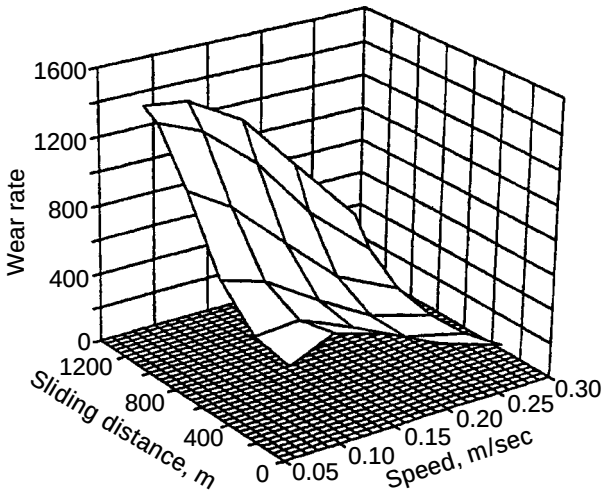

Figure 2.—Neural network-generated three-dimensional plots illustrating the relationship between speed, load, and pin-on-disk wear rate.

Acoustics

Scale-Model Acoustic Liner and Low-Tip-Speed Turbofan Testing

In support of the Advanced Subsonic Technology (AST) project, a cooperative NASA Glenn/Pratt & Whitney test was initiated in October of 1996 to evaluate advanced fan-noise-reduction technologies. The test was conducted in NASA Glenn's 9- by 15-Foot Low-Speed Wind Tunnel (LSWT), which is configured for acoustic testing. The existing Glenn drive rig was used to drive 22-in. fan models for various types of testing. In addition to steady-state aerodynamic data, unsteady aerodynamic data, and structural data, two types of acoustic test data were taken. Far-field acoustic data (fig. 1) and internal duct rotating-rake microphone data were obtained. The rotating-rake data were used to measure acoustic modes present in the duct, especially those due to the interaction of the fan wakes with the stators. The test was divided into two primary segments. The first evaluated the acoustic effectiveness of advanced acoustic liners installed in the inner and outer fan duct. Figure 2 shows the location of these liners in the 22-in. model nacelle duct. Several advanced liners were tested and compared to a baseline that was set (by the AST Project), to 1992 liner technology. During the second test segment, a

Figure 1.—NASA/Pratt & Whitney Fan 1 in acoustic configuration.

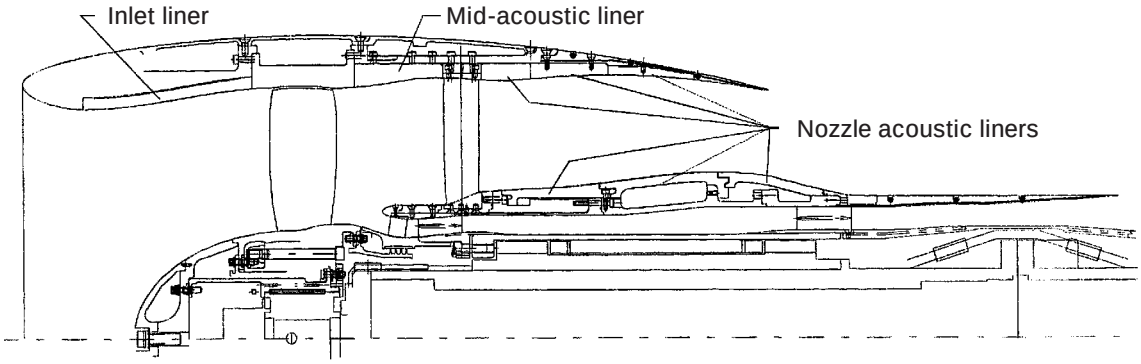

Figure 2.—Location of advanced liners as tested in the 22-in. model nacelle.

highly loaded, low-tip-speed fan (called P&W Fan 2), was tested for aerodynamic performance, operability (which also relates to airplane safety), and acoustic performance.

(1) Concepts validate to improve nacelle duct treatment effectiveness by 25 percent relative to 1992 technology. (Target completion date, January 1, 1997)

(2) Validate technology to reduce engine noise by 6 dB relative to 1992 technology.

Acoustic and aerodynamic performance testing was completed at the end of May 1997 for the advanced liners and also for P&W Fan 2. The data has been shared with the AST community and is being evaluated to determine the noise-reduction effectiveness advanced acoustic liners and the lower tip speed, P&W Fan 2 relative to P&W Fan 1.

Glenn contacts: Brian Fite, (216) 433–3892; and David Elliott, (216) 433–8711

Acoustic Barrier Facilitates Inlet Noise Measurements for Aft-Dominated Fans

Noise from modern high-bypass-ratio subsonic turbofans tends to be aft-dominated. That is, the highest levels of flyover noise radiate from the fan exit. Therefore, to measure the fan inlet sound radiation without contamination from the aft radiation, we had to selectively suppress the aft noise. To do this, we used an acoustic barrier in the NASA Glenn 9- by 15-Foot Low Speed Wind Tunnel (9x15 LSWT), which effectively isolated the inlet noise field on a model of an advanced turbofan. This proof-of-concept test was performed on a model turbofan manufactured for NASA Glenn by the Allison Engine Company as part of the Advanced Subsonic Technology (AST) Program. The barrier was of wood frame construction, 8 cm thick with, typically, 0.64-cm tempered fiberboard skins. It was constructed in sections that were joined upon installation, and it was mounted on tracks on the tunnel floor and ceiling at a sideline distance of 15 cm from the fan nacelle. The barrier sections extended from floor to ceiling and had an axial length of 61 cm. An elliptical leading edge was faired into the upstream barrier section, where nominally full-height by 46-cm-axial-length acoustic treatment was installed on the fan side of the barrier just downstream of the leading edge. This acoustic treatment consisted of a bulk absorber with a perforated metal skin. Tests were made with the barrier leading edge at the fan inlet highlight plane and at a distance 15 cm further aft. The barrier extended downstream virtually to the end of the treated tunnel test section.

Figure 1, a photograph of the Allison fan in the 9x15 LSWT, shows the acoustic barrier in the upstream position. The translating microphone, which was used to collect the acoustic data, is on the 224-cm sideline. Figure 2 is a directivity plot showing the aft fan noise suppression due to the barrier along the 224-cm sideline. These data are for one-third octave band levels at 6300 Hz, which corresponds to the second harmonic of the fan rotor-stator interaction tone. Results are shown for the fan without the barrier and for the fan with the barrier leading edge at the two different axial test locations. Aerodynamic data indicate that the barrier does not influence the performance of the fan.

Glenn contacts: Richard P. Woodward, (216) 433–3923; and Christopher E. Hughes, (216) 433–3924

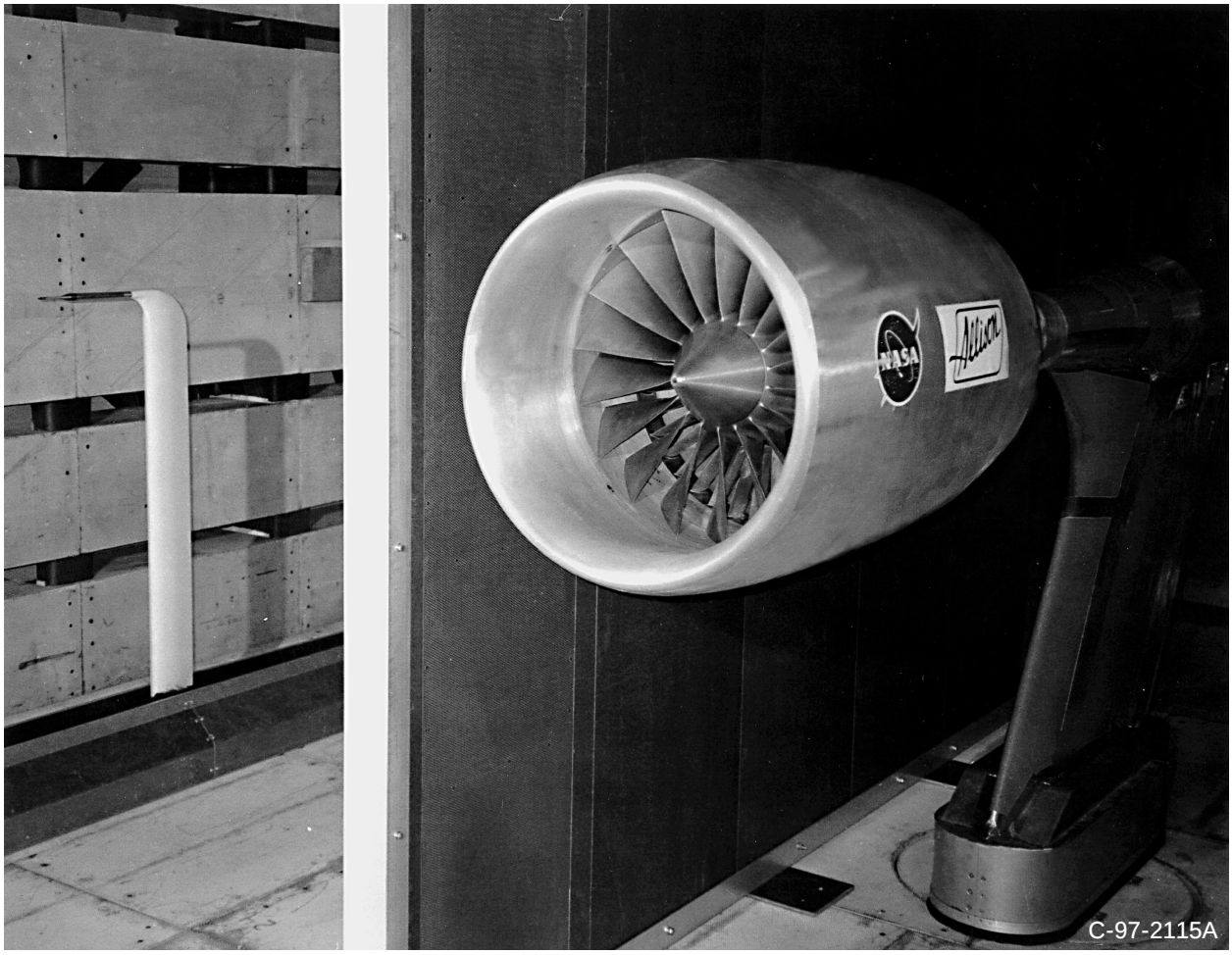

Figure 1.—Allison fan installed in Lewis' 9x15 LSWT with acoustic barrier in place. Translating microphone probe used to acquire sideline noise data is visible on the sideline.

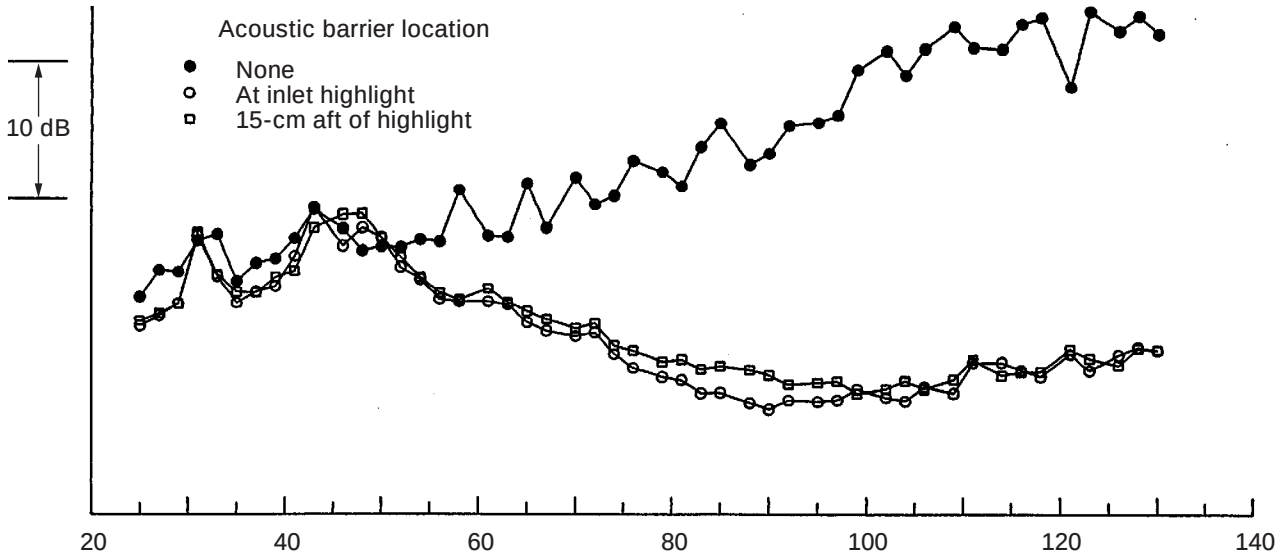

Figure 2.—Sound pressure level directivities for fan 2 blade passage frequency tone showing acoustic shielding effect of the barrier wall.

Jet Noise Prediction for Internal Exhaust Mixer Nozzles

At NASA Glenn, advanced exhaust systems designed to reduce jet noise from low-bypass-ratio turbofan engines are being studied as part of NASA's Advanced Subsonic Technology Program. Our efforts are directed at developing engine components that will reduce acoustic emissions and not compromise engine performance. Thus, experiments were conducted to map aeroacoustic features of internal exhaust gas mixers. Test configurations included 12- and 20-lobe mixers, as well as a reference splitter nozzle at one-seventh scale. At the same time, computational tools were developed to help designers with the parametric study and development of new generation mixers. Aeroacoustic measurements of these nozzles will serve as a data base for developing improvements to existing aerodynamic and acoustic prediction capabilities.

A computational-based acoustic code that predicts turbulence-generated noise on the basis of a Reynolds-averaged Navier-Stokes solution was developed. Flow predictions were made with the NPARC code and an appropriate two-equation k-ε turbulence model.

In acoustic calculations, we assumed noise is dominated by small-scale turbulence, and that noise sources are those described by Lilley's equation, namely self and shear noise; these were modeled to account for anisotropy of turbulence. Figure 1 shows a 12-lobe mixer operating at a primary nozzle pressure ratio of 2.77. Sample acoustic predictions only for noise sources external to the mixer exit plane are shown in figures 2 and 3. Figure 2 portrays far-field sound pressure level directivity on an arc of 15.25 m, and figure 3 shows the noise spectra at $\theta = 150°$ from the nozzle inlet.

Glenn contact: Abbas Khavaran, (216) 977–1120

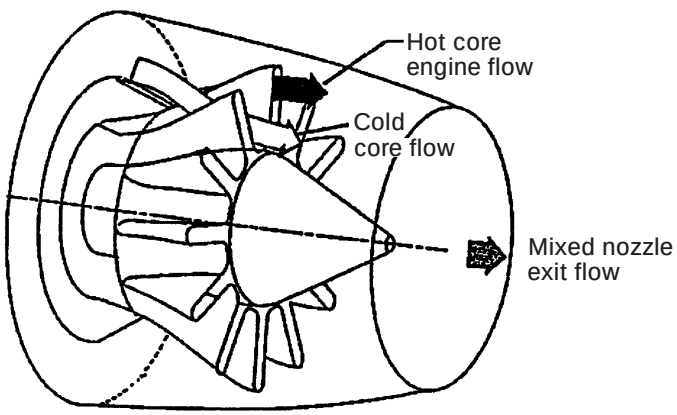

Figure 1.—Geometry of typical lobed forced mixer exhaust.

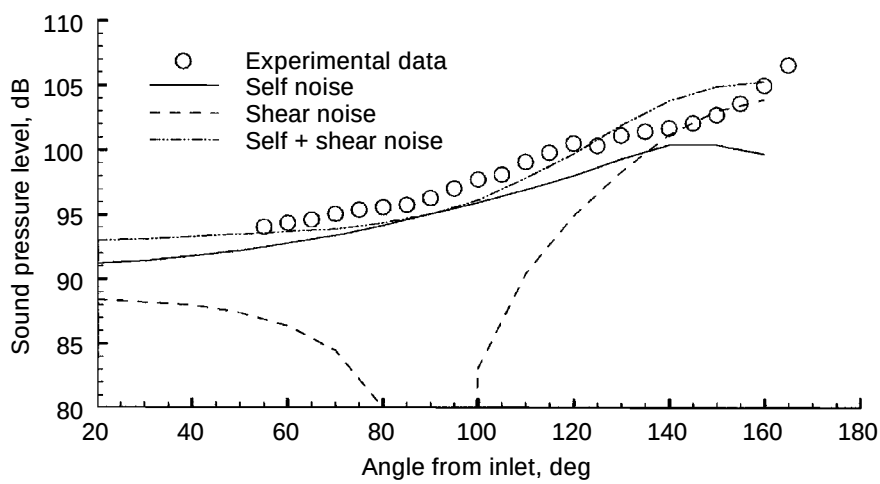

Figure 2.—Sound pressure level (SPL) directivity.

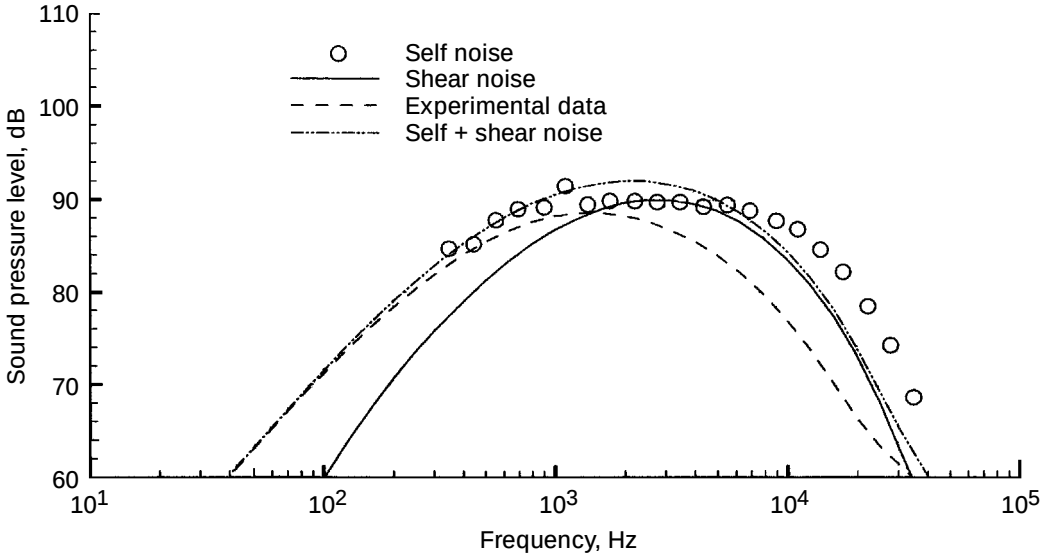

Figure 3.—Spectra at $\theta = 130°$ from nozzle inlet.

Mechanical Components

Gear Crack Propagation Studies

Designers of gears for helicopter or turboprop power transmissions have a common goal: reduced weight. To help meet this goal, some design gears with thin rims. Rims that are too thin, however, may lead to bending fatigue problems and cracks. The most common methods of gear design and analysis are based on standards published by the American Gear Manufacturers Association. Among these standards are rating formulas for gear tooth bending to prevent crack initiation. These standards take into account the effect of rim thickness on tooth bending fatigue; however, they do not indicate the crack propagation path or the remaining gear life once a crack has started.

Recently, analytical and experimental studies were performed to investigate the effect of rim thickness on gear tooth crack propagation. The goal was to determine, for various rim thicknesses, whether cracks grow through gear teeth or through gear rims. A finite-element-based computer program FRANC (Fracture Analysis Code) simulated gear tooth crack propagation by using principles of linear elastic fracture mechanics. Quarter-point, triangular elements were used to represent the stress singularity at the crack tip. The program had an automated crack propagation option that used an automated remeshing scheme to numerically simulate crack growth. To determine crack propagation direction, crack tip stress intensity factors were estimated. Crack propagation life was predicted on the basis of the calculated stress intensity factors by using various fatigue crack growth models. In addition, gear bending fatigue tests were performed in a spur gear fatigue rig. Gears with various backup ratios (rim thickness divided by tooth height) were tested to validate crack path predictions and crack propagation life.

For backup ratios of 3.3 and 1.0, the analysis predicted that cracks would propagate through the teeth and not the rims. This was validated by the experiments (fig. 1(a)). For a backup ratio of 0.3, the analysis predicted cracks that would propagate through the rim, which was also validated by experiments (fig. 1(b)). For a backup ratio of 0.5, the experiments produced rim fractures whereas the analysis showed instability (tooth or rim fracture), depending on various initial conditions. The analytical results at the point of transition from tooth to rim failure should be used cautiously to produce a safe gear design. A good correlation between predicted and measured gear crack growth was achieved when the predictions were based on the Paris crack growth equation and the concept of fatigue crack closure. For thin rims, a decrease in rim thickness caused an increase in both the stress intensity factor and the compressive cyclic stress in the gear tooth fillet region. The increase in stress intensity factor promoted crack growth, whereas the increase in cyclic compressive stress tended to

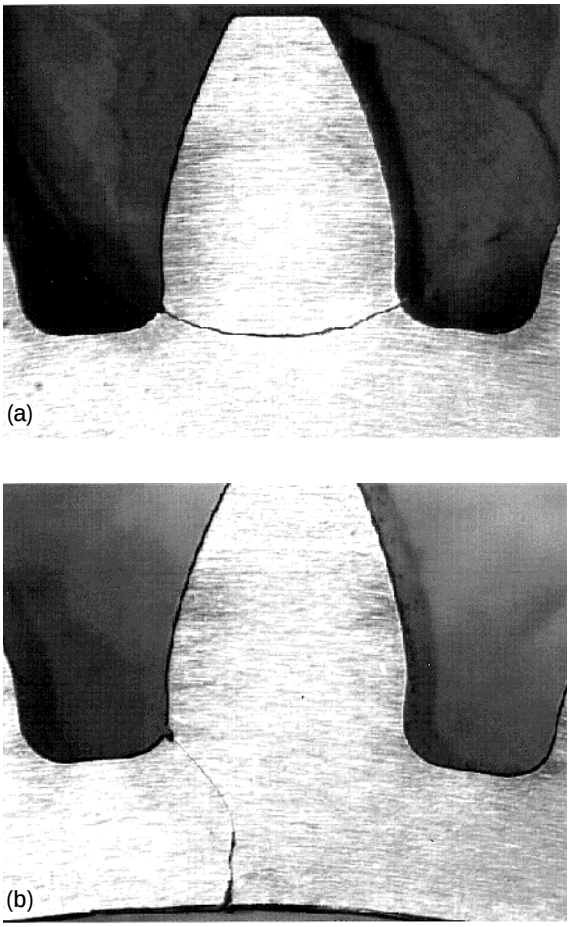

Figure 1.—Experimentally determined crack propagation paths. (a) Thick-rimmed tooth produced tooth fracture. (b) Thin-rimmed tooth produced rim fracture.

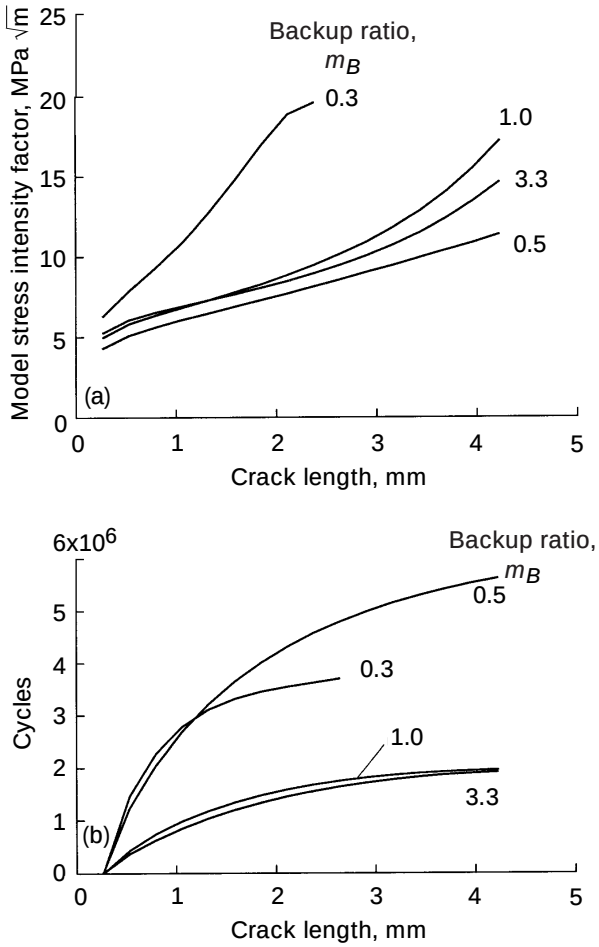

Figure 2.—Effect of backup ratio on crack propagation. (a) Mode-I stress intensity factors. (b) Crack propagation cycles.

retard crack growth and increase the number of propagation cycles to failure (see fig. 2). For more information, see Lewicki and Ballarini (1996a and b) and Zakrajsek and Lewicki (1996).

Glenn contact: David G. Lewicki, (216) 433–3970

Validated Method to Optimize Load Sharing of Split-Torque Transmissions

Most helicopters in service have a planetary transmission design. Studies show that some helicopters would be lighter and more reliable if a split-torque transmission design were employed. Historically, U.S. helicopter manufacturers have been hesitant to use this design because of difficulties in ensuring balanced load sharing among the load paths—an essential design consideration. Recently, a Sikorsky-Boeing team chose to use this design in the U.S. Army Comanche helicopter, with Sikorsky Aircraft designing and manufacturing the transmission. To ensure that such a helicopter would be safe, NASA and Army researchers studied the load-sharing problem. A theory was proposed that balanced load sharing could be achieved by proper configuration of the geartrain. From this theory, scientists at the NASA Glenn Research Center developed a computer code to determine the optimal configuration. The code calculates how elastic deformations in the gear teeth, shaft, housing, and bearings affect the relative load carried in each load path. Sikorsky Aircraft applied the information from the new computer code to the design of the Comanche gearbox.

A prototype split-torque transmission had been designed and built prior to the development of the theory and code. Measurements on the prototype's four final drive gears showed an unbalanced load distribution, with one gear beyond its allowable design limit. The Sikorsky theory and the NASA Glenn code duplicated the load trends, and inhouse experiments showed similar results. The code was then applied to the prototype transmission to determine its optimum design configuration. Incremental design changes were made to the transmission, and subsequent testing showed nearly equal load sharing on the four final drive gears—with all of them below the design limit (see fig. 1). Because of this analysis, a significant amount of development time and money was saved.

Government and Sikorsky personnel have applied for a patent as coinventors of the validated theory and computer code. Glenn and the Army continue to collaborate with Sikorsky Aircraft by sharing transmission technology that will bring the Comanche gearbox design to maturity. For more information, see Krantz (1996) and Krantz and Delgado (1996).

Glenn contact: Timothy L. Krantz, (216) 433–3580

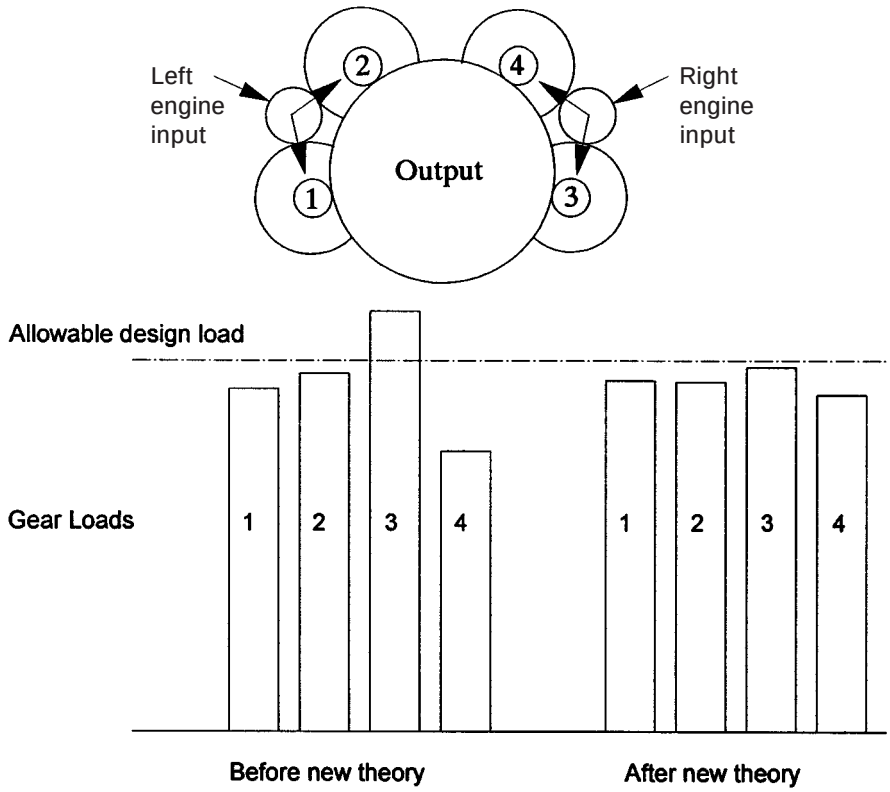

Figure 1.—Measurements of loads on four final drive gears prove that new theory ensures load sharing.

Evaluation of Face Gears for Aerospace Drive System Applications

Reduction of system weight is the highest priority for any helicopter drive system. With this in mind, face gears have been chosen as a candidate gear mesh component for advanced helicopter drive train systems. This gear system can transfer power from a single input pinion to two output gears, thereby reducing by 50 percent the level of loading applied to the teeth. In a helicopter drive system this capability results in a substantial weight savings as the gears can be designed to have approximately half the load capacity of standard spiral bevel gears. Figure 1 shows face gears in a future helicopter drive system.

In the past, face gears were limited to low-load and low-speed arrangements. In helicopters they would be operating well beyond their known operational envelope. Furthermore, there are no design criteria for face gears. And their manufacture presents another problem: Aerospace gears are produced to very tight tolerances, with the best gear steels being used for strength and durability, and Computer Numerically Controlled (CNC) machines often being, used to manufacture them; however, the manufacturing process for face gears is not this modern. Thus, the Defense Advanced Research Projects Association (DARPA) is currently funding development of a procedure to final-grind the face gear members.

Since 1991, NASA Glenn has been experimentally evaluating the face gear system (see the test hardware in fig. 2). During this time period, several variations in the tooth geometry and heat treatment have enabled the gears to operate at high rotational speeds and loads (19 100 rpm, 360 hp). The long life required for these gears, however, has still not been realized. The hardware tested to date has been compromised by less than adequate materials and dated manufacturing technology. As a result, current aerospace gear materials and modern final

grinding processes are being used to manufacture new face gears, which are expected to be tested by October 1997. For more information, see Handschuh et al. (1997).

Glenn contacts: Robert F. Handschuh, (216) 433–3969; and David G. Lewicki, (216) 433–3970

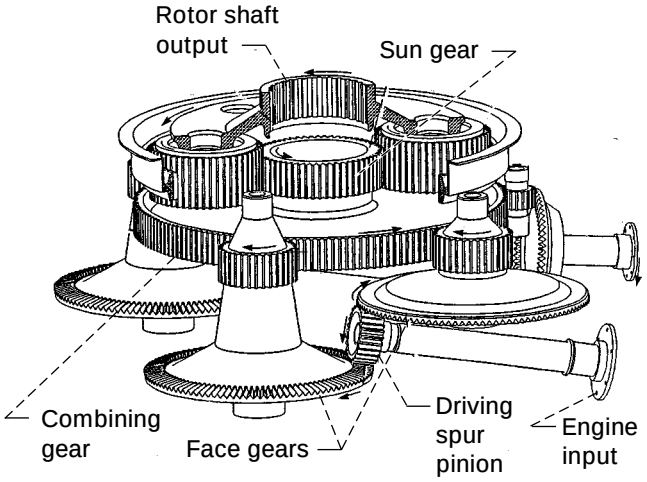

Figure 1.—Helicopter transmission with face gear drives.

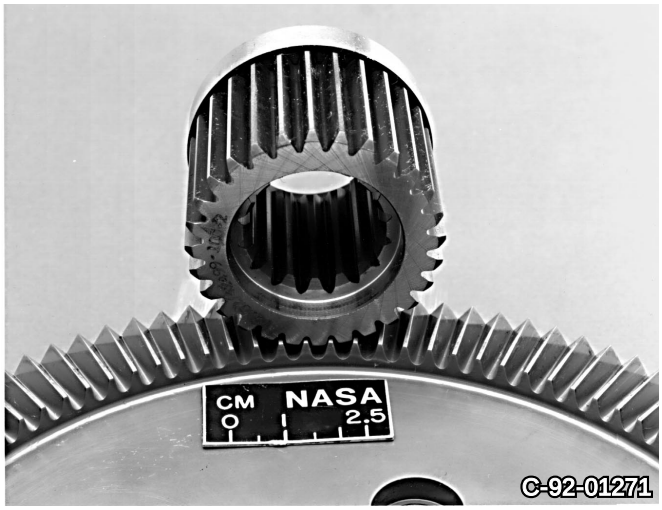

Figure 2.—Face gear specimen used in test program.

Using Hob Offset to Balance Strength of Spur Gears

In a gear set with a speed ratio other than unity, the smaller gear (the pinion) tends to be weaker than the larger gear, particularly if the pinion has a small number of teeth. Also, in some cases, tooth interference from the pinion may cause undercut. Undercutting further reduces tooth strength.

Gear designers sometimes specify nonstandard gears, such as one with the tooth addendum on the pinion increased slightly and the gear addendum reduced. This adjustment to the tooth addendum is made by withdrawing the hob (cutting tool) slightly as the pinion is cut and by advancing the hob as the gear is cut.

For nonstandard gears operated at standard center distance, the cutter offsets for the pinion and gear are equal and opposite. In some designs, especially those with large module teeth, long addendum pinion teeth may cause undercutting on the gear. In these cases, the gears can be operated at a slightly extended center distance.

The NASA gear dynamics code Dynamic Analysis of Spur Gear Transmission (DANST) was used to investigate the effect of various amounts of hob offset on the dynamic stress to a set of extended center distance spur gears operated over a wide speed range. Results were compared with the optimum value computed from an older static procedure. A contour diagram (fig. 1) shows how various hob offset values over the speed range of 1 000 to 15 000 rpm affect the dynamic tooth stress. At lower speeds (below 5 000 rpm) the dynamic stress is minimized by hob offsets that are less than the optimum static value, which is shown as a dashed line. (See the two areas marked with letter “A” in fig. 1). Above 7 000 rpm, the dynamic stress is minimized by a greater amount of hob offset (letter “B” in fig. 1).

Often the goal in gear design is to create a balance between the tooth strength of the pinion and the gear. Maximizing pinion tooth strength may excessively weaken the teeth of the gear. Another study was done to find the amount of hob offset required for balanced tooth strength. Figure 2 shows these results. The gear dynamics code DANST can be used to determine an optimally balanced design. For more information, see Lin et al. (1997) and Liou et al. (1995).

Glenn contact: Fred B. Oswald, (216) 433–3957

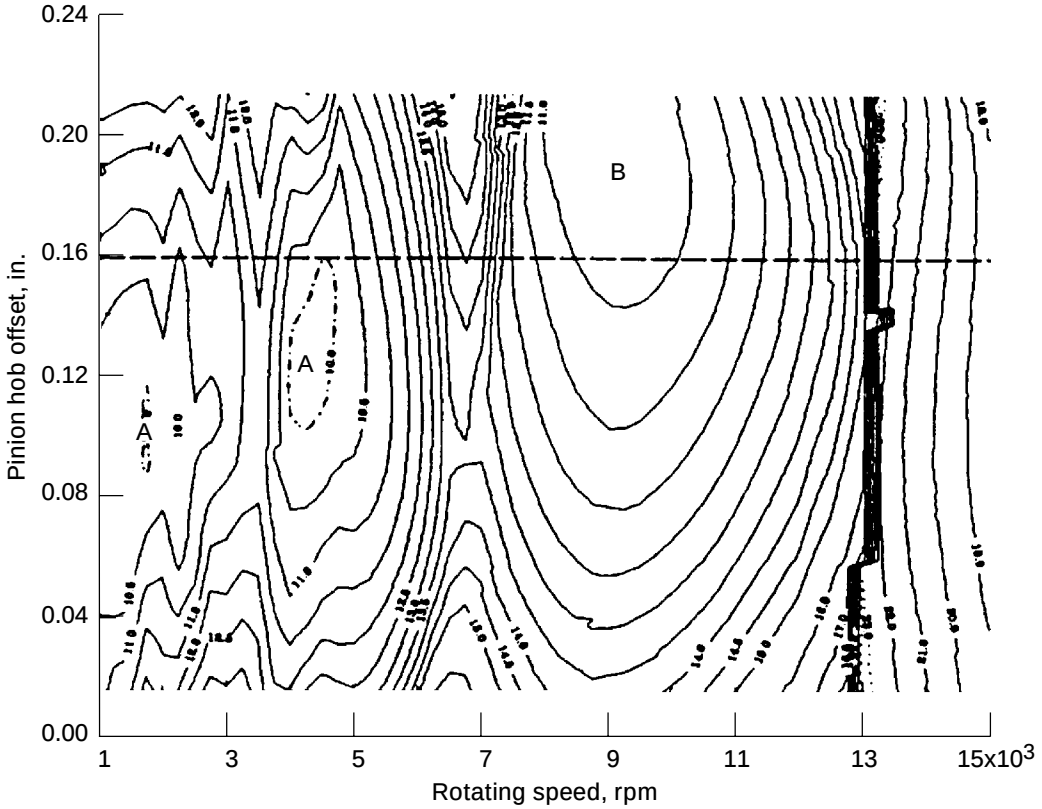

Figure 1.—Contour plot showing effect of hob offset and operating speed on pinion dynamic stress. (Dashed line indicates optimal static procedure hob offset.)

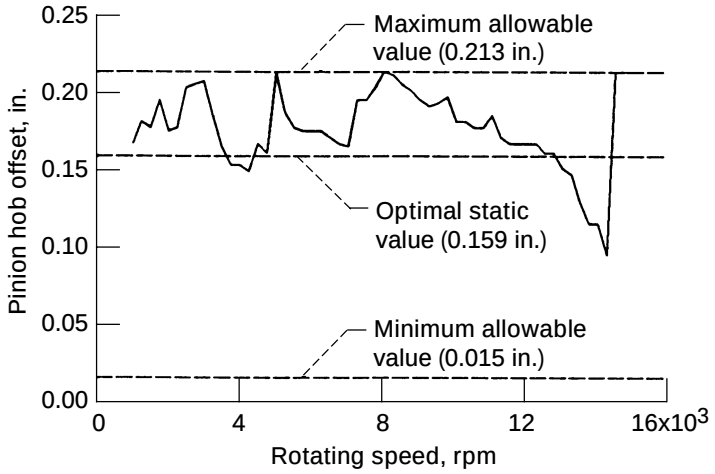

Figure 2.—Hob offset value required to balance dynamic tooth strength of pinion and gear plotted as a function of operating speed.

Brush Seals Tested for Joint Technology Advanced Gas Generator II Engine

Brush seals for the Joint Technology Advanced Gas Generator (JTAGG) II engine being developed by AlliedSignal Engines were tested at the NASA Glenn Research Center. This engine uses two identical brush seals in tandem to separate the hot high-pressure compressor air from the cooler buffer air for the number 2 carbon ring seal. At intermediate rated power, the engine operating conditions for the brush seal are estimated to be 50 000 rpm (899 ft/sec), 175-psid air-to-air-pressure differential, and 1200 °F inlet air temperature. Both static and performance tests were done on the brush seals. In addition, they were tested with a radial offset of 0.003 in. to simulate maneuver conditions and with a radial runout of 0.003 in. in the rotor to simulate transient conditions such as traversing through critical speeds. A 50-hr endurance test was also conducted. Although the maximum operating conditions could not be attained simultaneously in the seal test rig, we concluded that the brush seal design should be able to meet the air-leakage flow factor goal of less than 0.004 at maximum operating conditions.

In post-test inspection, small amounts of wear were found in the Haynes 214 bristle tips and the Inconel 718 rotor that was coated with Triboglide (EG&G

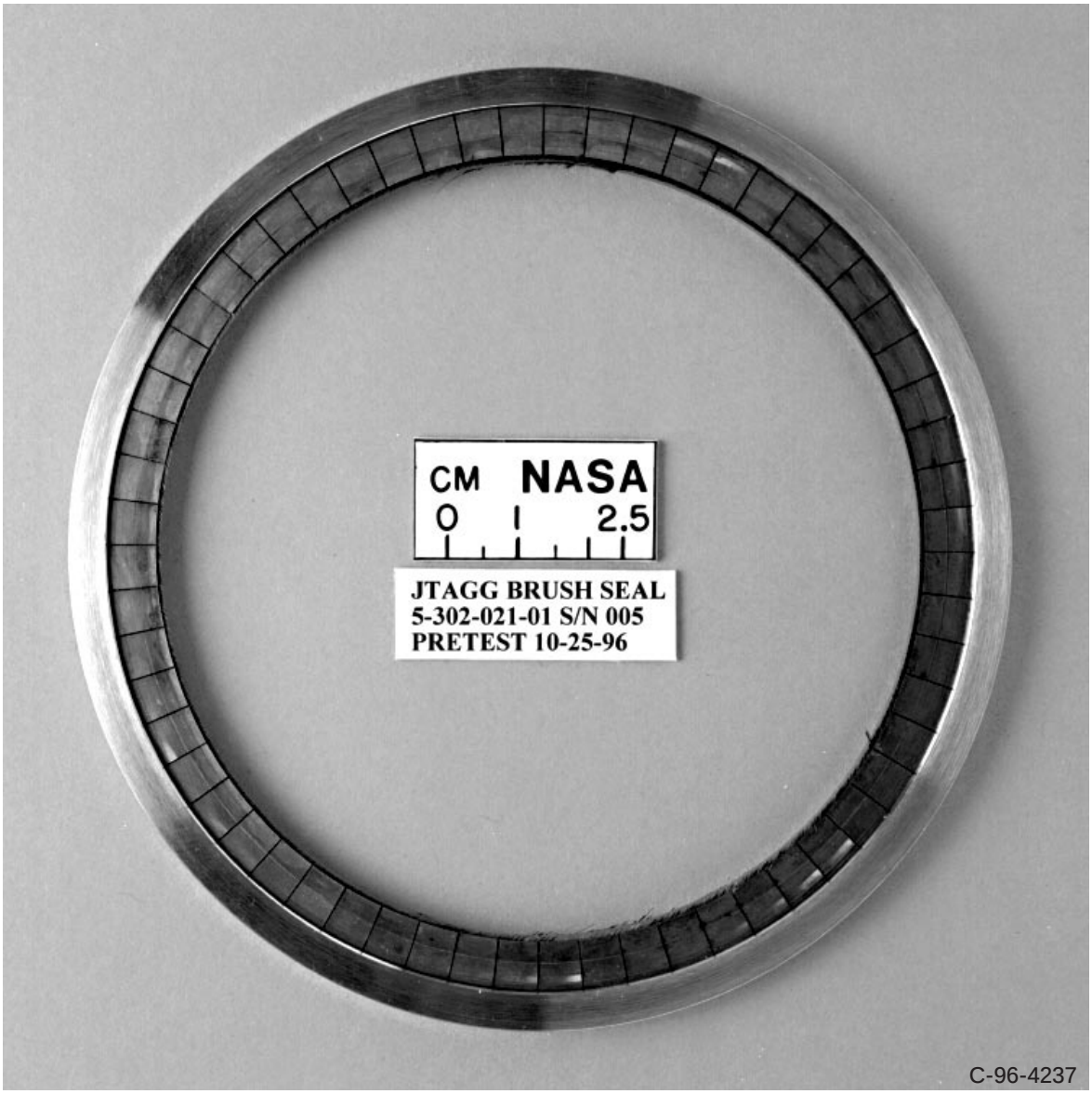

Figure 1.—Advanced low-hysteresis brush seal.

Sealol, Cranston, RI). Triboglide is a chromium carbide coating with barium calcium fluoride (a high-temperature solid lubricant) dispersed in the coating. Overall, the seal and rotor were in excellent condition; thus, we predict that the seals should easily meet the JTAGG II engine test requirement of 100 hr.

We tested both conventional and advanced low hysteresis design brush seals. An advanced low hysteresis design brush seal is shown in figure 1. The bristles are made of Haynes 214, and the side plates are made of INCO 625 (Inconel). The low-pressure side plate was relieved where it contacts the bristles, and a thin deflector plate was inserted between the high-pressure side plate and the bristles. Initially, this seal exhibited little hysteresis, but after 50 hr of testing, substantial hysteresis occurred. However, the leakage flow factor remained under the 0.004 goal. For more information, see Arora and Proctor (1997).

Glenn contact: Margaret P. Proctor, (216) 977–7526

Diagnostic Parameters Detect Gear-Tooth Fatigue Crack

Drive-train diagnostics is one of the most significant areas of research in rotorcraft propulsion. An investigation of serious rotorcraft accidents resulting from fatigue failures showed that 32 percent of the failures occurred in engine and transmission components. Now, Government aviation authorities are demanding that in the near future the safety record of civil helicopters match that of conventional fixed-wing jet aircraft. Such an accomplishment would require that helicopter safety improve 30-fold over fixed-wing aircraft. Practically, this can be accomplished only with the aid of a highly reliable, online health and usage monitoring (HUM) system. For rotorcraft transmissions, a critical element of a reliable HUM system is the ability to accurately detect gear-tooth damage as early as possible. A gear-tooth fatigue crack, if undetected, can propagate into complete tooth fracture or gear rim fracture, both of which can result in catastrophic failure of the transmission system. To assess the performance of a variety of gear damage detection techniques, gear crack propagation tests were conducted at the NASA Glenn Research Center.

The spur gears shown in figure 1 were part of a series of crack propagation tests conducted on a spur gear fatigue test rig at NASA Glenn. To initiate cracks, a notch was placed in the fillet region (loaded side) on one tooth of each of the test gears. The notches were located at a radius of 40.49 mm on the fillet, which is the position of maximum tensile stress. The spur gear test rig was then used to cause the spur gear specimen to fail through bending fatigue. To verify the crack growth rate, crack detection gauges were installed on each side of the notched tooth. As the crack propagated, it broke through each of the nine crack wires that circumferentially surrounded the fillet area on each side. In figure 2 crack length is plotted as a function

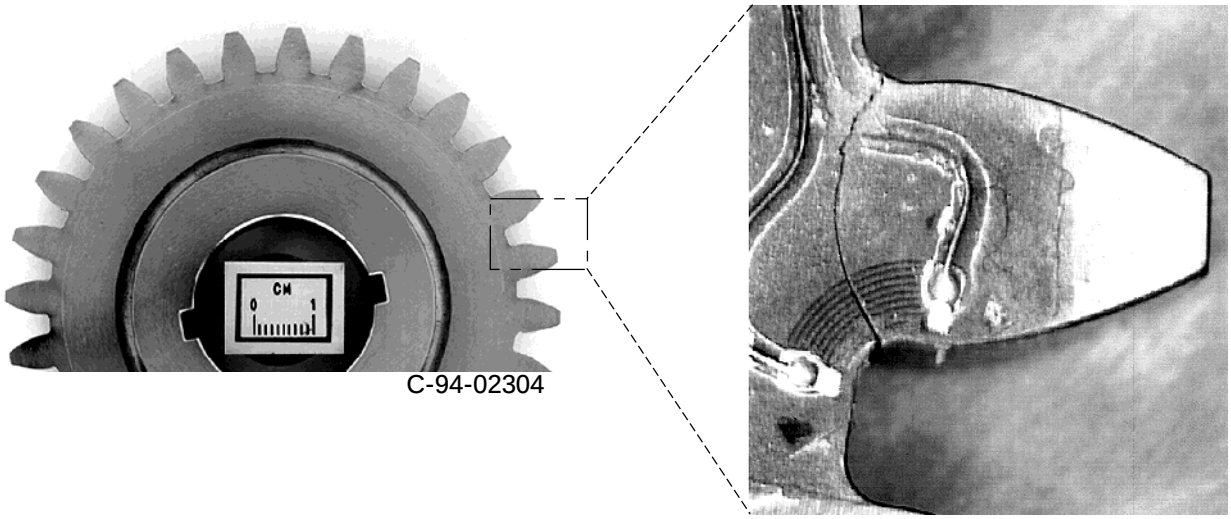

Figure 1.—Test gear used in fatigue crack propagation studies.

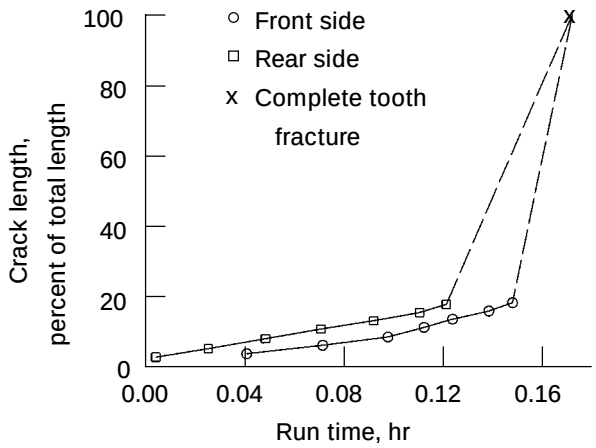

Figure 2.—Crack length as a function of run time.

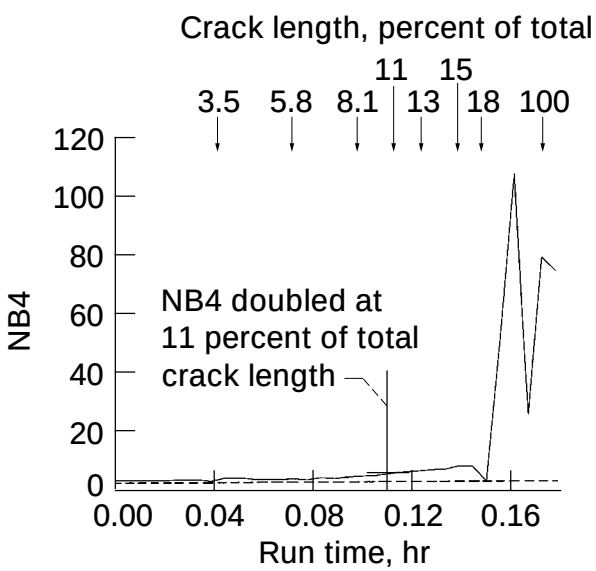

Figure 3.—Parameter NB4 as a function of run time.

of run time for the test gear shown in figure 1. As can be seen in figure 2, the crack gauges covered only the first 18 percent of the total crack length before failure occurred (complete fracture of the tooth). Although the crack gauges covered only 18 percent of the total crack length, they covered 75 percent of the time from the start of the crack to gear or tooth failure. Two regions can be seen in figure 2: in the first there is moderate crack growth rate (first 75 percent of propagation time); and in the second, accelerated crack growth rate, where the final 82 percent of total crack length occurs (last 25 percent of crack propagation time).

A number of gear damage detection techniques were applied to the vibration signal emitted by an accelerometer mounted on the housing of the gear test rig. All of the gear fault detection methods investigated reacted to the fatigue crack in the region of accelerated crack growth, prior to complete fracture. Recall that this is the region where the last 82 percent of total crack length is achieved in only 25 percent of the total crack growth time. Although in this test all of the methods were able to detect the crack during propagation in this last region, more advance warning of the potentially catastrophic crack is needed. Only three of the methods investigated were able to show a trend that was increasing beyond the nominal value during the first phase of crack propagation. Of these three, the technique called NB4, which was developed at NASA Glenn, gave the most robust indication of the fatigue crack. NB4 is a demodulation technique that uses normalized kurtosis to produce a dimensionless fault-indication parameter with a value of three under nominal conditions. Figure 3 shows the NB4 parameter (measure of gear faults) detection as a function of run time for this test. For reference, the crack length as a percent of total length is shown along the top of this figure. The NB4 parameter not only gave a robust indication of the crack in the accelerated crack growth region, prior to failure, but also, more importantly, it reacted to the growing fatigue crack during the moderate crack growth region. When the crack had advanced to only 11 percent of its total length to failure, NB4 indicated a value double the nominal value. This is significant in that the earlier a fatigue crack can be detected in an aircraft transmission, the more time and options that are available to the operator. For more information, see Zakrajsek and Lewicki (1996).

Glenn contact: James J. Zakrajsek, (216) 433–3968

Gas Journal Bearing Stability Versus Amplitude Ratio

A gas journal bearing with a wavy surface was tested over a range of speeds up to 18 000 rpm to determine its stability in an unloaded condition as a function of the wave amplitude. The bearing was 50 mm in diameter, 58 mm long, and had 0.0165 mm of radial clearance. Three waves were created on the inner surface by deforming the bearing sleeve. The ratio of the wave amplitude to the radial clearance (i.e., wave amplitude ratio WAR) was varied from 0 to 0.3.

Unlike the plain journal bearing (fig. 1(a)), a wave journal bearing reduces the susceptibility to subsyncronous frequency whirl (SSFW) motion. A wave journal bearing (Dimofte, 1995) is a bearing with a slight, but precise, variation in the circular profile of the bearing such that a waved profile is circumscribed on the inner bearing diameter. The profile has a wave amplitude that is a fraction of the bearing clearance. Figure 1(b) shows a three-wave bearing. Note that the clearance, the wave, and the wave's amplitude are greatly exaggerated in figure 1 so that the concept may be visualized.

Experiments showed that for wave amplitude ratios of 0.187 or larger the bearing ran in a stable mode, up to a critical speed, after which it began to experience SSFW motion with a frequency close to one half the synchronous frequency. The speed threshold when the SSFW motion began was found to be a function of the WAR. For example, the threshold speed was 9 650 rpm for a WAR of 0.187 and 17 210 rpm for a WAR of 0.30. However, for WAR's smaller than 0.187 (such as 0.024 and 0.157), the bearing became sensitive to SSFW motion at very low speeds. Moreover, it developed a supersynchronous whirling motion with a frequency close to twice the synchronous frequency. A WAR equal to 0.187 or greater suppressed both the subsynchronous and supersynchronous whirl motion and allowed the bearing to run in a very stable mode.

A stability bearing analysis code was used to predict the critical mass of an experimental bearing operating in an unloaded condition. WAR's from zero (true circular) to 0.35 were used. The results are plotted in figure 2, where we can see that a true circular bearing and a wave bearing with a WAR of 0.15 are unstable for any bearing mass. However, if the WAR is increased, a portion of the predicted curves lie above the bearing mass line. In these regions the bearing can run in a stable mode free of SSFW motion.

The experimentally observed threshold to SSFW motion for a bearing with a WAR equal to 0.187 or larger is also plotted in figure 2 as a set of scattered points located on the horizontal line denoting the actual bearing mass value of 5.2 kg. Essentially, this line intersects with the predicted critical mass curves at the speeds at which a bearing with a mass of 5.2 kg would begin SSFW motion for the given WAR values. Figure 2 demonstrates that the experimental data points are in good agreement with the predicted values. For more information, see Dimofte (1995).

Glenn contact: Florin Dimofte, (216) 977-7468

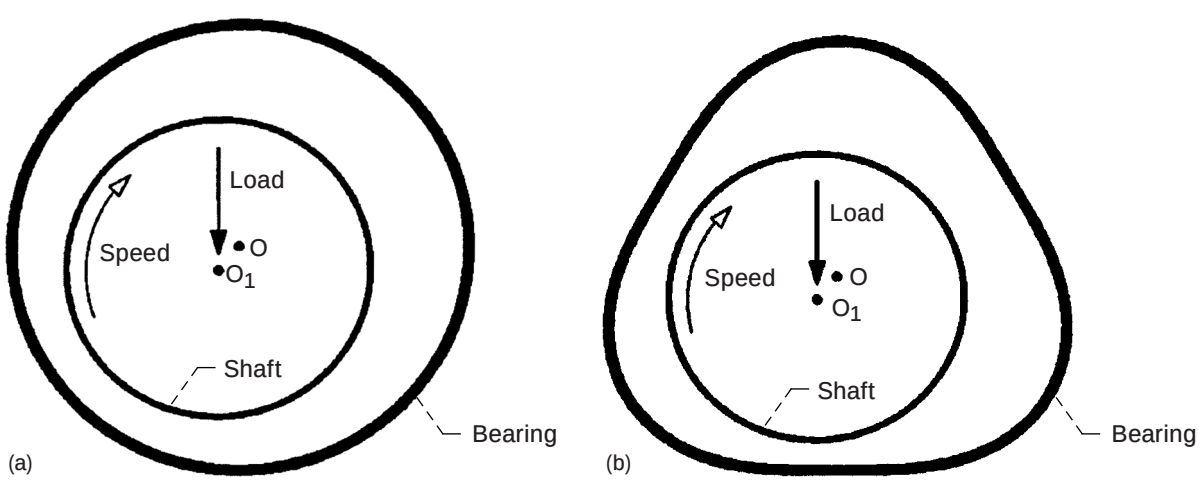

Figure 1.—Journal bearings. (a) True circular. (b) Three wave. (Shaft center, 0; bearing center, 0_1.)

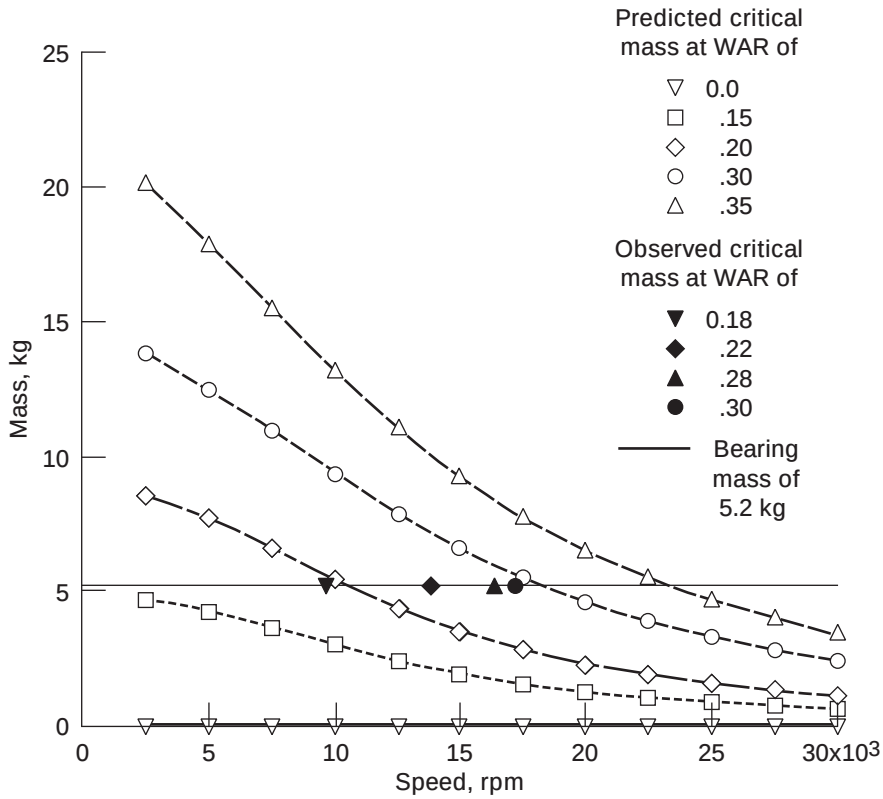

Figure 2.—Predicted critical mass and experimentally observed threshold of whirling.

NASA Selects 1996 Government Invention of the Year

A patented seal developed for the National Aerospace Plane project by Dr. Bruce M. Steinetz and Mr. Paul J. Sirocky (retired) of NASA's Glenn Research Center, Cleveland, Ohio, won NASA's 1996 Government Invention of the Year award.

The High-Temperature, Flexible, Fiber Preform Seal has been used for numerous NASA aeronautic applications since it was patented in 1992. It was also used by General Electric Aircraft in the joint NASA/DOD/GE Integrated High Performance Turbine Engine Technology Program (IHPTET). The hybrid rope seal was used to seal the perimeter of advanced nickel-aluminide turbine vane airfoils; thus the vane could grow relative to the supporting structure, thereby overcoming the thermal shock failure experienced with conventional seals. The high-temperature turbine vane/seals, combined with several other advanced technologies, contributed to meeting the program goals of reducing specific fuel consumption by 20 percent and increasing engine power-to-weight by 40 percent, in a successful full-scale Joint Technology Advanced Gas Generator (JTAGG) engine test.

The invention is being evaluated by Pratt & Whitney as a possible replacement for the sealing interfaces between the large turning vanes and the flowpath fairing elements of the F119 engine, which will be used in the F22 fighter, the country's next generation premier fighter plane. Because of the potential for improved durability, Pratt & Whitney is also evaluating an abrasion-resistant hybrid version of the seal (ceramic core/superalloy sheath). And Williams International is evaluating NASA's fiber preform seal as a means to both seal and structurally support a high-temperature, uncooled, engine transition segment for an advanced

demonstrator turbine engine. Temperatures in this application are in excess of 1000 °F—beyond the capabilities of any other seal.

In addition Glenn, under a reimbursable Space Act Agreement, is working with Praxair, a major U.S. producer of industrial gases, to adapt the seal technology for use in the company's proprietary high-temperature industrial gas systems.

Some of the attributes of the seal are as follows: It is a flexible seal that can be used at very high temperatures (2000+ °F) in numerous aerospace and industrial applications; it can bend around sharp radii (about equal to the seal's diameter), conforming to and sealing complex turbine components; and it exhibits low leakage, retains resilience after high-temperature cycling, and can support structural loads. The seal can be braided of emerging ceramic and/or superalloy fibers to meet specific application requirements.

Dr. Steinetz, a Senior Research Engineer at Glenn, is responsible for coordinating NASA's engine seal development projects. He earned his Ph.D. in Mechanical and Aerospace Engineering at Case Western Reserve University, Cleveland, Ohio, in 1991. Currently, Dr. Steinetz leads a research team that includes Michael Adams and Lawrence Kren, who helped perform the laboratory tests qualifying the seal for subsequent engine tests.

Mr. Sirocky was a Senior Project Engineer at Glenn until 1985, when he retired with 30 years of Government service. He was working for Sverdrup Technology, Inc., when the patent for the seal was issued.

Glenn contact: Bruce M. Steinetz, (216) 433–3302

Bibliography

Arnold, S.M.; and Saleeb, A.F.: On the Thermodynamic Framework of Generalized Coupled Thermoelastic-Viscoplastic-Damage Modeling. NASA TM–105349, 1992.

Arnold, S.M.; Saleeb, A.F.; and Castelli, M.G.: Specialized Deformation Tests for the Characterization of a Viscoelastoplastic Model: Application to a Titanium Alloy. NASA TM–106268, 1997.

Arnold, S.M.; Saleeb, A.F.; and Castelli, M.G.: A Fully Associative, Nonisothermal, Nonlinear Kinematic, Unified Viscoplastic Model for Titanium Alloys. NASA TM–106926, 1995.

Arnold, S.M.; Saleeb, A.F.; and Castelli, M.G.: A Fully Associative, Nonlinear Kinematic, Unified Viscoplastic Model for Titanium Based Matrices. NASA TM–106609, 1994.

Arora, G.K.; and Proctor, M.P.: JTAGG II Brush Seal Test Results. AIAA Paper 97–2632, (NASA TM–107448) 1997. (Available online: http://letrs.lerc.nasa.gov/cgi-bin/LeTRS/browse.pl?1997/TM-107448.html).

Brewer, D., et al.: Measurement of Mechanical Damage in SiC/SiC Composites Using Vibration, Acousto-Ultrasonic, and Thermographic NDE. HITEMP Review, NASA CP–10178, Vol. II, paper no. 36, 1995, p. 1.

Castelli, M.G.: A Summary of Damage Mechanisms and Mechanical Property Degradation in Titanium Matrix Composites Subjected to TMF Loadings. Thermal-Mechanical Fatigue of Aircraft Engine Materials, AGARD CP–569, 1996a, pp. 12:1-12.

Castelli, M.G.: Characterization of Damage Progression in SCS–6/Timetal 21S $[0]_4$ Under Thermomechanical Fatigue Loadings. Life Prediction Methodology for Titanium Matrix Composites, ASTM STP–1253, W.S. Johnson, J.M. Larsen, and B.N. Cox, eds., American Society for Testing and Materials, Philadelphia, 1996b, pp. 412–431.

Castelli, M.G.; and Bhanu Sankara Rao, K. Cyclic Deformation of the Superalloy Haynes 188 Under Isothermal and Thermomechanical Loadings, *Superalloys 1996*, The Minerals, Metals & Materials Society, 1996, pp. 375–382.

Darolia, R., et al.: Design Methodology of Intermetallics. IHPTET F33615–94–C2414, R&D Status Report no. 10, 1996.

Dimofte, F.; Wave Journal Bearing With Compressible Lubricant, Part I: The Wave Bearing Concept and a Comparison With a Plain Circular Journal Bearing. STLE Tribology Transactions, vol. 38, no. 1, 1995, pp. 153–160.

Handschuh, R., et al.: Experimental Evaluation of Face Gears for Aerospace Drive System Applications. NASA TM–107227 (ARL–TR–11109), 1997.

Huber, R.D.; and Green, R.E., Jr.: Acousto-Ultrasonic Nondestructive Evaluation of Materials Using Laser Beam Generation and Detection. NASA CR–185282, 1990.

Jadaan, O.M.; Powers, L.M.; and Gyekenyesi, J.P.: Creep Life of Ceramic Components Using a Finite Element Based Integrated Design Program (CARES/*Creep*). ASME Paper 96–GT–369, 1996.

Janosik, L.A.; Duffy, S.F.: A Viscoplastic Constitutive Theory for Monolithic Ceramics—I. ASME J. Eng. Gas Turbines and Power, vol. 120, no. 1, Jan. 1998, pp. 155–161.

Kautz, H.E.: Non-Contact Determination of Antisymmetric Plate Wave Velocity in Ceramic Matrix Composites. NASA TM–107125, 1996.

Krantz, T.L.: A Method to Analyze and Optimize the Load Sharing of Split Path Transmissions NASA TM–107201, 1996. (Available online: http://letrs.lerc.nasa.gov/cgi-bin/LeTRS/browse.pl?1996/TM-107201.html).

Krantz, T.L.; and Delgado, I.R.: Experimental Study of Split-Path Transmission Load Sharing. NASA TM–107202, 1996.

Lee, H.-J.; and Saravanos, D.A.: Active Compensation of Thermally Induced Bending and Twisting in Piezoceramic Composite Plates. AIAA Paper 96–1277–CP, Apr. 18–19, 1996a, pp. 120–130.

Lee, H.-J.; and Saravanos, D.A.: Coupled Layerwise Analysis of Thermopiezoelectric Composite Beams. AIAA J., vol. 34, no. 6, June 1996b, pp. 1231–1237.

Lee, H.-J.; and Saravanos, D.A.: Layerwise Finite Elements for Smart Piezoceramic Composite Plates in Thermal Environments. AIAA Paper 96–1277 (NASA TM–106990), 1996c.

Lei, J.-F., et al.: Comparison Testings Between a High Temperature Extensometer and a Resistance Strain Gage With Multiple Installation Techniques. Experimental Mechanics, vol. 36, no. 4, Dec. 1996, pp. 434–439.

Lewicki, D.G.; and Ballarini, R.: Gear-Crack Propagation Investigation. NASA TM–107147, 1996a.

Lewicki, D.G.; and Ballarini, R.: Effect of Rim Thickness on Gear Crack Propagation Path. NASA TM–107229, 1996b. (Available online: http://letrs.lerc.nasa.gov/cgi-bin/LeTRS/browse.pl?1996/TM-107229.html).

Lin, H.H., et al.: Balancing Dynamic Strength of Spur Gears Operated at Extended Center Distance, NASA TM–107222, 1997. (Available online: http://letrs.lerc.nasa.gov/cgi-bin/LeTRS/browse.pl?1997/TM-107222.html).

Liou, C.-H., et al.: Using Hob Offset to Balance Dynamic Strengths in Spur Gears. NASA TM–106934, 1995.

Lissenden, C.J., et al.: Experimental Determination of Yield and Flow Surfaces under Axial-Torsional Loading. Multiaxial Fatigue and Deformation Testing Techniques, ASTM STP–1280, S. Kalluri and P.J. Bonacuse, eds., 1997, pp. 92–112.

Lissenden, C.J., et al.: Verification of Experimental Techniques for Flow Surface Determination, NASA TM–107053, 1996. (Available online: http://letrs.lerc.nasa.gov/cgi-bin/LeTRS/browse.pl?1996/TM-107053.html).

Nemeth, N.N., et al.: Designing Ceramic Components for Durability. Advanced Ceramic Matrix Composites—Design Approaches, Testing and Life Prediction Methods, E.R. Generazio, ed., Technomic Publishing Co., Lancaster, PA, 1996a, pp. 3–16.

Nemeth, N.N., et al.: Durability Evaluation of Ceramic Components Using CARES/*Life*. J. Eng. Gas Turb. Power (NASA TM–106475), vol. 118, no. 1, 1996b, pp. 150–158.

Periera, J.M.; Kautz, H.E.; and Roth, D.J.: Measurement of Mechanical Damage in Ceramic Matrix Composites Using Vibration and Acousto-Ultrasonic NDE. HITEMP Review. NASA CP–10146, Vol. I, 1994, pp. 23–1 to 23–2. (Permission to cite this material was granted by Carol A. Ginty, December 1997.)

Roth, D.J.: Single Transducer Ultrasonic Imaging Method That Eliminates the Effect of Plate Thickness Variation in the Image. NASA TM–107184, 1996. (Available from NASA Glenn's Subsonic Systems Office.)

Roth, D.J., et al.: Commercial Implementation of NASA-Developed Ultrasonic Imaging Methods via Technology Transfer, Materials Evaluation, vol. 54, no. 11, November 1996a, pp. 1305–1309.

Roth, D.J., et al.: Commerical Implementation of Ultrasonic Velocity Imaging Methods via Cooperative Agreement Between NASA Glenn Research Center and Sonix, Inc. NASA TM–107138, 1996b. (Available online: http://letrs.lerc.nasa.gov/cgi-bin/LeTRS/browse.pl?1996/TM-107138.html).

Salem J.A.; Noebe, R.; and Mandersheid, J.: Reliability Modeling of Brittle Anistropic Materials. Proceedings of the 22nd Annual Conference on Composite Advanced Ceramics Materials and Structures, Jan. 20–24, Cocoa Beach, FL, 1998.

Salem, J.A., et al.: Reliability Analysis of Uniaxially Ground Brittle Materials. J. Eng. Gas Turbines Power (NASA TM–106852), vol. 118, no. 4, 1996, pp. 863–871.

Safaeinili, A.; Lobkis, O.I., and Chimenti, D.E.: Air-Coupled Ultrasonic Characterization of Composite Plates. Materials Eval., Oct. 1995, pp. 1186–1197.

Sokolowski, T.M., et al.: Stress and Reliability Analysis of a Metal-Ceramic Dental Crown. NASA TM–107178, 1996.

Telesman, J.; Ghosn, L.J.; and DeLuca, D.P.: Influence of the Failure Mode on Fatigue Crack Growth Behavior in Single Crystal Superalloys. Hydrogen Effects in Materials, A.W. Thompson and N.R. Moody, eds., The Minerals, Metals & Materials Society, Warrendale, PA, 1996, pp. 943–952.

Verrilli, M.J. and Castelli, M.G., eds.: thermomechanical Fatigue Behavior of Materials: Second Volume, ASTM STP–1263. American Society for Testing and Materials, Philadelphia, 1996.

Ye, L.: On Fatigue Damage Accumulation and Material Degradation in Composite Materials. Comp. Sci. Technol., vol. 36, no. 4, 1989, pp. 339–350.

Zakrajsek, J.J.; and Lewicki, D.G.: Detecting Gear Tooth Fatigue Cracks in Advance of Complete Fracture. NASA TM–107145, 1996. (Available online: http://letrs.lerc.nasa.gov/cgi-bin/LeTRS/browse.pl?1996/TM-107145.html).

REPORT DOCUMENTATION PAGE

Form Approved
OMB No. 0704-0188

Public reporting burden for this collection of information is estimated to average 1 hour per response, including the time for reviewing instructions, searching existing data sources, gathering and maintaining the data needed, and completing and reviewing the collection of information. Send comments regarding this burden estimate or any other aspect of this collection of information, including suggestions for reducing this burden, to Washington Headquarters Services, Directorate for Information Operations and Reports, 1215 Jefferson Davis Highway, Suite 1204, Arlington, VA 22202-4302, and to the Office of Management and Budget, Paperwork Reduction Project (0704-0188), Washington, DC 20503.

1. AGENCY USE ONLY (*Leave blank*)

2. REPORT DATE
November 1999

3. REPORT TYPE AND DATES COVERED
Technical Memorandum

4. TITLE AND SUBTITLE
Structures and Acoustics Division 1996 Annual Report

5. FUNDING NUMBERS
WU–910–31–11–00

6. AUTHOR(S)
Cynthia S. Acquaviva

7. PERFORMING ORGANIZATION NAME(S) AND ADDRESS(ES)
National Aeronautics and Space Administration
John H. Glenn Research Center at Lewis Field
Cleveland, Ohio 44135–3191

8. PERFORMING ORGANIZATION REPORT NUMBER
E–11118

9. SPONSORING/MONITORING AGENCY NAME(S) AND ADDRESS(ES)
National Aeronautics and Space Administration
Washington, DC 20546–0001

10. SPONSORING/MONITORING AGENCY REPORT NUMBER
NASA TM—1999-206966

11. SUPPLEMENTARY NOTES
Responsible person, Cynthia Acquaviva, organization code 5900, (216) 433–3306.

12a. DISTRIBUTION/AVAILABILITY STATEMENT
Unclassified - Unlimited
Subject Category: 39 Distribution: Nonstandard

This publication is available from the NASA Center for AeroSpace Information, (301) 621–0390.

12b. DISTRIBUTION CODE

13. ABSTRACT ***(Maximum 200 words)***

The Structures and Acoustics Division of NASA Glenn Research Center is an international leader in rotating structures, mechanical components, fatigue and fracture, and structural aeroacoustics. Included are disciplines related to life prediction and reliability, nondestructive evaluation, and mechanical drive systems. Reported are a synopsis of the work and accomplishments reported by the Division during the 1996 calendar year. A bibliography containing 42 citations is provided.

14. SUBJECT TERMS
Structural mechanics; Structural fatigue; Structural dynamics; Structural integrity; Mechanical components; Acoustics

15. NUMBER OF PAGES
65

16. PRICE CODE
A04

17. SECURITY CLASSIFICATION OF REPORT	18. SECURITY CLASSIFICATION OF THIS PAGE	19. SECURITY CLASSIFICATION OF ABSTRACT	20. LIMITATION OF ABSTRACT
Unclassified	Unclassified	Unclassified	